

Radio Emissions from Laser Induced Breakdown of Materials

A thesis submitted

to

University of Hyderabad

for the award of

Doctor of Philosophy in Physics



by

Vinoth Kumar L (10ACPP07)

Advanced Centre of Research in High Energy Materials (ACRHEM)

School of Physics, University of Hyderabad

Hyderabad 500046

Telangana, India.

August 2016

DECLARATION



I, **Vinoth Kumar L**, hereby declare that this thesis entitled “**Radio Emissions from Laser Induced Breakdown of Materials**” submitted by me under the guidance of **Dr. P. Prem Kiran**, Assistant Professor, ACRHEM, School of Physics, University of Hyderabad, is a bonafide research work which is also plagiarism free. I also declare that it has not been submitted previously in part or in full to this University or any other University or Institution for the award of any degree or diploma. I hereby agree that my thesis can be deposited in Shodhganga/INFLIBNET.

A report on plagiarism statistics from the University Librarian is enclosed.

Date:

Vinoth Kumar L
(10ACPP07)



**University of Hyderabad, Central University (P.O.),
Gachibowli, Hyderabad-500 046, India**

CERTIFICATE

This is to certify that the thesis entitled '**Radio Emissions from Laser Induced Breakdown of Materials**' being submitted to the University of Hyderabad by **Vinoth Kumar L** (Reg. No: 10ACPP07), for the award of **Doctor of Philosophy in Physics**, is a bonafide work carried out by him under my supervision and guidance which is a plagiarism-free thesis.

The thesis has not been submitted previously in part or in full to this or any other University or Institution for the award of any degree or diploma.

Dr. P. Prem Kiran
Thesis Supervisor
(ACRHEM)

Head of the Department/ Center

(ACRHEM)

Dean

(School of Physics)

To

My Parents

Smt. Bharathi and Shri. Lakshmi Narayanan

ACKNOWLEDGEMENTS

There are many people who inspired, influenced, supported and helped me to come to a stage where I am in today. I take it as an opportunity to express my love and gratitude towards all of them. I may not be able to spell all the names here. However those missing here are equally important.

*I had an average schooling. When I scored less in my plus two exams, it was my mother **Smt. Bharathi** who was backing me with all her love and support. After she left her physical body, I was blessed with the admission into B.Sc Physics on her birthday. Three years later, on her birthday again, I was blessed with the alumni scholarship, which helped me to apply for M.Sc admissions in many of the prestigious institutions. There by, I always feel her love and support inspite of her physical absence. My father **Mr. Lakshmi Narayanan**, inspite of not having a rich formal education, always gave his best to educate me. My elder brother **Venkatesh**, inspite of having a very tough childhood days, made sure that I am safe and secured. He gave me all the freedom to do whatever I wanted to, by taking all the family responsibilities on his shoulders, besides supporting my education. My sister-in-law **Smt. Manasa**, filled all the voids and energized us with all her love, affection and support. She deserves a lot of credit for the success of our family. My younger brother **Vijay**, who is always a source of joy and inspiration to me, never failed to keep my spirits up. I am all in tears, whenever I think of the hardships my family people went through to protect me and make me feel comfortable. I am short of words to express my gratitude. I bow down and say "I love you all".*

*Without a guru, life is incomplete. I am fortunate to have been blessed with a wonderful guru in the form of **Dr. P. Prem Kiran**. It was the freedom he always offered, to express myself and explore whatever I want to, helped me think out of the box and learn a lot. Thanks a ton for being you Sir. I would like to express my gratitude to my teachers **Smt. Godavari, Smt. Amudhavalli, Mr. Ezhil Palaniswamy, Mr. Kalaimani, Mr. Balasubramanian, Smt. Alamelu, Mr. Saravana Kumar, Dr. V. Parthiban, Prof. S. P. Tewari, Dr. Soma Venugopal Rao, Prof. James Raju and Dr. Manoj Kumar** not only for educating me, but*

also for shaping me to be a socially responsible man with character and values. I would also thank my music teachers **Dr. Balasubramaniam, Smt. Anuradha, Mr. Madhu, Smt. Krithi and Smt. Janaki** for providing me the required fuel for my research activities.

A friend in need is a friend in deed. I am really showered with loads of blessings in the form of lovely friends like **Hemanth, Vinay, Krishna, Sai Pramod, Sukanya, Jeganathan, Nagarathanam, Venkatesh, Shamanth, Yeshwanth, and Aravind**. Thank you all for accepting me and spending a lot of time with me. All your love, affection and time are greatly appreciated. My special thanks to **Dr. Aruna**, who has always been showering loads and loads of unconditional love on me.

I am extremely thankful to University of Hyderabad and ACRHEM for giving me the opportunity to pursue my PhD here. I thank to all the directors (past and present) and faculty members of ACRHEM. My special thanks and regards to my doctoral committee members for their technical support and discussions. I express my heartfelt gratitude to my senior **Dr. Leela**, who set the tone for our entire research group. I also thank **Manikanta** for helping in carrying out the experiments and other colleagues of the group for their support. I want to thank all my HCU friends, notably **Paul Praveen, Vinoth, Dr. V. Praveen, Dr. Sai Kiran, Ashwin, Anil, Sachin, Nageswara Rao, Anusha, Ganesh, K. Srinivasa Rao, Narasimha, Abdul Kalam** etc. I also thank all the staff members of ACRHEM office for all their help and assistance. I also acknowledge the financial assistance from DRDO to complete my thesis successfully.

.....Vinoth Kumar L.

Contents

1. Chapter I: Introduction	1
1.1.Pulsed laser-matter interactions	2
1.2.RF emissions from natural astronomical sources	4
1.3.Literature survey on low frequency emissions from LIB	5
1.4.Objectives of the thesis	6
1.5.Brief organization of the thesis	7
2. Chapter II: Experimental details	9
2.1.Details of the experimental diagnostics	10
2.1.1. Laser sources.....	10
2.1.2. Details of the spectrum analyzer.....	10
2.1.3. Details of the detecting antennas	12
2.2.Experimental setup.....	14
2.3.Optimization of the experimental set up and conditions	15
2.3.1. Calibration of the spectrum analyzer with known RF sources	15
2.3.2. Experiments with the diamond RH-799 whip antenna.....	16
2.3.3. Whip vs Lindgren antenna	17
2.3.4. Detection of higher frequencies	19
2.3.5. Dependence of antenna polarization.....	20
2.4.Experiments to extract data with minimum error	21
2.4.1. Signal to noise ratio	21
2.4.2. Estimation of error in the measurements	22
2.4.3. Finalized experimental setup and data analysis procedure	26
2.5.Positioning of the detector	27
2.5.1. Angular and radial distribution of the emissions	27
2.5.2. Angular distribution of emissions with circularly polarized pulses.....	31
2.5.3. Positioning of the detector in case of solid targets	32
3. Chapter III: Radio emissions from laser induced breakdown of atmospheric air	35

3.1.Results	36
3.1.1. Effect of antenna polarization.....	36
3.1.2. RF spectra from ns and ps LIB of atmospheric air	39
3.2.Emission Mechanism	42
3.3.Discussion	44
3.3.1. Effect of pulse duration.....	44
3.3.2. Dependence of RF emissions on focusing conditions	46
4. Chapter IV: Radio emissions from laser induced breakdown of solid targets	59
4.1.Effect of antenna polarization	61
4.2.Data analysis	61
4.2.1. RF emissions from LIB of conductors.....	61
4.2.2. RF emissions from LIB of insulators.....	64
4.2.3. RF emissions from LIB of dielectrics.....	66
4.3.Discussion	69
5. Chapter V: Radio emissions from laser induced breakdown of copper powder compacts.....	77
5.1.Introduction	78
5.2.Sample preparation	80
5.3.Results and discussions.....	82
6. Chapter VI: Radio emissions from laser induced breakdown of high energy materials	99
6.1.Introduction	100
6.2.Results and discussions.....	103
7. Chapter VII: Summary and future scope.....	113
7.1.Summary	114
7.1.1. Optimization of conditions for maximum RF reception from LIB.....	114
7.1.2. Material specific RF emissions from LIB.....	116
7.1.3. Separation of material classes from the strength of RF emissions	118
7.1.4. Dependence of input laser energy on RF emissions from LIB	120

7.1.5. Dependence of target surface on RF emissions from LIB	120
7.2.Future scope	121
8. References	123
9. List of publications.....	135
10. List of awards	136

Chapter I

Introduction

This chapter describes the objectives of the thesis with the basic introduction on the emissions from pulsed laser-matter interactions, RF emissions from astronomical sources and their relevance in the possibility of utilizing them for standoff identification of materials.

Pulsed laser-matter interactions lead to plasma formation and associated emission of radiation. The emissions in radio frequency (RF) and microwave region of the electromagnetic spectrum are relatively unexplored. The signature emissions, reported from the astronomical sources, travelling towards the detector over the distance of several light years encourage the development of a remote sensing tool using radio waves. Laser induced breakdown (LIB) of materials were reported to be a sophisticated way to generate RF radiation which are proposed to be utilized for laser ground penetrating radar (LGPR) application. The aim of this thesis is to systematically study the RF emissions from the LIB of various materials by tuning the laser and target parameters. The understanding of the emission mechanism and the optimization of favourable conditions to generate and detect RF emissions may lead to the possibility of developing a potential sensing technique using RF radiation from LIB.

1.1 Pulsed laser-matter interactions

Pulsed laser-matter interaction [1-3] is a widely investigated topic due to its diverse applications [4]. When a laser pulse of sufficient intensity is focused on a target material (solid, liquid, gas), the medium gets converted into plasma state [4, 5]. This is known as laser induced breakdown (LIB) of materials. Plasma formation by optical breakdown is a result of an avalanche process of electron multiplication. It begins with a few seed electrons which may initially be present in the material or may be generated due to the laser induced ionization. These seed electrons, gaining energy from the laser electric field, can develop electron avalanche ionization by repeated collisions with the neutral atoms and molecules in the medium. Following the energy and momentum conservation, the laser energy can be absorbed by the electrons only when they collide with a atom or ion. Therefore, the process becomes effective only in dense media where the probabilities of electron-atom and electron-ion collisions are higher. Once there is appreciable ionization in the medium, intense heating and the hydrodynamic expansion of the plasma takes place. The result is the appearance of a spark in case of gas media and the associated visible damage in case of condensed media. Hence, as a consequence of the laser-matter interaction, the target material will attain the plasma state with a temperature range of 3000-10000 K.

Depending on the plasma temperature and conditions, the plasma created during LIB tends to attain equilibrium with mechanical (acoustic [7-9] and shock waves [10,11]) emissions, which are due to the pressure drive from the plasma core to the surroundings and the electromagnetic emissions across the entire electromagnetic spectrum [12-32], which are due to the spectroscopic transitions. The energy release, in different forms, from the plasma due to LIB of materials is shown in fig 1.1. Most of the electromagnetic emissions from LIB were extensively studied to be applied in various fields. For example, the THz, visible and x-ray emissions from LIB are successfully utilized in THz remote sensing [33], LIB spectroscopy (LIBS) [34, 35], and x-ray astronomical simulation respectively [36]. However, the emission of very low frequency radiation, radio frequency (RF) and microwaves, from LIB remains relatively less explored.

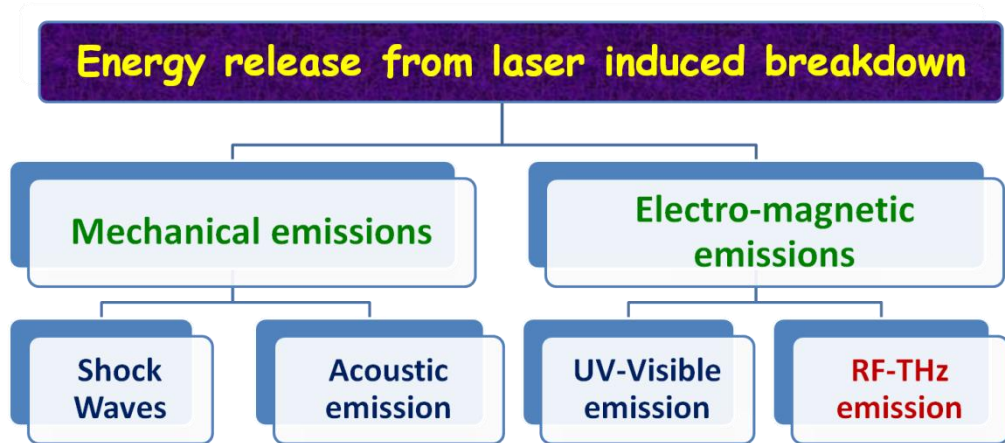


Fig 1.1: Emissions from laser induced breakdown of materials

The RF band starts from a few Hz to thousands of GHz. The details are given in table 1.1. The receiving antenna is tuned with an LC circuit with specific resonant frequency, amplifying the signals within the band of interest while reducing other frequencies outside the band [37]. Different regions of the radio spectrum are allocated for different radio technologies and applications where some parts are licensed to be operated for specific purposes.

Table 1.1: Radio frequency bands

Frequency	Wavelength	Designation	Abbreviation
3-30 Hz	10^5 - 10^4 km	Extremely low frequency	ELF
30-300 Hz	10^4 - 10^3 km	Super low frequency	SLF
300-3000 Hz	10^3 - 10^2 km	Ultra low frequency	ULF
3-30 kHz	10^2 -10 km	Very low frequency	VLF
30-300 kHz	10-1 km	Low frequency	LF
0.3-300 MHz	1km-100 m	Medium frequency	MF
3-30 MHz	100-10 m	High frequency	HF
30-300 MHz	10-1 m	Very High frequency	VHF
0.3-3 GHz	1 m-1 cm	Ultra High frequency	UHF
3-30 GHz	10-1 cm	Super High frequency	SHF
30-300 GHz	1 cm-1 mm	Extremely High frequency	EHF
0.3-3 THz	1-0.1 mm	Tremendously High frequency	THF

1.2 RF emissions from natural astronomical sources

The RF emissions from many astronomical sources have been studied for many decades. The reports on the emissions from sun, planets, flare stars, outer heliosphere, alpha orionis and other astronomical sources [38-48] explain that most of these emissions are due to the acceleration of charged particles in the hot, ionized interstellar gases. Synchrotron emission, one of the non thermal radiation processes, was also reported to be a dominant process in the astronomical emissions. The synchrotron emissions are due to the electrons spiraling in magnetic fields at speeds comparable to that of light. The emissions [49-56] from solar flares, cosmic ray showers and natural aurora are reported to be due to the propagation of charged particles through the dust particles. Besides these free-free emissions, which are due to the energetic free electrons, emissions due to bound-free (during recombination) and bound-bound (due to electron motion between the bound states) transitions [57] were also reported to be the origin of radiation from astronomical sources. Table 1.2 summarizes the emissions reported from some of the astronomical objects.

Table 1.2: Natural astronomical RF sources

Astronomical body	Frequency range
Earth	30-800 KHz
Jupiter	20 KHz- 40 MHz
Saturn	20-1200 KHz
Uranus	20-1200 KHz
Neptune	20-1300 KHz
Sun	30 KHz-30 GHz

The RF frequencies from these astronomical sources have been identified to be element specific. Several studies were reported on these element specific frequencies [58-62]. All the reported frequencies have been reviewed by the international astronomical union (IAU). Some of the reported astronomical RF signatures from different molecules reviewed by IAU are given in table 1.3.

Table 1.3: RF signatures from astronomical sources

Compound	Observed frequencies (GHz)
Carbon monoxide (CO)	115.271, 230.538, 461.041, 691.473, 806.652
Carbon monosulphide (CS)	48.991, 97.981, 244.953, 342.883
Formaldehyde (H ₂ CO)	4.83, 14.488, 137.45, 140.840
Hydrogen isocyanide (HNC)	88.632, 265.886, 271.981, 354.484, 797.433
Water vapour (H ₂ O)	22.235, 183.310, 380.197, 547.676

The element specific RF emissions that are detected from a distance of several light years indicate the properties of these radiations in propagating over larger distances with minimum attenuation. The element specificity and the long range propagation of RF emissions, from the natural astronomical sources, are encouraging features favouring them to be considered for remote sensing of materials. The impact of space debris on satellites and space stations may result in severe damage. These hypervelocity impacts, which are associated with plasma formation, are monitored by the RF and microwave emissions associated with it [63-67]. The reproducibility in the results, due to the complications in controlling the velocity of the projectile, is one of the setbacks to develop this technique into a tool for remote sensing. LIB of materials is one of the efficient ways to replicate the conditions that are analogous to those which result in RF emissions from astronomical sources. While stand-off sample identification from the conventional LIBS technique is carried out at the distances of a range of few meters, their shortcomings in remote and wireless detection of hazardous environment can be addressed by utilizing the low frequency radiation from LIB, which are least attenuated during propagation [68].

1.3 Literature survey on low frequency emissions from LIB

Pearlman and Dahlbacka were one of the first to observe RF emissions (1-330 MHz region) from dense laser plasmas where the emission mechanism was explained on the basis of oscillations, which were well below the characteristic

Chapter 1: Introduction

plasma frequency, suggesting the existence of macroscopic charge fluctuations in the plasma expansion [69]. Also, Gerdin *et al.* have reported that instabilities such as ion-acoustic in LIB lead to RF and microwave emissions whose frequencies are several orders less than that of the plasma frequency [70]. In an experiment using high energy nanosecond (ns) pulses from CO₂ laser, production and propagation of supra-thermal electrons in the LIB was predicted to induce instabilities and subsequent microwave emission [71]. The recent advancements in the ultrafast optics and lasers have given rise to the high power laser systems that are utilized for the production of supra thermal electrons [72-85] and filamentation that lead to low frequency electromagnetic emissions [86-98].

On the application front, the microwave radiation emitted from the LIB has been proposed to be utilized for the laser-driven ground penetrating radar (LGPR) to overcome the shortcomings of the conventional GPR which require large span antennas or long span measurements to survey a remote location precisely [99]. Some preliminary experiments to measure the characteristics of the microwave emitted and to check the feasibility of this application were also carried out using the sub picosecond (ps) laser pulse induced plasma [100]. In order to utilize the radiation emitted from LIB of materials, it is important to tune the input laser parameters required for the emission of radiation in the desired frequency range. Hence, it is crucial to understand the plasma dynamics in the low frequency emissions from LIB. Thus systematic studies on thorough understanding of the mechanism of low frequency emissions from LIB and their characteristics by tuning the experimental parameters (laser pulse duration, laser energy, properties of the target material etc.) are required.

1.4 Objectives of the thesis

The focus of this thesis is to study the RF emissions from the LIB of different materials by tuning the input laser parameters and the properties of the target material. The aim is to understand the radiation emission mechanism and the optimization of the conditions that favour the generation and detection of RF emissions from LIB. The studies on the variation in the RF emission with respect to target material, under similar experimental conditions, which can pave way for the development of an RF based sensor is the primary objective of this thesis.

Chapter 1: Introduction

1.5 Brief organization of the thesis

Based on the objectives, the thesis has been organized into various chapters which bring up various aspects of the RF emissions from LIB.

Chapter 2 describes the experimental details and the basic characteristics of these emissions that help in arriving at the optimization of the conditions and the precautions to be taken during the measurements. Besides, the experiments to bring down the ambient noise, the studies on radial and angular distribution of RF emissions from LIB, to position the detector, are presented.

Chapter 3 contains the results of the studies carried out on the observation and characteristics of RF emissions from ns and ps LIB of atmospheric air. From the mechanism of RF emissions from LIB, the origin of the RF emissions from LIB is presented. Further the effect of input laser intensity, by varying the focusing conditions, is presented to emphasize the importance of generation of seed electrons and the subsequent RF emissions. The scaling of RF emissions, with $I\lambda^2$, with the optimal intensity conditions to generate RF emissions of appreciable strength is also presented.

Chapter 4 contains the results of the studies carried out on the observation and characteristics of RF emissions from ns and ps LIB of solid targets. The significance of the properties of the target material in the plasma formation and the associated RF emissions from LIB are highlighted by studying the emissions from the LIB of three different classes of target materials; conductors, insulators and dielectrics. The origin of emissions based on the number density (n_e , n_i) of the plasma due to the laser-matter interaction of different materials, the separation of the material classes by the RF amplitude, at low input laser energies and the decay of RF emissions due to plasma recombination, at higher input laser energies, are emphasized.

Chapter 5 contains the results of the investigation of RF emissions from the ns and ps LIB of compacted copper micro powders. The studies on the effect of surface modification on the laser-matter interaction and the associated RF emissions are presented based on the experimental observations of RF emissions from the LIB of targets made up of particles of different particle sizes with

Chapter 1: Introduction

different packing densities. The comparison of the emissions from LIB of the powder compacts with those from the bulk sintered copper target is presented to show the role of reflectance that controls the efficiency of energy transfer between the laser and the target.

Chapter 6 contains the results on the RF emissions from ns and ps LIB of high energy materials (HEMs). The promise in these studies, due to the presence of specific RF bands that are observed in the LIB of organic compounds that contain nitrogen, is highlighted.

Chapter 7 summarizes and concludes the work presented, followed by the future scope of the thesis. The need for further studies to translate the material specific RF emissions from LIB, and the features of appreciable RF generation and their propagation at lower input laser energies, into the development of a wireless laser and RF based sensor is discussed.

Chapter II

Experimental details

This chapter describes the experimental diagnostics and the set up used to study the RF emissions from ns and ps LIB. The optimization of the conditions and the precautions to be taken care to ensure measurements with minimum error are presented in detail.

The calibration of the diagnostics with known RF sources was carried out before proceeding with the experiments. Based on the results of RF detection from LIB of atmospheric air, the emissions from LIB of all the target materials (presented in the subsequent chapters) were detected with the mini biconical antenna (Lindgren 3182, 30-1000 MHz). Besides the estimation of experimental errors, the experiments to improve the signal to noise ratio were carried out. In order to minimize these errors, besides triggering the spectrum analyzer with the incident laser pulses, the average of these 100 spectra was taken into consideration. Moreover, the analyses were carried out by deducting the ambient atmospheric noises. The studies on radial and angular distribution of RF emissions from LIB of atmospheric air and copper target indicate $\sin^2\theta/r^2$ dependence of electric dipolar radiation. It was observed that the signal reception was better when the laser and the antenna polarization match.

2.1 Details of the experimental diagnostics**2.1.1 Laser sources**

In order to optically breakdown a medium, it is necessary to achieve the condition of input intensity of the laser pulses being greater than the breakdown threshold of the medium [5, 6]. In our experiments, second harmonic of Nd:YAG lasers of two different pulse durations: 7 ns (from INNOLAS Spitlight-1200) and 30 ps (from EKSPLA PL2250) were chosen to create optical breakdown. The important laser parameters of these lasers are given in table 2.1. The other details of the lasers can be referred in the respective user manuals [101, 102].

Table 2.1: Few important laser parameters

Parameters	Source 1 (INNOLAS Spitlight-1200)	Source 2 (EKSPLA PL2250)
Laser pulse duration	7 ns	30 ps
Wavelength of operation	532 nm	532 nm
Laser polarization at 532 nm	Linear (vertical)	Linear (horizontal)
Laser beam diameter	8 mm	12 mm
Range of energy used	5 – 100 mJ	1.5 – 38 mJ
Typical theoretical intensities utilized	$\sim 10^{11}$ W/cm ²	$\sim 10^{13}$ W/cm ²

2.1.2 Details of the spectrum analyzer

The detections of low frequency emissions from LIB by various research groups, mentioned in the previous chapter [69-100], were carried out by antennas whose signal receptions were monitored by an oscilloscope. The obtained time domain information of the emitted radiation was converted into the corresponding frequency domain by the fast Fourier transforms (FFT) of the data. Thus, in all those laser based RF and microwave measurements, the diagnostics were designed over a specific narrow band of frequencies limiting the information that can be derived out from the plasmas. In our case, a high resolution spectrum analyzer from Agilent (model: E4448A) which can measure and monitor complex RF, microwave, and millimeter-wave signals from 3 Hz to 50 GHz was used (Fig 2.1). Thus, the frequency evolution over the entire band of the detecting antenna can be obtained at a single shot. Moreover, since the frequency domain information is directly obtained from the spectrum analyzer, the dominant frequency, power,

Chapter 2: Experimental details

distortion, harmonics, bandwidth and the other important spectral components of the signals can be directly observed which are not easily detected in the time domain measurements.

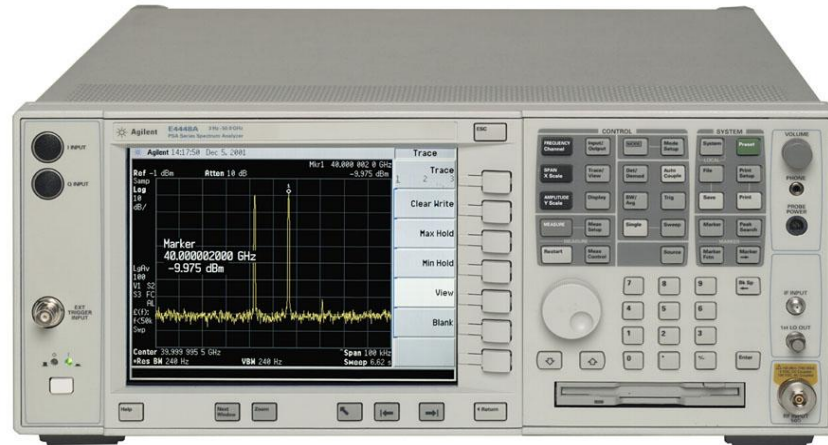


Fig 2.1: Agilent PSA E4448A spectrum analyzer

This high-performance spectrum analyzer is a super heterodyne receiver [103] where the desired frequency is beaten up with that from the local oscillator by the mixer to produce the side-band frequencies along with the intermediate frequency. The lower sideband which is the difference between the input and local oscillator frequencies is of interest in the super heterodyne receiver. The conversion of the received frequency into a fixed intermediate frequency (IF), makes the signal processing relatively simpler. The frequency coverage of the PSA E4448A spectrum analyzer can be expanded up to 325 GHz with optional external harmonic mixers. The important features of this spectrum analyzer are given in table 2.2. The other details can be seen in the user manual [104].

Table 2.2: Few important features of Agilent PSA E4448A spectrum analyzer

Few important parameters	Values
Frequency range	3 Hz – 50 GHz
Dynamic range	+30 dBm to -155 dBm
Input impedance	50 Ohm
Resolution bandwidth (RBW)	1 Hz – 3 MHz
Video bandwidth (VBW)	1 Hz – 3 MHz

Chapter 2: Experimental details

2.1.3 Details of the detecting antennas

The low frequency radiation detectors are antennas of different shapes, frequency ranges and gains. The initial experiments were carried out with diamond RH-799 wide band whip antenna whose frequency range is 70-100 MHz (Fig 2.2). This antenna has an isotropic radiation pattern. The resonant frequency of this antenna can be altered by varying the length of the antenna as shown in Fig 2.2. The details of the variation of resonant frequency with antenna length are given in the table 2.3.



Fig 2.2: Diamond RH-799 whip antenna (70-1000 MHz)

Table 2.3: Antenna lengths and their corresponding resonant frequencies of diamond RH-799 whip antenna

Antenna length (cm)	Resonant frequency (MHz)
23.5	905
23.73	300
24	800
47	430
50	144
61	120
113	70

The other antennas used in the studies, procured from ETS Lindgren, are given in table 2.4. These were antennas with directional gains whose sensitivity is very high compared to that with the isotropic Diamond RH-799 whip antenna.

Chapter 2: Experimental details

Table 2.4: Set of antennas used in the studies

Model	Antenna type	Frequency Range
Diamond RH-799	Telescopic whip	70-1000 MHz
3182	Broadband mini-bicon	30-1000 MHz
3117	Double ridged guide horn	1-18 GHz
3116C-PA	Double ridged guide horn	18-40 GHz

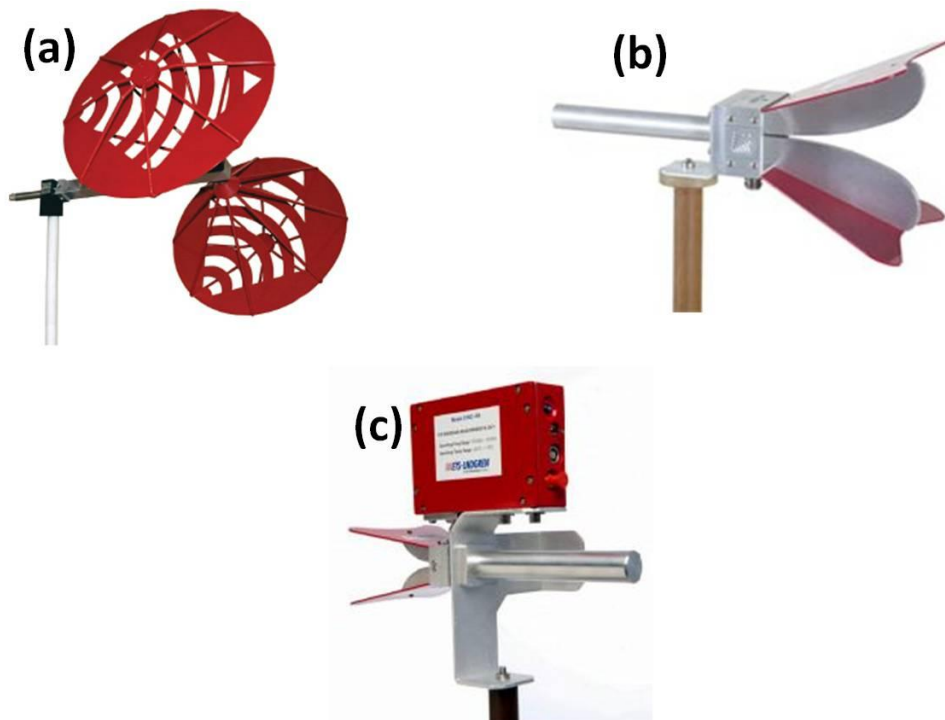


Fig 2.3: (a) 3182 broadband mini-bicon antenna (30-1000 MHz) (b) 3117 double-ridged guide antenna (1-18 GHz) and (c) 3116C-PA Double-Ridged Waveguide Horn antenna (18-40 GHz)

The total range of frequency covered in our experiments was 30 MHz to 40 GHz with the antennas that are shown in Fig 2.3. The Lindgren 3182 broadband mini-bicon antenna is capable of detecting radiation in the frequency range 30- 1000 MHz. The 3117 double-ridged guide antenna and the 3116C-PA double-ridged waveguide horn antenna cover 1-18 GHz and 18-40 GHz respectively. The physical dimensions of the antennas were directly proportional to the wavelength that has to be detected. The length, width and height of the 3182 mini-bicon antenna, which is the largest of the antennas used, was 53.34 cm, 41.30 cm and 62.70 cm respectively. This antenna covers (30-1000 MHz) all of the VHF and

Chapter 2: Experimental details

part of the UHF bands. Hence, this is one of the extensively used antennas for spectrum monitoring of FM, TV and some cellular phones. The detailed specifications of these antennas can be referred from the antenna user manual [105].

2.2 Experimental setup

The experimental setup is shown in Fig 2.4.

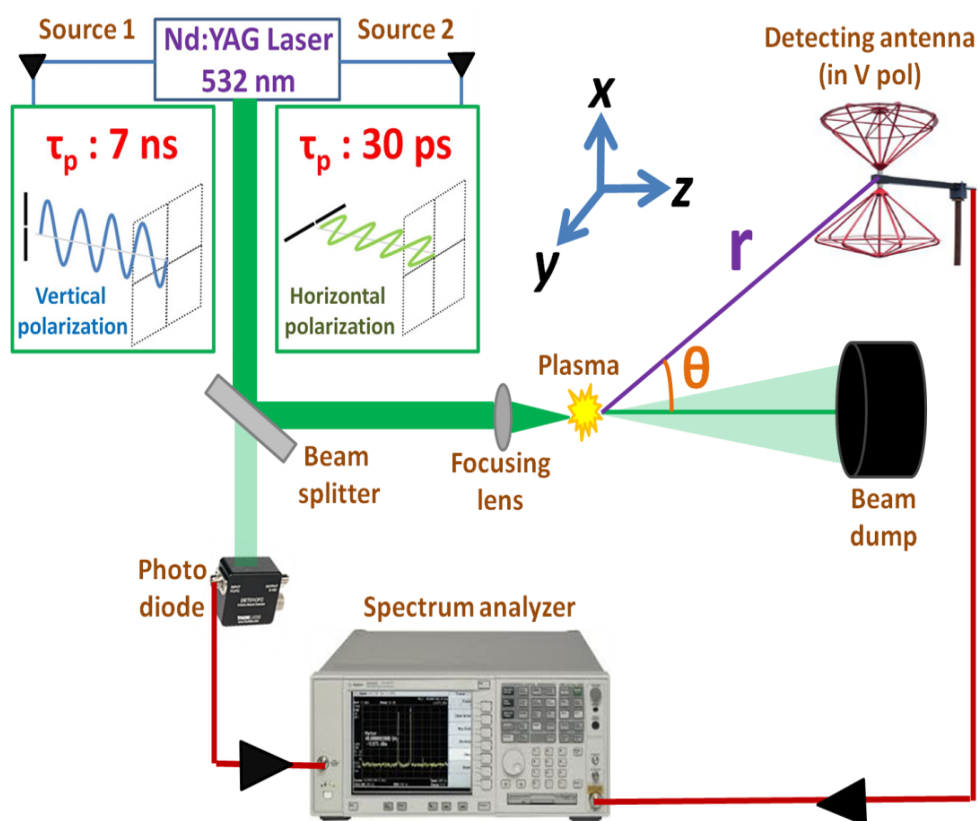


Fig 2.4: Experimental setup. The laser propagation is along z direction in both ns and ps LIB

Second harmonic (532 nm) of Nd:YAG lasers of two different pulse durations: 7 ns (INNOLAS spitlight-1200) and 30 ps (EKSPLA PL2250) were focused on different target materials to generate LIB. The RF emissions from the plasma are detected by the antenna (Lindgren 3182 broadband mini-bicon) that is coupled to the spectrum analyzer (Agilent model: E4448A) where the signals are monitored and recorded. The beam dump blocks the defocused laser beam after focal plane during LIB of atmospheric air. The setting up of the diagnostics, optimization of the experimental conditions and the positioning of the detector are as follows.

2.3 Optimization of the experimental set up and conditions

Before performing the actual measurements, it is very important to set the diagnostics to ensure reliability of the measurements. The works carried out in setting up the diagnostics are presented in this section.

2.3.1 Calibration of the spectrum analyzer with known RF sources

The first and most important step is to ensure that the spectrum analyzer is in proper working condition. In order to do that, RF signals from standard sources are to be chosen. Also, RF signal detection and analysis has the problem of interference of the signal to be detected with waves from the electronic devices (due to the inbuilt oscillator circuits) and the waves utilized for communication purposes. These contribute to the noise which, as a consequence, suppresses the signals of interest. RF emissions from the mobile phones is one of the most important and predominant sources of noise. Hence, an experiment with mobiles of different service providers was performed to find the corresponding uplink and down link frequencies (Fig 2.5). The lindgren 3182 (30-1000 MHz) and 3117 (1-18 GHz) antennas were used for this experiment. These results are tabulated in table 2.5.

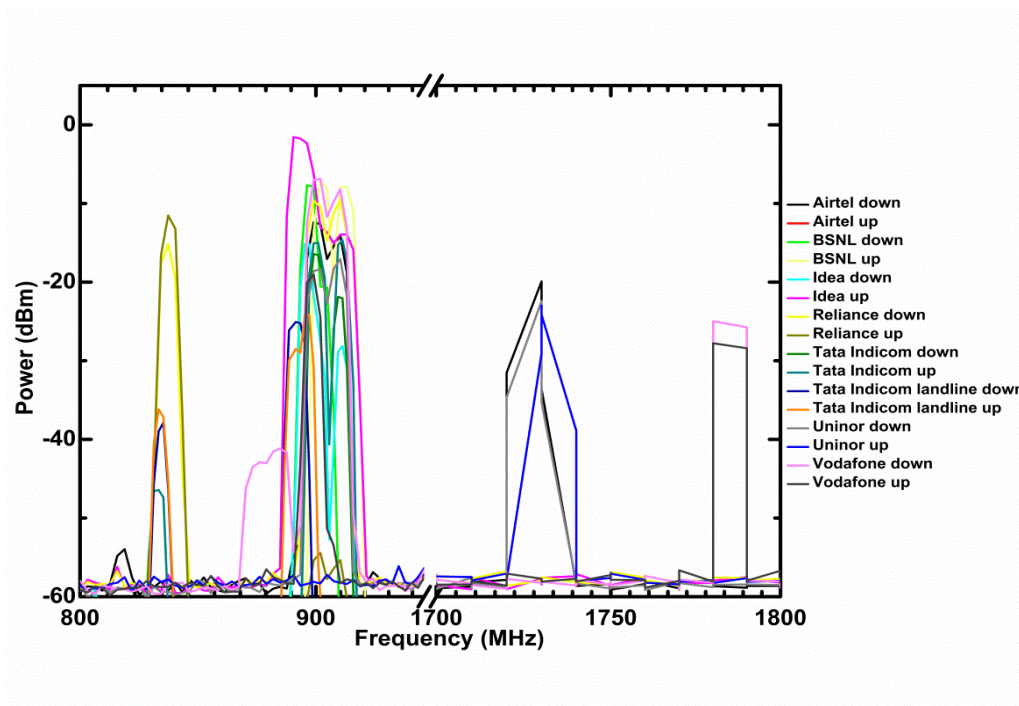


Fig 2.5: Uplink and downlink frequencies of different mobile services detected using lindgren 3182 (30-1000 MHz) and 3117 (1-18 GHz) antennas

Table 2.5: Uplink and downlink frequencies of different mobile phone services

Mobile service	Uplink frequency (MHz)	Downlink frequency (MHz)
Airtel	891 – 913	896 – 914
BSNL	890 – 915	890 – 914
Idea	890 – 913	891 – 896
Reliance	836 – 836	835 – 836
Tata Indicom	832 – 834	899 – 911
Tata Indicom (landline)	829 – 838	836
Uninor	1720 – 1740	1728
Vodafone	1782	899 – 917

These bands were confirmed from the telecom spectrum allocation charts [106]. Hence, the above experiment shows the good working condition of the spectrum analyzer besides helping in identifying the major interfering signals.

2.3.2 Experiments with the diamond RH-799 whip antenna

After the experiments to ensure the proper working of the spectrum analyzer with different mobile service providers, the experiments to arrive at the detector to be used for the measurements were carried out. The initial experiments were performed with the diamond RH-799 whip antenna to check for the resonant frequencies at different antenna lengths. The measurements of RF emissions were performed with 7 ns laser source with atmospheric air as target material. The RF spectra from 7 ns LIB of air at 35 mJ input laser energy at different antenna lengths is shown in Fig 2.6.

For each antenna length, the corresponding resonant frequency was observed in the spectrum. Besides the resonant frequency some additional frequency lines were also observed. For example, when the antenna length was 50 cm, which was set to resonate at 144 MHz, prominent peaks were observed at around 140 MHz to

Chapter 2: Experimental details

160MHz. In addition to that, some more peaks at 290 MHz, 328 MHz, 446 MHz, 520 MHz etc., were also observed. Hence, it is confirmed that the same plasma source tends to give many spectral lines.

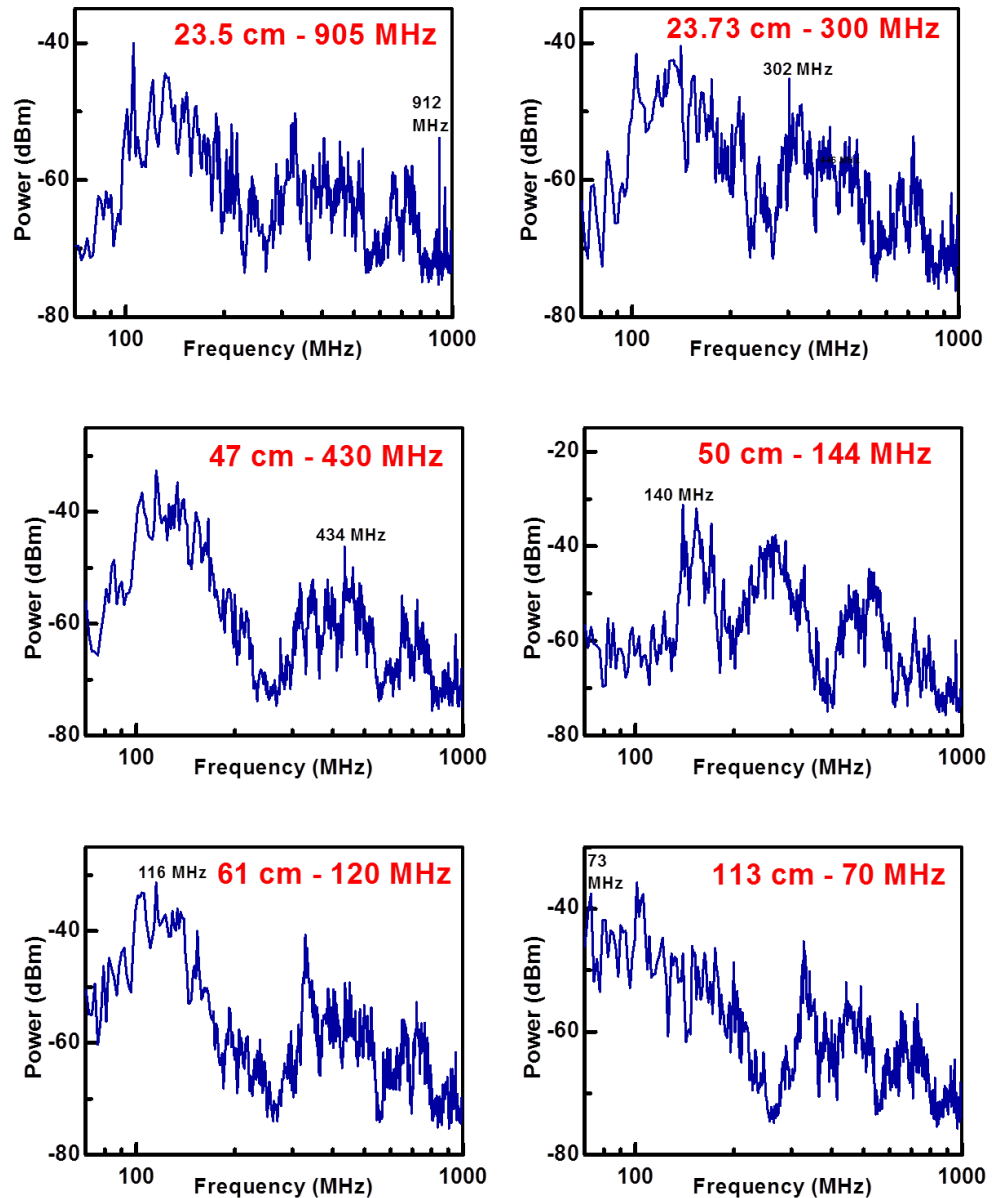


Fig 2.6: RF emissions from 7 ns LIB of air at 35 mJ with diamond RH-799 antenna at different lengths. Antenna length and the corresponding resonant frequency are labeled in each spectrum

2.3.3 Whip vs Lindgren antenna

Even though the spectra with diamond whip antenna has many lines including those of resonant frequencies at different lengths, the spectral lines were poorly resolved. Moreover, the signal to noise ratio was very low. This is due to the lower gain of the antenna due to isotropic reception. Hence the experiments were

Chapter 2: Experimental details

repeated, under similar conditions, with the Lindgren antenna which has directional gain. The spectra are shown in Fig 2.7.

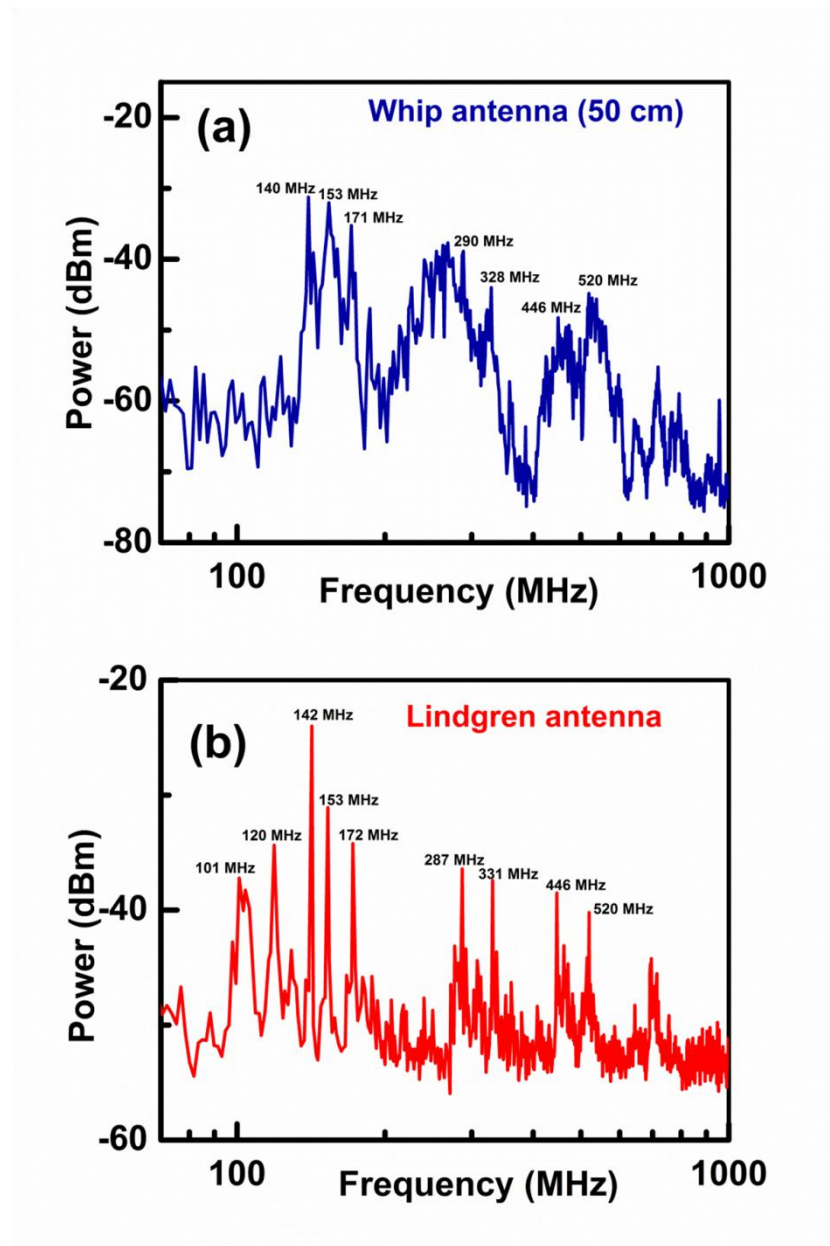


Fig 2.7: Comparison of RF emissions from 7 ns LIB of air at 35 mJ with (a) Diamond RH-799 antenna at 50 cm (144 MHz) and (b) Lindgren 3182 antenna under similar experimental conditions

In the above spectra, most of the frequencies (153 MHz, 446 MHz, 520 MHz) are common with both the antennas where as the other frequencies are also almost common with a very small difference of ± 3 MHz. Even though the spectra look alike, the spectral lines with the Lindgren biconical antenna were clear, distinct and well resolved with better signal to noise ratio. This is because of the

Chapter 2: Experimental details

directionality in the gain of the antenna. A similar trend of well resolved lines was observed with mini-bicon antenna for ps LIB. Hence, further experiments in 30 - 1000 MHz range of frequencies were carried out with the Lindgren biconical antenna.

2.3.4 Detection of higher frequencies

The experiments on RF emissions from ns and ps LIB of air were also carried out with antennas of higher frequencies (1 – 40 GHz). The spectra are given in Fig 2.8.

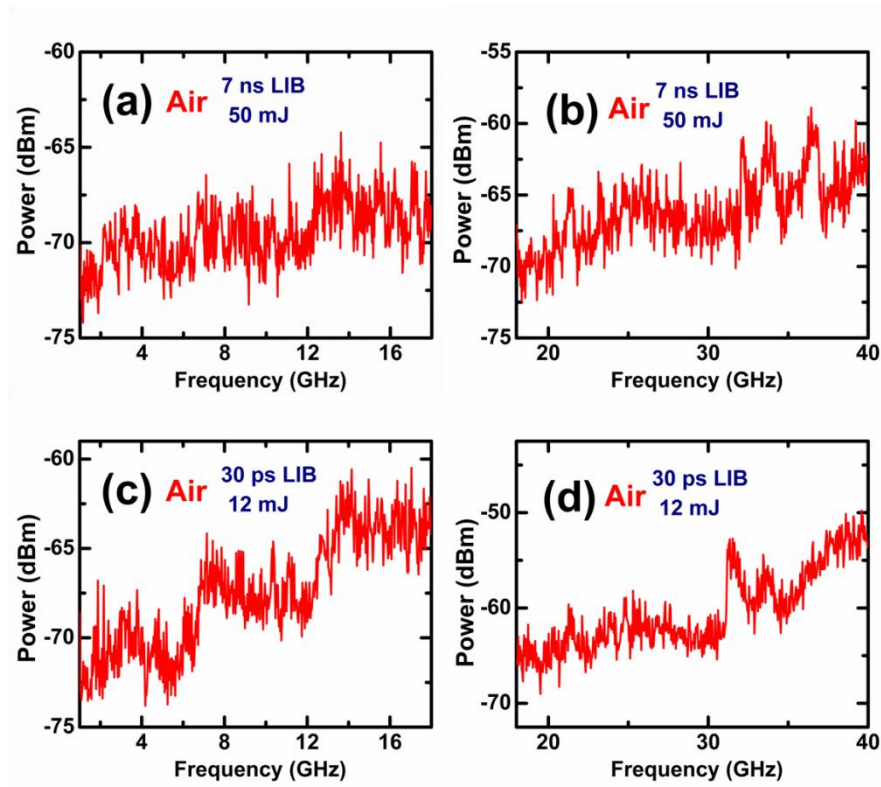


Fig 2.8: Spectra from (a) ns and (c) ps LIB of air over 1-18 GHz with lindgren 3117 antenna and spectra from (b) ns and (d) ps LIB of air over 18-40 GHz with lindgren 3116B antenna

The lines in high frequency range were observed to be poorly resolved. As a result, the noise floor and the signals could not be clearly distinguished. Moreover, the strength of RF emissions in 1-40 GHz range was observed to be relatively lesser than that in 30-1000 MHz range. Hence, the measurements and analysis of the emissions from LIB of all the target materials were planned to be carried out with Lindgren biconical antenna, over 30-1000 MHz, before proceeding with the detection of higher frequencies.

2.3.5 Dependence of antenna polarization

Electromagnetic waves, being transverse in nature, have a specific polarization [106]. RF receivers are designed in such a way that they are compatible to receive signals when they are oriented in a particular direction. In short, for a particular antenna polarization, the signal reception becomes better [107]. Hence it is important to understand the polarization concept. Consider an electromagnetic wave travelling along z direction as shown in Fig 2.9. The electric field and magnetic field are oscillating along x and y directions respectively. Whenever the antenna is oriented parallel to the electric field of the electromagnetic radiation, the signal reception is better than that with the antenna oriented perpendicular to the electric field of the propagating radiation. In the figure, assuming the laser polarization as vertical, the parallel antenna condition is termed as vertical polarization and the cross polarization condition is termed as horizontal antenna polarization. These conditions are valid for the Lindgren 3182 antenna.

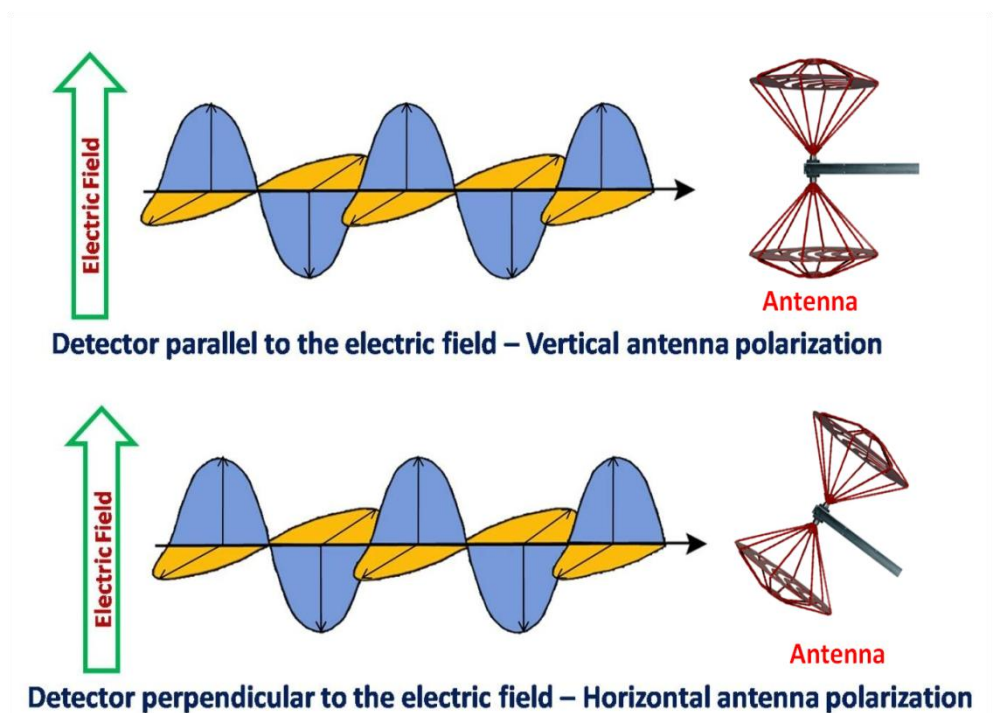


Fig 2.9: Antenna polarization (considering vertical laser polarization)

2.4 Experiments to extract data with minimum error

Any measurement is prone to have errors. There are many contributors to these errors. The instrumental errors (least count and resolution) [109] and error in observation (parallax) [110] are some of the important contributors of experimental errors. It is important to identify the sources of the errors and the ways in which these errors can be brought down during the measurements.

2.4.1 Signal to noise ratio

One of the challenges in instrumentation is to identify the signals of interest and to eliminate noises. Hence, it is crucial to enhance the signal to noise ratio [111] in any of the measurements. In our case, the external noises are to be eliminated by allowing the detector to collect the signals only from LIB. For this, the spectrum analyzer was externally triggered. The triggering was done with respect to the pockel cell of the laser and then with respect to the photo detector. The spectra without plasma formation, under different conditions (no triggering (free run), pockel cell triggering and photo detector triggering) with 7 ns laser pulses at 40 mJ energy, were recorded to check the inherent noise levels (Fig 2.10).

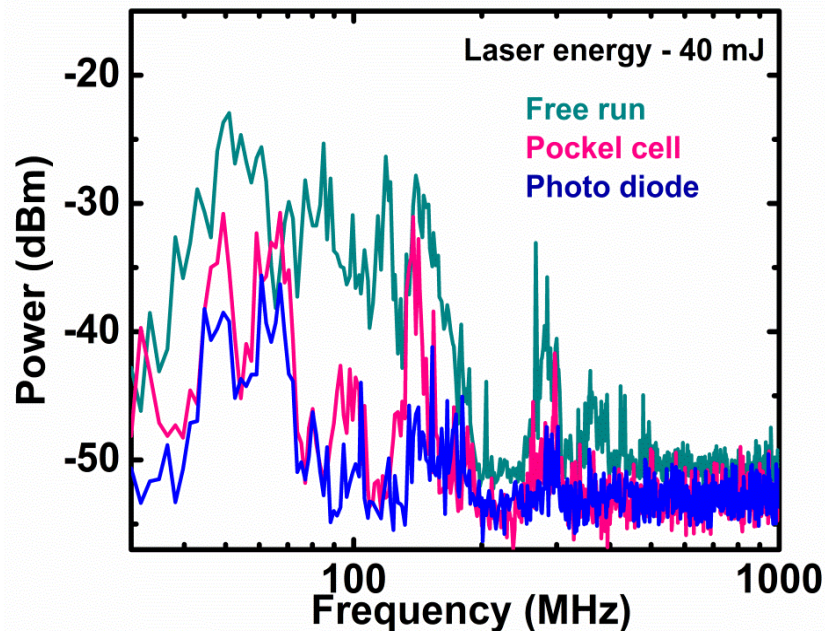


Fig 2.10: Noise without plasma formation at 40 mJ laser energy detected with lindgren 3182 antenna (30-1000 MHz)

Chapter 2: Experimental details

From the spectra (Fig 2.10), the amplitude of the noise signals were observed to be higher when the measurements were carried out with the spectrum analyzer in the free run (no trigger) mode. For example, at ~ 50 MHz, the ambient noise level was observed to be around -25 dBm with the spectrum analyzer in the free run mode. The noise was measured to be around -30 dBm, when the spectrum analyzer was triggered with respect to the pockel cell of the laser. This was observed to come down further (-40 dBm), when the spectrum analyzer was triggered with respect to the photo detector. From these, it is evident that there is a considerable improvement in the signal to noise ratio when the spectrum analyzer is externally triggered. Again, triggering with respect to the photo detector proved to be better than that with the pockel cell. This is because the pockel cell, being a source of RF waves, contributes additional signals to the spectrum which in turn descends the signal to noise ratio [112]. Based on these studies, all the subsequent experiments were performed by triggering the spectrum analyzer with respect to the laser pulse using a photo detector.

2.4.2 Estimation of error in the measurements

Knowing the contribution from each factor of error is important to understand the measurements better. In our experiments, the contribution of errors due to laser fluctuations and the limitations in the instruments (antennas and spectrum analyzer) are to be found out. Hence, the detection of RF emissions from ns and ps laser induced breakdown (LIB) of air was performed under different conditions (at different energies, with and without antenna etc.). The 3182 broadband biconical antenna (30-1000 MHz) was used to detect RF emissions. Under each condition, 50 measurements were carried out. The ns and ps laser pulses were focused with 80 mm convex lens. The corresponding focal spot diameters ($2\omega_0$) of the ns and ps pulses focused in air were estimated to be $\sim 140 \pm 10 \mu\text{m}$ and $\sim 160 \pm 10 \mu\text{m}$. Fig 2.11 shows the pulse to pulse fluctuations in the RF emissions from ns and ps LIB of atmospheric air at 10 mJ and 4 mJ input laser energies respectively.

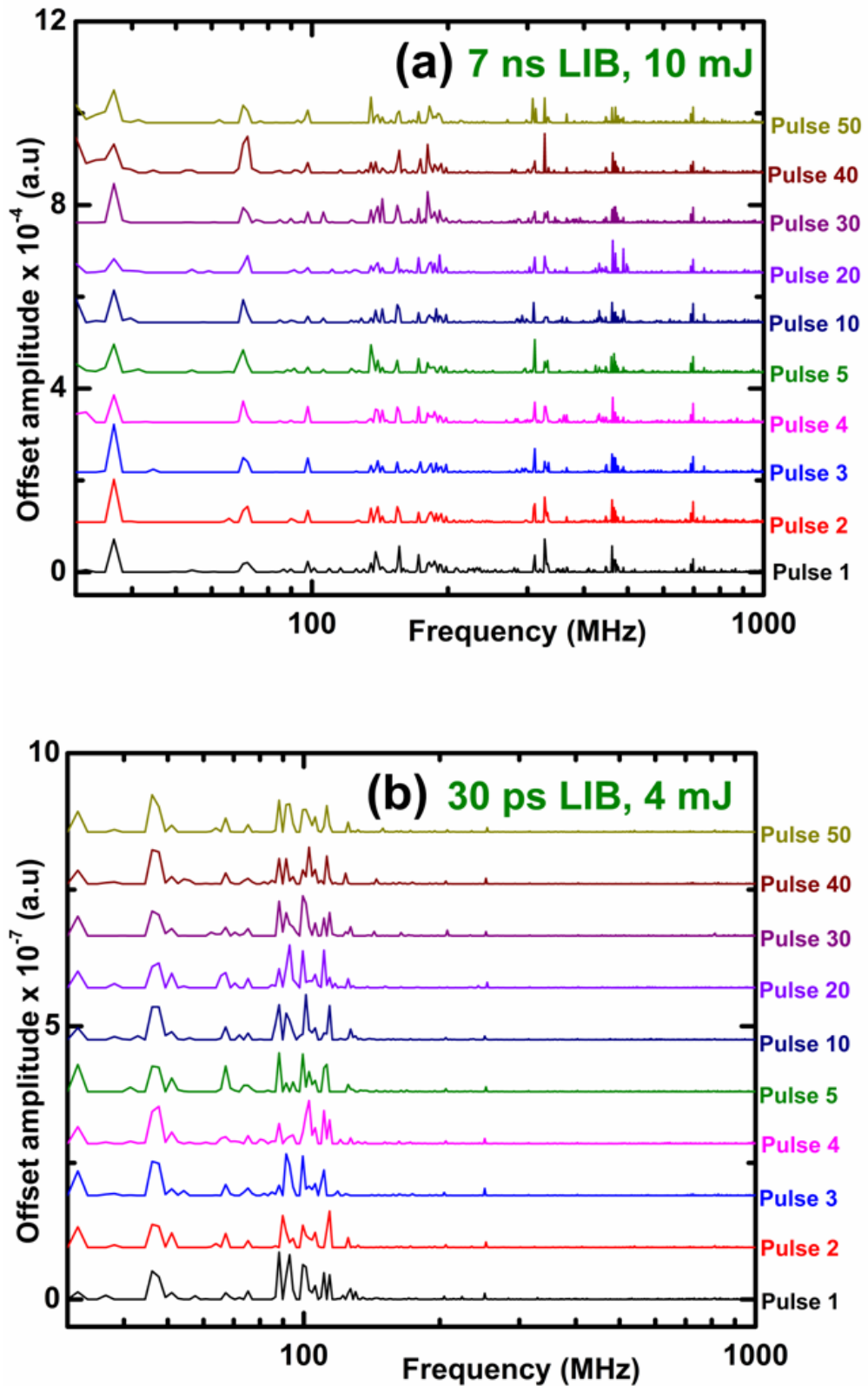


Fig. 2.11. Fluctuations in the RF emissions from (a) ns and (b) ps LIB of air with respect to input laser pulses

Chapter 2: Experimental details

The frequency spectrum from the breakdown of every laser shot was observed to be similar, barring few alterations in the amplitude. Analyzing the frequencies, no harmonics were observed in the emitted spectra. This shows that the frequency lines represent the RF emissions from the LIB of the target medium. If 'd' is the dimension of the radiation source, 'r' is the distance between the source and the detector and λ is the wavelength to be detected, the near field radiation condition [37] is satisfied if $d \ll r \ll \lambda$. Generally the RF signals, due to near field loading, will have poor resolution. This is evident from the broadened peaks in the lower frequency region (30-100 MHz). However, the high frequency (>100 MHz) signals have better resolution. To overcome the loss of signals due to near field loading effects, it is important to minimize the obstruction loss by removing obstacles from the line of sight of the plasma source. Therefore, it was ensured that the radiation from plasma reaches the detector without any obstruction. Besides, the focusing of laser pulses was carried out well away from the laser system and the beam steering optics. The standard deviation and the corresponding errors were estimated. The results are tabulated in 2.6 and 2.7.

Table 2.6: Error in RF emissions from 7 ns LIB of air

Experimental condition	Error (%)
Only with spectrum analyzer	1.2
Spectrum analyzer with 3182 broadband antenna (30 – 1000 MHz) without laser	2.3
With laser (at 10 mJ energy) without plasma formation	8.8
Laser (at 10 mJ energy) breakdown of air	10.6
Laser fluctuations (at 10 mJ energy)	7.3
With laser (at 100 mJ energy) without plasma formation	3.9
Laser (at 100 mJ energy) breakdown of air	4.4
Laser fluctuations (at 100 mJ energy)	3.2

Chapter 2: Experimental details

Table 2.7: Error in RF emissions from 30 ps LIB of air

Experimental condition	Error (%)
Only with spectrum analyzer	1.2
Spectrum analyzer with 3182 broadband antenna (30 – 1000 MHz) without laser	2.3
With laser (at 4 mJ energy) without plasma formation	3.8
Laser (at 4 mJ energy) breakdown of air	4.5
Laser fluctuations (at 4 mJ energy)	3.5
With laser (at 38 mJ energy) without plasma formation	1.3
Laser (at 38 mJ energy) breakdown of air	1.8
Laser fluctuations (at 38 mJ energy)	1.0

From the above tables, it was observed that the error is negligible when RF emissions are recorded only with spectrum analyzer without the antenna in connection. The increase in error in the RF measurements was observed when the antenna was connected to the spectrum analyzer. It is seen that the contribution of error, in the measurement of RF emissions, keeps increasing when new parameters are included in the experiments. The laser fluctuations were observed to be one of the major factors of error in the measurements. The fluctuations in the laser energies at low input laser energies were observed to be high. This is reflected in the measurements (Table 2.6). The maximum possible errors in case of ns LIB and ps LIB were estimated to be 10.6% and 4.5% respectively. In order to minimize the error in measurements, the experiments were planned to be performed at least with 100 laser shots with one RF spectrum per shot. The average of these 100 RF spectra was taken into consideration for further analysis.

From the above discussions, it was concluded that the Lindgren biconical antenna (30 – 1000 MHz), which has a directional gain, will be the predominant detector in the experiments. In order to get the data that is free from noises, it was also concluded to trigger the spectrum analyzer with respect to the laser pulse with the

Chapter 2: Experimental details

aid of the photo diode. Further, the experiments were planned to be performed for atleast 100 laser shots where the average of the spectra obtained from these 100 laser shots will minimize the experimental errors. But still, there is high contribution of noise due to the electronic equipments in the lab. These equipments contain many RC circuits which is a very good source of RF radiation [108]. In order to eliminate the contribution of these noise components, the following procedure was followed in carrying out the experiments. Before recording the RF spectrum from the LIB of the target, the ambient noise (without plasma formation) was recorded. This noise data was then subtracted from the ns and ps LIB data that contains noise as well as the signals of interest. This was done assuming that the ambient noise is constant when the data was recorded with and without laser induced breakdown. However, to overcome errors in the inconsistencies in the noise, the experiments were checked for the repeatability of data by performing multiple times (besides, considering the average spectrum of 100 laser shots). The analyses carried out in all the chapters were following this procedure.

2.4.3 Finalized experimental setup and data analysis procedure

After a complete set of studies on the details of the experimental diagnostics, minimization of experimental errors and the precautions to be taken care during the experiment and data analysis, the finalized experimental set up was arrived (Fig 2.4). Second harmonic (532 nm) of Nd:YAG lasers of two different pulse durations: 7 ns (INNOLAS spotlight-1200) and 30 ps (EKSPLA PL2250) were focused on different target materials to generate LIB. The broadband mini biconical antenna (Lindgren 3182) of frequency range 30-1000 MHz was used as the radiation detector. To ensure better signal to noise ratio, the spectrum analyzer was externally triggered by the laser pulse through the photo detector signal. The polarization state of ns and ps laser pulses was vertical and horizontal, respectively. The laser energy was in the range of 5–200 mJ with ns and 1.5–38 mJ ps pulses, leading to intensities of the order of 10^{11}W/cm^2 and 10^{13}W/cm^2 , respectively. The antenna polarization is termed as vertical (V-pol), whenever it is oriented parallel to the x axis. When it is rotated parallel to the y axis, it is termed as horizontal antenna polarization (H-pol). To study the polarization effects, the antenna was rotated to measure the H-pol and V-pol components of emissions.

Chapter 2: Experimental details

In order to eliminate the contribution of the ambient noise signals in the RF spectra, before measuring the signals of interest, the measurement of the ambient noise (at different input laser energies) was carried out by recording the spectrum without plasma formation. As mentioned in 2.4.2, this noise data was subtracted from the LIB data that contains noise as well as signals of interest. In order to avoid complexity and make this subtraction straight forward, the powers in dBm units were converted into corresponding powers in microwatt (μW) units thereby getting rid of the negative and logarithmic components of the dBm units. In all the subsequent analysis, the amplitude of the RF signals was specified in the microwatt (μW) units. Besides, the average RF spectrum from those from the LIB of atleast 100 laser shots was considered for data analysis.

In order to arrive at the integrated power of RF emissions from LIB of the targets, the frequency domain RF spectra were converted into the corresponding time domain spectra by inverse fast Fourier transformation (IFFT). The area under the curve of the time domain spectrum gives the total energy output of the emitted RF radiation.

$$\text{Area under the curve} = \int_{t_1}^{t_2} f(t)dt = \text{Total output energy}$$

The emission of radiation varies under different focusing conditions, which alters the focal volume. Therefore, the total output energy is normalized with respect to focal volume and the solid angle subtended by the detector. This is termed as the normalized RF output. This normalized RF output was considered in all the subsequent analyses that involve the integrated RF emissions from LIB.

2.5 Positioning of the detector

Besides studying the experimental conditions to extract error free data on the RF emissions from LIB, it is very important to position the detector for maximum signal reception. Hence the studies on angular and radial dependence of RF emissions from LIB become crucial.

2.5.1 Angular and radial distribution of the emissions

The angular measurements, from the LIB of atmospheric air, were carried out at different angles between the source and the detector, by keeping the distance

Chapter 2: Experimental details

fixed. The laser pulses were focused at a focusing geometry (f/D) ~ 10 . The emissions from ns LIB at an input laser energy of 40 mJ is shown in Fig 2.12 (a). The amplitude of 120-140 MHz band was observed to be increasing with the angle between the source and the detector with the maximum when the source and the detector are perpendicular to each other (90° and 270°). Similar results were observed in case of emissions from ps LIB (Fig 2.12 (c)). The normalized RF output was plotted as a function of angle of detection. These results are depicted in polar plots (with measurements from maximum possible points) with different antenna polarizations (Fig 2.12b and 2.12d). The emissions with same laser and antenna polarization were observed to be stronger than those with cross polarization.

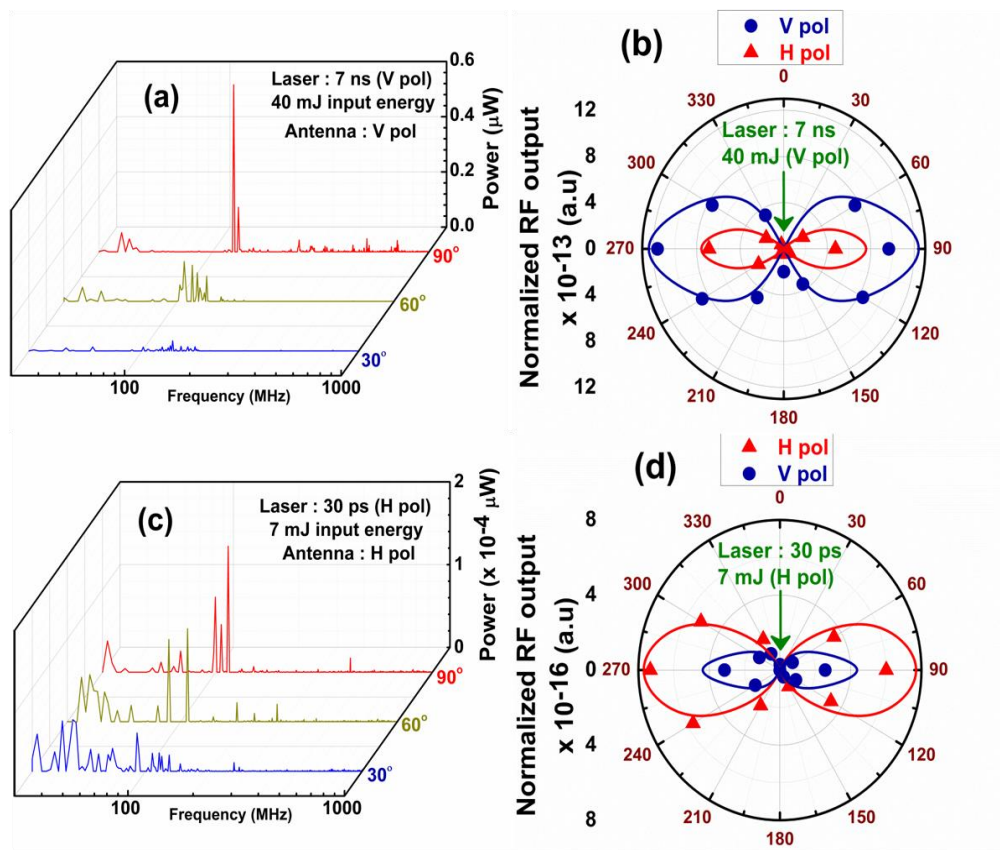


Fig 2.12. Angular distribution fits of RF emissions from (a) 7 ns LIB at 40 mJ laser energy (c) 30 ps LIB at 7 mJ laser energy and the corresponding polar plots from (b) 7 ns LIB and (d) 30 ps LIB with different antenna polarizations. (Arrows depict the laser direction)

The near field and far field conditions for an antenna play a crucial role in signal reception [37]. The critical distance R is given by $R = 2d^2/\lambda$, where, λ is the wavelength and d is the largest dimension of the antenna. The far-field condition

Chapter 2: Experimental details

is satisfied, if the antenna distance from the source is greater than R . In our experiments, the LIB is not a monochromatic source since a band of frequencies is observed to be emitted from it. Hence the near field and far field conditions will vary with every individual emitted frequency. The radial dependence of emissions, with the detector perpendicular to the source, at different input laser energies from ns and ps LIB was carried out. The spectra from ns LIB at 25 mJ input laser energy and ps LIB at 12 mJ input laser energy are shown in Fig 2.13a and 2.13b respectively. The amplitude of lines was observed to be decreasing with the distance between the source and the detector. Similar results were observed in case of emissions from ns LIB. The integrated emitted power, plotted as a function of distance between the source and the detector (Fig 2.13c and 2.13d) indicates the radial dependence of the emissions from ns and ps LIB at various input laser energies.

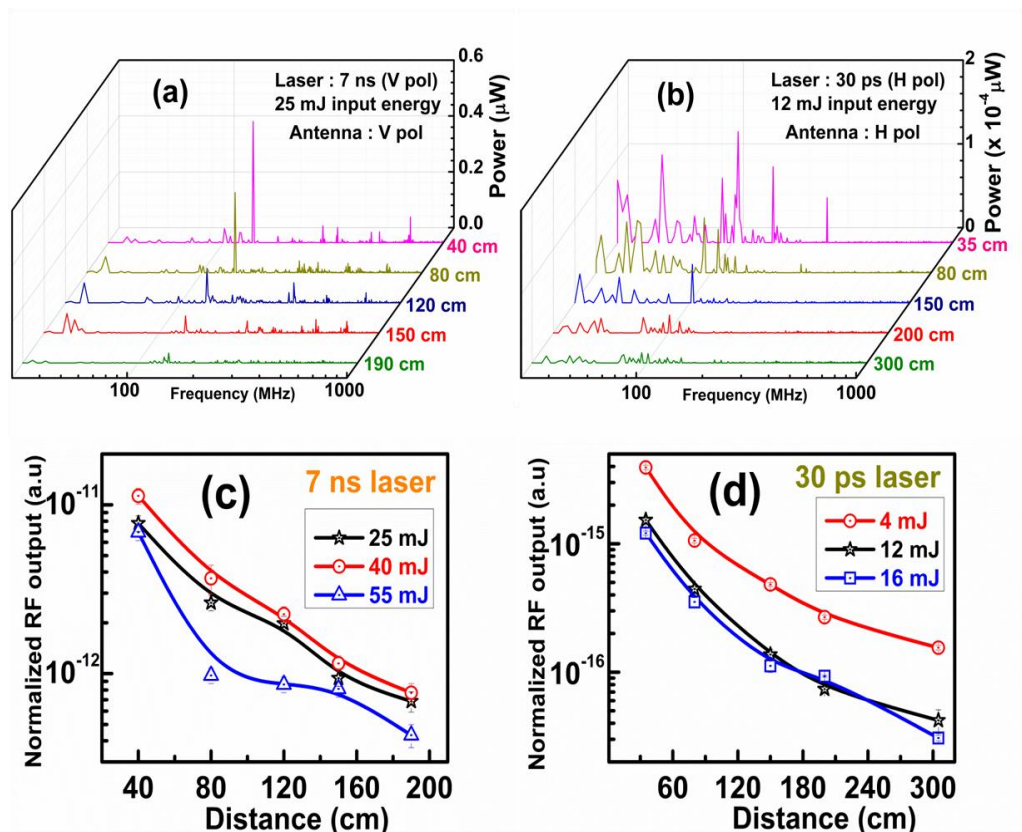


Fig 2.13: Spatial distribution fits of RF emissions with detector 90° with respect to the source from (a) 7 ns LIB at 25 mJ laser energy (b) 30 ps LIB at 12 mJ LIB and the corresponding radial RF output at different laser energies from (c) 7 ns LIB and (d) 30 ps LIB

Chapter 2: Experimental details

During the expansion of plasma due to LIB of air, under the influence of the electromagnetic field of a laser pulse, electric dipole moments (p) are induced [99]. These oscillating electric dipoles radiate em waves in the RF and microwave range of frequencies. The generation of such an intrinsic dipole structure aligned with the beam axis directed opposite to the wave propagation vector was experimentally confirmed [113]. The intensity (I) of the dipolar radiation, which is the average of the Poynting vector (S), is given by [114]

$$I(r, \theta) = \left(\frac{\mu_0 p^2 \omega_p^4}{32 c \pi^2} \right) \frac{\sin^2 \theta}{r^2} \hat{r} \quad (2.1)$$

where, ‘the symbols ‘ θ ’ and ‘ r ’ represent the angle and the distance between the source and the detector, respectively as shown in Fig 2.4. Here, ω_p is the plasma frequency and ‘ p ’ is the induced dipole moment whose variation with input laser intensity is explained in detail in section 3.3.2.

The angular distribution of normalized RF emissions, with linear input laser pulses, were turned out to vary as $\sin^{1.5}\theta$ and $\sin^{1.6}\theta$ in case of ns and ps LIB, respectively, for the laser and antenna polarizations used in the present study. Similarly, for the spatial emissions, the best possible fits were obtained for $r^{-1.8\pm 0.1}$ and $r^{-1.75\pm 0.05}$ in case of ns LIB and ps LIB respectively. The slight deviation from $\sin^2 \theta / r^2$ can be accounted to the have quadrupole and multipole contributions of emissions which depend on the n_e value. The details of the mechanisms involved in the RF emissions are given in section 3.2. The asymmetry in the polar plots can be accounted for the fluctuations in the plasma evolution. When the pulse duration of the laser pulse is very long (longer than ns), the optical discharge propagates mainly within the laser beam (the region in which energy is supplied). Thus, charge separation occurs primarily at the leading and trailing fronts which correspond to the general quadrupole charge configuration in a laser spark. For nanosecond and picosecond pulses of relatively high intensities ($\sim 10^{11} - 10^{12}$ W/cm²), the transition from the optical detonation regime to the breakdown wave regime could reduce the effective electron concentration and temperature gradients in the region of the leading front of the laser pulse. Therefore, the dipole due to the trailing front of the laser pulse is predominant and this forms a plasma spark with quasi-dipole distribution of the electric field [115]. Therefore,

Chapter 2: Experimental details

the amplitude of RF emissions from ns and ps LIB is approximated to inverse square variation.

The magnitude of electric potential is higher due to the plasma formed by the breakdown of a medium with laser pulses of relatively longer pulse duration. This is attributed to the change in plasma dimensions, since the reduction in the transverse size of the dipoles lowered the electric fields in their vicinity in case of breakdown with lasers of shorter pulse durations. Hence, the amplitude of electric field with ns LIB should be higher than that with ps LIB. Thus, considerable difference is observed in the RF emissions from ns and ps LIB. Also, at higher input laser energies, the higher electric fields generated lead to the higher values of electron density (n_e), which contributes to the plasma frequency (ω_p). Under these conditions, the emission of radiation comes down as the recombination of the plasma constituents dominates [116]. Thus, under specific focusing conditions, the RF emissions of greater amplitude are generated at lower input laser energies. Besides, the strength of the signals achieved at lower energies was observed to be higher even at distances away from the plasma source. At a distance 190 cm away from the plasma, the amplitude of RF emissions from ns LIB at 40 mJ is observed to be ~ 1.8 times greater than that at 55 mJ input laser energy (Fig 2.13c). Similarly, in case of ps LIB, at 300 cm away from the source, the amplitude of emissions at 4 mJ is observed to be ~ 5 times higher than that at 16 mJ laser energy (Fig 2.13d) [117]. This is one of the attractive features that support RF emissions from LIB to be utilized for remote sensing.

2.5.2 Angular distribution of emissions with circularly polarized pulses

The angular dependence of RF emissions was also studied with the circularly polarized input laser source. For this, the linearly polarized laser beam was converted into circularly polarized beam by introducing a quarter wave plate in the path of the laser beam. The spectra from ns LIB and ps LIB of air and their corresponding polar plots are given in Fig 2.14.

The variation of amplitude of emissions with angle of detection with the circularly polarized input laser radiation is very similar to that with linearly polarized input radiation. The maximum amplitude of emissions is detected when the antenna is placed perpendicular (at 90° or 270°) to the plasma source. When the theoretical

Chapter 2: Experimental details

fit was made, the contribution of antenna polarization was quantified equally because of the equal distribution of electric field in the horizontal and vertical directions of the circularly polarized laser source [118]. The experimental data was fit to equation 2.1. Unlike the antenna polarization dependence with linear laser source, the amplitude of RF emissions at different antenna polarization with circularly polarized laser source was observed to have same magnitude. Hence, with circularly polarized pulses, the specific dependence of antenna polarization is lost.

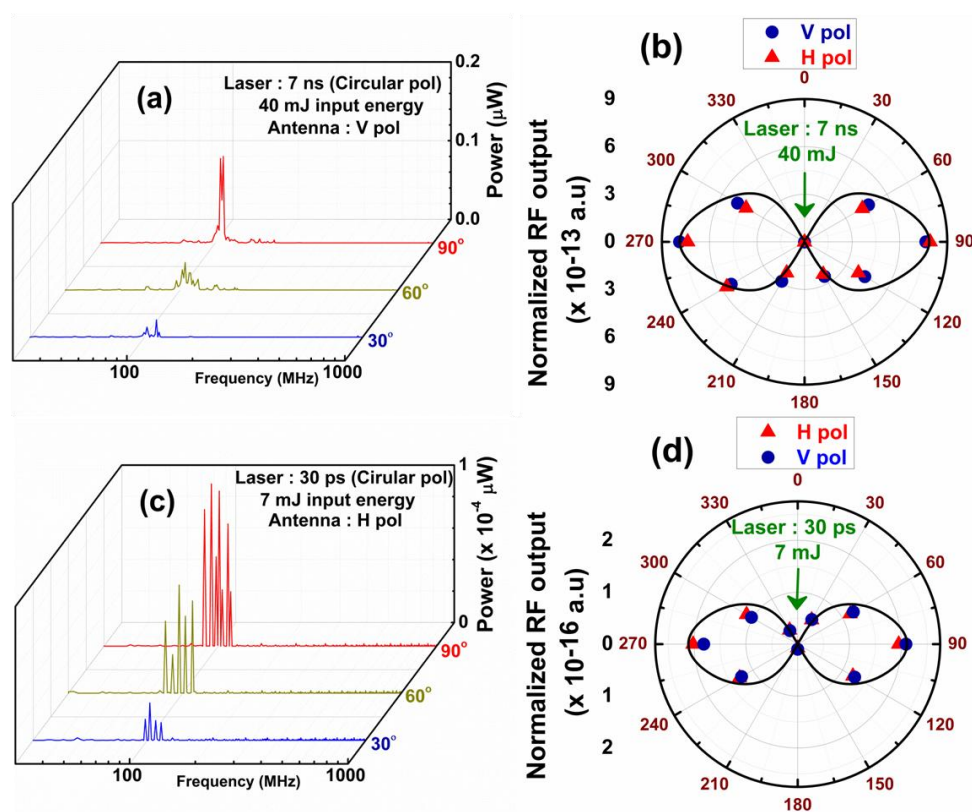


Fig 2.14: RF emissions from circularly polarized LIB of air at different angles of detection (a) at 40 mJ input energy with 7 ns source (c) at 7 mJ input energy with 30 ps source and the corresponding polar plots with (b) 7 ns laser source and (d) 30 ps laser source with different antenna polarizations with the arrows depicting the direction of the input laser pulses.

2.5.3 Positioning of the detector in case of solid targets

To optimize the detector position with solid targets, the angular dependence of RF emissions from the LIB of copper target was studied. Single shot-LIB, where every laser pulse interacts with the fresh sample spot, was ensured with the target mounted on an electronically controlled XY translation stages (M-443, LTA-HA,

Chapter 2: Experimental details

and ESP-300, M/s. Newport). The average of 100 single shot-LIB data was considered for analysis. It was ensured that no air breakdown was happening during laser focusing. The plots are given in Fig 2.15.

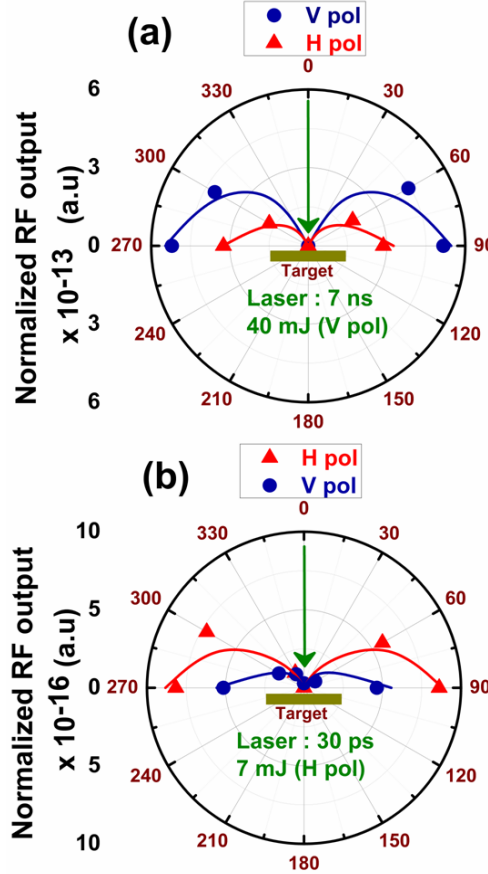


Fig 2.15: Polar plots of RF emissions from LIB of solid (copper) target (a) at 40 mJ input energy with 7 ns source and (b) at 7 mJ input energy with 30 ps source with different antenna polarizations with the green arrows depicting the direction of the input laser pulses.

From the studies on angular dependence of RF emissions with solid samples, the emissions were observed to be maximum when the source and the detector are perpendicular. Hence, the $\sin^2\theta$ dependence of RF emissions was confirmed in case of solid targets as well. Based on the above studies, the detection of RF emissions from ns and ps LIB of the all the targets (presented in the subsequent chapters) were performed with the detector positioned perpendicular to the plasma source.

In summary, the details of the experimental set up and setting up of the experimental diagnostics were presented in this chapter. Besides calibrating the spectrum analyzer with the standard RF signals, the experiments to minimize the

Chapter 2: Experimental details

noise and errors were carried out. After setting up the experiment, the positioning of the antenna was determined by the radial and angular distribution of RF emissions from the LIB of air and copper targets.

Chapter III

Radio emissions from laser induced breakdown of atmospheric air

This chapter contains the results of the studies carried out on the observation and characteristics of RF emissions from ns and ps LIB of atmospheric air.

The interaction of charged particles with the cluster of atoms and molecules results in the emission of low frequency electromagnetic radiation from LIB. Therefore, low frequency emissions take place from the plasma that is far from fully ionized state. The high peak power of ps laser, when compared with ns laser, ensures more ionization. Hence the probability of interaction between the charged species and neutrals is reduced in ps LIB. Thus, the emissions from ns LIB is found to be about 3 orders higher than those from ps LIB. .

The focusing conditions are found to play an important role in the generation of seed electrons and the subsequent RF emissions. The variation of RF emissions with $I\lambda^2$, under different focal geometries, emphasizes the importance of the plasma parameters and the interaction of the plasma constituents in the RF emissions from LIB. The emitted frequencies were observed to correspond to the ion-plasma frequencies confirming the interaction of charged species with neutrals in the RF emission phenomena. The slope of the rise in RF emissions from ns and ps LIB represents the buildup of induced dipole moment with the input laser intensity. Similarly, the slope of the fall in the emissions, with respect to $I\lambda^2$, indicates the damping of radiation that takes place at high input laser intensities due to higher plasma recombination rate. Thus, besides studying the mechanisms, involved in RF emissions from LIB, the optimal intensity conditions to generate RF emissions of appreciable strength were also investigated.

Chapter 3: RF emissions from LIB of atmospheric air

After finalizing the experimental set up and optimizing the experimental conditions that are presented in the chapter 2, the measurement of RF emissions from LIB of different materials is the next step. In this chapter the interaction of laser with atmospheric air and its subsequent effects on the emission of low frequency radiation are presented. Atmospheric air is composed of different elements (N, O, H etc.) and many other impurities (like aerosols and other pollutants), with Nitrogen being the major component [119].

Optical breakdown is generally signified by a spark due to plasma formation. The spark in case of gas targets (compared with solid and liquid targets) can extend over a long distance as the volume of expansion of plasma in the LIB of gases is high [10,120]. The breakdown of atmospheric air takes place in two steps: creation of primary electrons and development of avalanche process of ionization [5]. Due to the presence of impurities in the atmospheric air, the laser intensity required to create initial free electrons becomes much lower. The avalanche ionization is controlled by these primary electrons [5]. After the breakdown, the electrons in the plasma can readily absorb more energy from the laser field. This rapidly heated plasma leads to the formation of an expanding shockwave [10]. It is important to understand the role of the primary electrons and laser-plasma interaction dynamics to uncover the physics involved in the emission of low frequency radiation from LIB.

The RF emissions (30 – 1000 MHz) from 7 nanosecond (ns) and 30 picosecond (ps) laser induced break breakdown (LIB) of air were recorded. Both the 7 ns and 30 ps laser beams (532 nm) were focused with the same lens in the focal geometry (f/D) ~ 10 and 6.5 in the ns and ps regimes respectively. The laser energy was in the range of 5-200 mJ with the ns pulses and 4-38 mJ with the ps pulses. An average of RF spectra over 100 laser shots was obtained.

3.1 Results

3.1.1. Effect of antenna polarization

The polarization state of ns and ps laser pulses was vertical and horizontal, respectively. To study the polarization effects, the antenna was rotated to measure

the H-pol and V-pol components of emissions. The RF emissions from ns and ps LIB of atmospheric air, with different antenna polarizations, are shown in Fig 3.1.

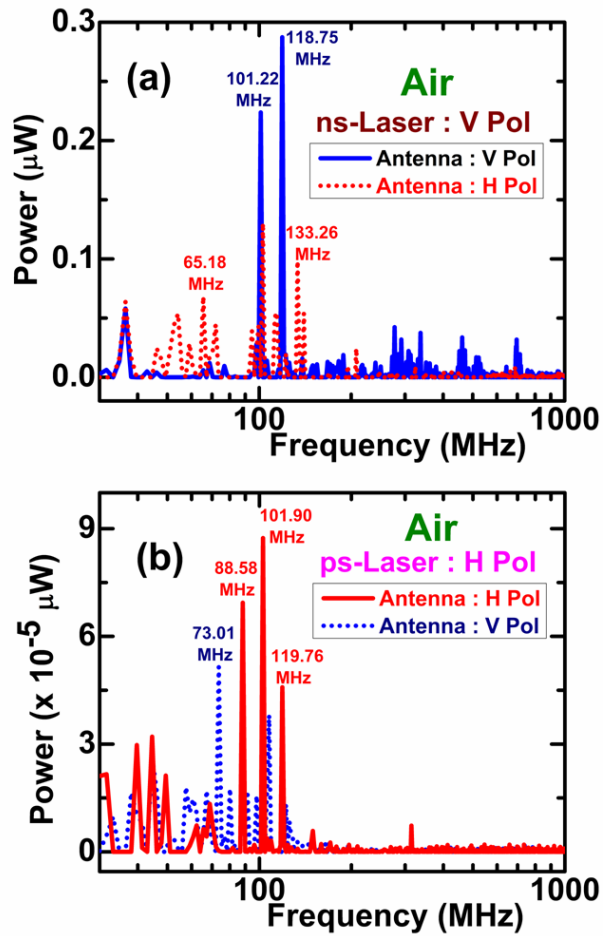


Fig 3.1: RF emissions from (a) 7 ns LIB and (b) 30 ps LIB of atmospheric air at 20 mJ laser energy with different antenna polarizations.

With both ns and ps LIB, the emitted frequencies were observed to vary with antenna polarization. In case of ns LIB of air, most of the lines below 100 MHz were missing with V-pol antenna unlike that with H-pol antenna. Also, the frequencies beyond 200 MHz were observed only with V-pol antenna. The amplitude of the prominent peaks with V pol antenna was observed to be almost double that compared to the corresponding peaks with H pol antenna (Fig 3.1a). In case of ps LIB of air, most of the emissions from V-pol and H-pol antennas were observed to be within 125 MHz with amplitude of lines with H-pol antenna relatively higher than those with V-pol antenna (Fig 3.1b). The lines and their corresponding amplitudes from ns and ps LIB are given in tables 3.1 and 3.2.

Chapter 3: RF emissions from LIB of atmospheric air

Table 3.1: Lines and their amplitudes from 7 ns LIB of air with different antenna polarizations.

Laser polarization: Vertical.

V pol antenna		H pol antenna	
Frequency (MHz)	Power (μW)	Frequency (MHz)	Power (μW)
36.48	0.056	36.48	0.065
101.22	0.225	46.66	0.025
118.75	0.288	54.32	0.053
275.02	0.044	65.18	0.067
291.34	0.033	71.50	0.043
313.23	0.024	101.66	0.129
336.77	0.039	133.26	0.097
459.91	0.035	140.29	0.055
516.52	0.018	207.43	0.024
695.01	0.034	-	-

Table 3.2: Lines and their amplitudes from 30 ps LIB of air with different antenna polarizations.

Laser polarization: Horizontal.

V pol antenna		H pol antenna	
Frequency (MHz)	Power ($\times 10^{-4} \mu\text{W}$)	Frequency (MHz)	Power ($\times 10^{-4} \mu\text{W}$)
33.40	0.974	31.07	2.20
37.78	1.642	39.46	3.05
45.26	2.23	44.63	3.24
57.08	1.75	49.39	2.15
60.47	1.43	88.58	6.97
67.44	1.67	101.90	8.87
73.01	5.17	119.76	4.69
79.61	1.69	148.45	0.63
92.02	1.64	315.27	0.81
97.56	1.54	-	-
107.95	3.81	-	-
122.94	1.400	-	-

From the tables, the role of antenna polarization in picking up the signals becomes evident. The lines with same laser and antenna polarizations, besides having higher amplitudes, were observed to be better resolved than those with cross polarizations. Hence, all the analyses were emphasized with similar laser and antenna polarization conditions.

3.1.2. RF spectra from ns and ps LIB of atmospheric air

The RF emission spectra from the ns and ps LIB of atmospheric air, under similar experimental conditions, with same laser and antenna polarization, are given in Fig 3.2.

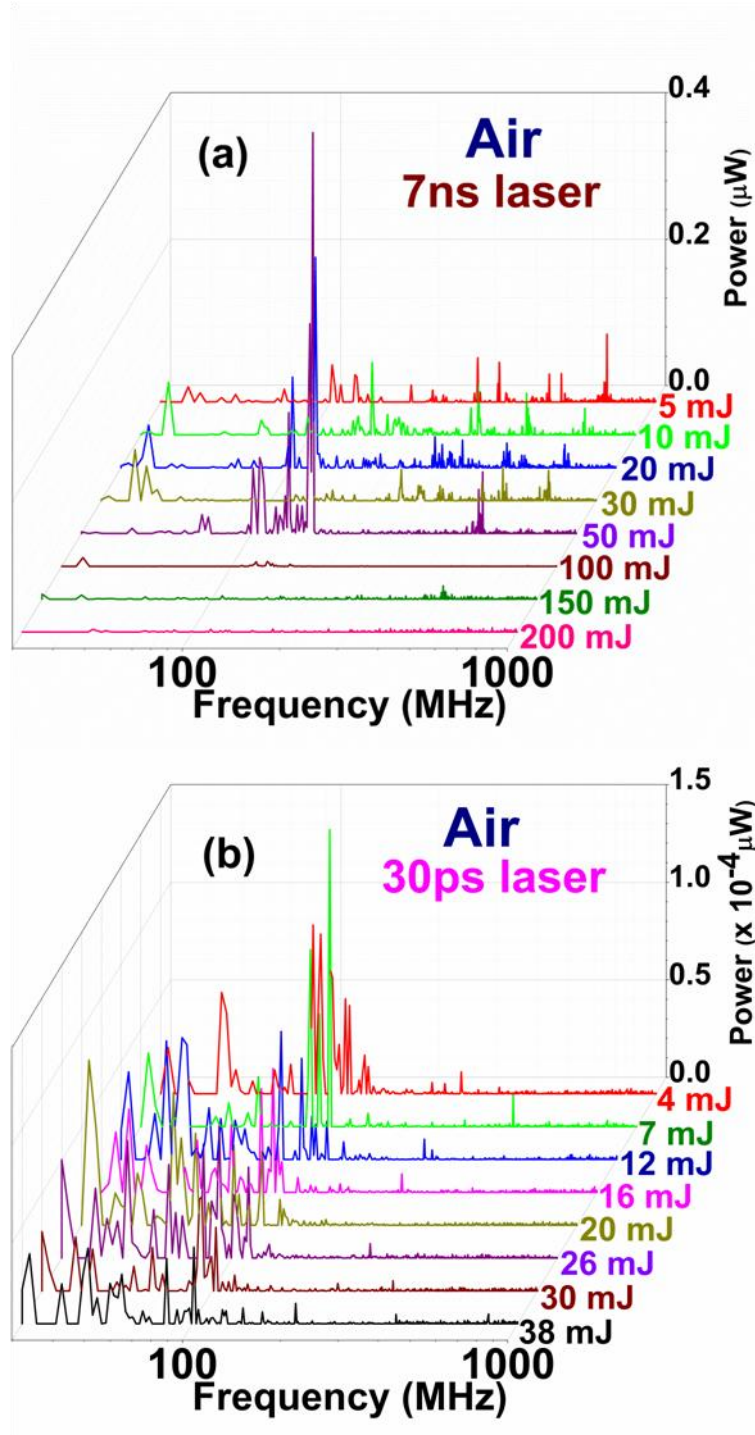


Fig 3.2: RF emissions from (a) 7 ns LIB (b) 30 ps LIB of atmospheric air with same laser and antenna polarization

The RF emission spectra, consist of many frequency lines over the entire detection range of the antenna used. The emissions were observed to be over 30-710 MHz and 30-120 MHz with ns and ps laser sources respectively. The maximum amplitude of emissions from ns and ps LIB were observed to be around 154 MHz and 102 MHz respectively. The amplitude of emissions was observed to vary with respect to the input laser energy. This is shown in Fig 3.3 where, the variation of normalized RF emissions was plotted with respect to input laser energy.

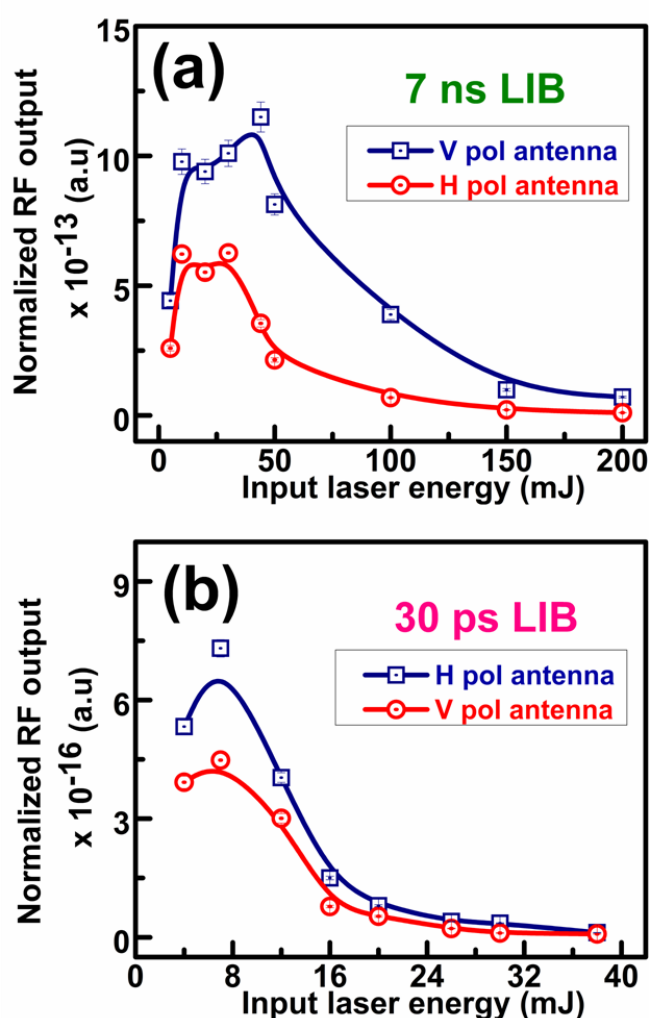


Fig 3.3: Normalized RF emissions at different input laser energies for different antenna polarizations with fixed laser pulse duration (a) 7 ns LIB (b) 30 ps LIB of atmospheric air

The RF emissions were observed to be increasing upto certain input laser energy. The emissions, after attaining the maximum at particular

input laser energy, were observed to fall at higher input laser energies (Fig 3.3). From 7 ns LIB, the RF emissions were observed to be increasing with input laser energy before attaining the maximum at the laser energy of 50 mJ. Similarly, with 30 ps LIB, the maximum of RF emissions was attained at input laser energy of 7 mJ. The effect of pulse duration, at different antenna polarizations, is depicted in Fig 3.4. With both V-pol and H-pol antenna, the amplitude of RF emissions from ns LIB was observed to be three orders higher than that from ps LIB.

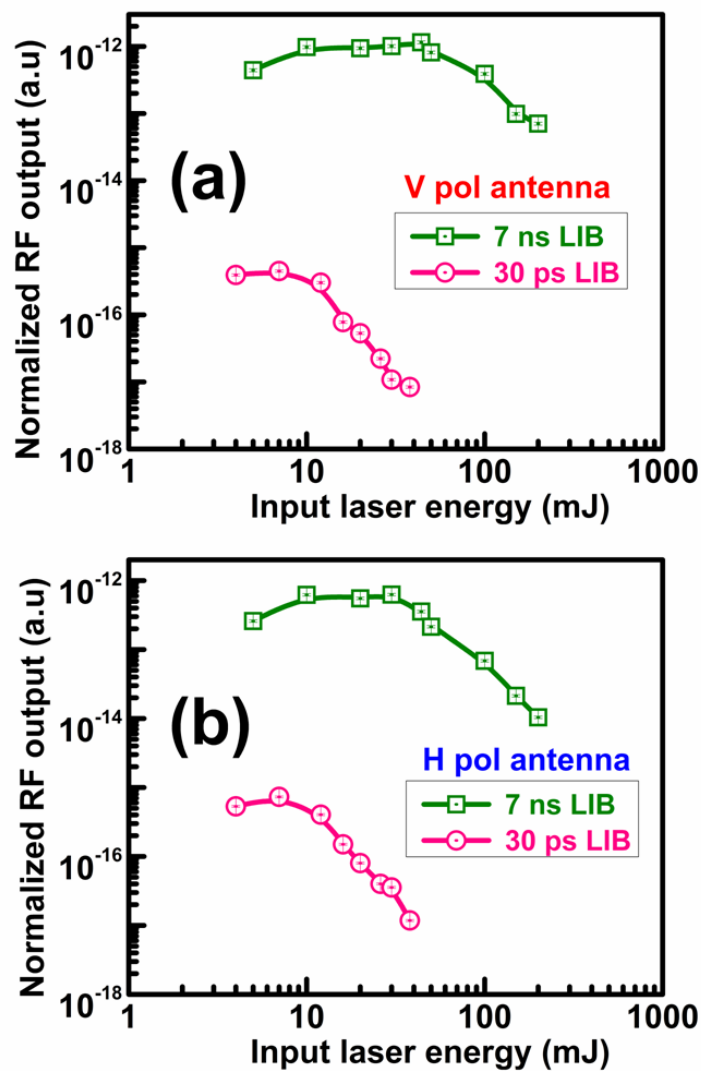


Fig 3.4: Normalized RF emissions at different input laser energies from sources of different pulse durations for a fixed antenna polarization (a) 7 ns LIB at V pol antenna and (b) 30 ps LIB at H pol antenna of atmospheric air as a function of input laser energy

3.2 Emission mechanism

Before discussing the results, it is important to understand the origin of RF emission from LIB. The interaction of the plasma constituents in the depth of focus of the laser pulse, which is twice the Rayleigh range (Z_R), is depicted in fig 3.5.

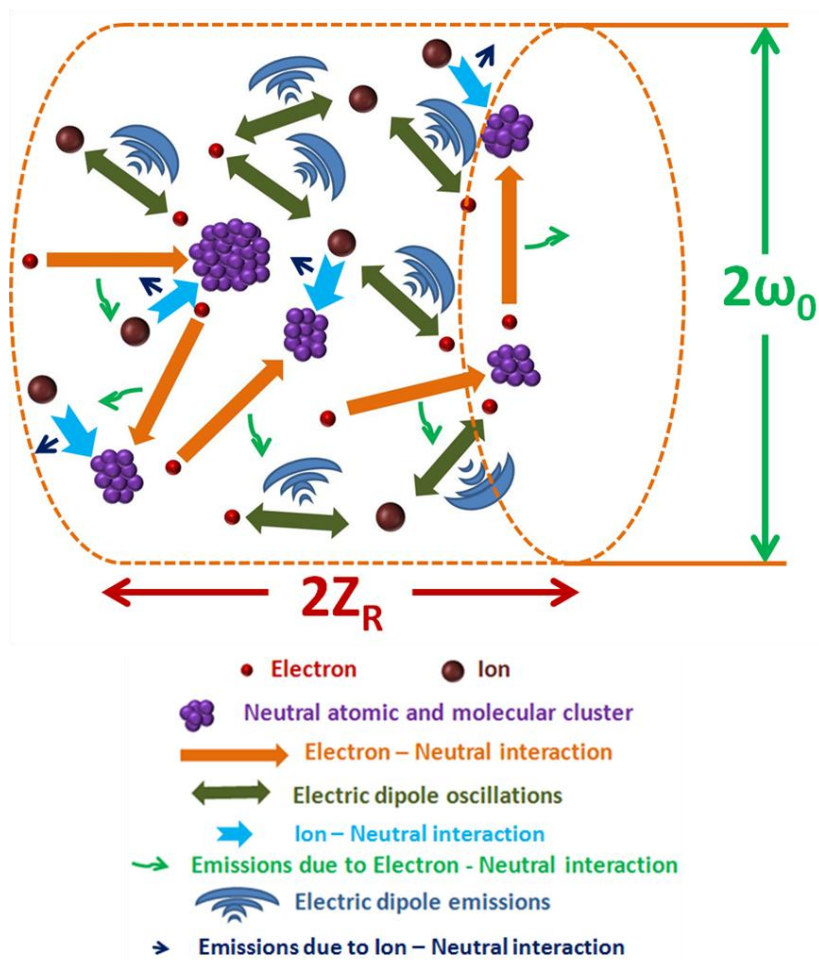


Fig 3.5: Mechanism of RF emissions from the focal volume of the plasma. $2w_0$ is the beam diameter at the focal plane

The nature of RF emissions from LIB depends on two major factors: (a) properties of the plasma due to laser pulse - matter interaction like degree of ionization, which decide plasma constituents (electrons, ions, neutral atomic and molecular clusters) and (b) the instabilities that create charge separation within the plasma and damping of the charge oscillations [121]. These two phenomena give an insight into the RF emissions and the total power emitted, respectively. In order to understand the phenomenon better, it is important to understand the timing

diagram of the pulsed laser matter interaction. In fig 3.6, the timing diagram of the pulsed laser matter interaction for a laser pulse of 532 nm wavelength and 10 ns pulse duration is given [122].

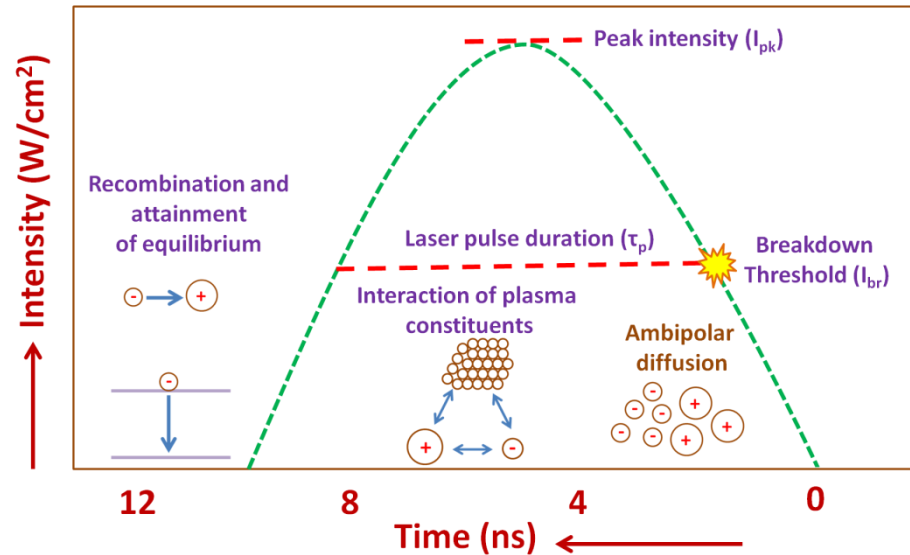


Fig 3.6: Generic temporal view of pulsed laser matter interaction leading to RF emissions

When the laser intensity is beyond the breakdown threshold of the material with which it interacts, laser induced breakdown takes place. Thus, as shown in Fig 3.6, the leading edge of the laser pulse creates the plasma and the rest of the pulse interacts with the plasma. At around 2-4 ns, electron diffusion will be dominant at very low time scales if the focal volume is about 100 times less than the mean free path of the electrons. For higher focal volumes, electron diffusion goes down. During the laser matter interaction (in the FWHM range), most of the laser energy is absorbed by the plasma. The electron – ion and electron – neutral interactions are dominant in this region. The interaction between the charged particles and the neutral atomic and molecular clusters, in plasma, results in the emission of low frequency radiation. During this interaction, secondary electrons are emitted which further interact with neutrals to emit radiation. Thus, the avalanche of ionization and subsequent radiation emission take place till the plasma cools down to attain equilibrium. Hence, it is clear that the low frequency emissions take place from the plasma that is far from fully ionized state [123]. Besides emissions due to interaction of charged particles with neutrals, the instabilities in the plasma and the subsequent interaction between electrons and ions yield electromagnetic emissions which are due to dipolar oscillations (Fig. 3.6). The recombination

starts once the interaction between the pulse and the plasma is over. The time domain information of RF emissions, which is obtained by taking the IFFT of the frequency domain information, is given in Fig 3.7. The emissions were observed to happen after several nanoseconds upto 500 ns where the recombination and the equilibrium attainment of the plasma happen.

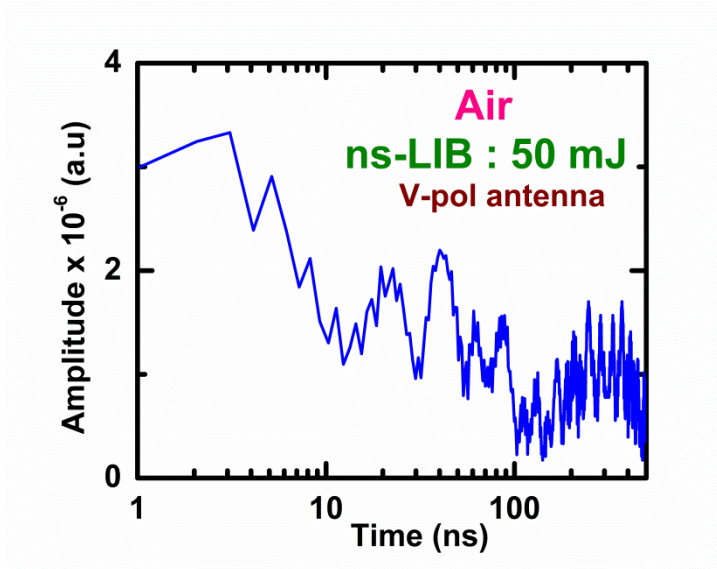


Fig 3.7: RF signals in time domain from 7 ns LIB of air at 50 mJ laser energy

3.3 Discussion

3.3.1 Effect of pulse duration

The RF emissions from LIB (Fig. 3.2) suggests the interaction of charged particles with neutrals which results in the avalanche ionization. As the peak power of the ps pulses is higher than that of the ns pulses by about two orders of magnitude, under similar conditions, the electron density of the plasma due to the ps-LIB of the target material is much higher than that due to the ns-LIB [124]. LIBS experiment, with the atmospheric air as the target material, was carried out with the 7ns laser system and the n_e values were estimated from the stark broadening [14] of the spectral lines. The typical value of n_e in the case of ps LIB of air obtained from literature [14]. The ratio of plasma frequency to the laser frequency (ω_p/ω_L) in case of ns LIB and ps LIB were calculated and are given in table 3.3.

Table 3.3: Values of n_e and ω_p in ns and ps LIB of atmospheric air

LIB	Input laser intensity (W/cm²)	Values of electron density (n_e), plasma frequency (ω_p) and the ratio (ω_p/ω_L)	
ns LIB	$\sim 3.15 \times 10^{10}$	$n_e \times 10^{15} \text{ cm}^{-3}$	8.34
		$\omega_p \times 10^{12} \text{ Hz}$	5.15
		ω_p/ω_L	0.01
	$\sim 1.27 \times 10^{11}$	$n_e \times 10^{16} \text{ cm}^{-3}$	9.26
		$\omega_p \times 10^{13} \text{ Hz}$	1.72
		ω_p/ω_L	0.03
ps LIB	$\sim 10^{13}$	$n_e \times 10^{18} \text{ cm}^{-3}$	1
		$\omega_p \times 10^{13} \text{ Hz}$	5.64
		ω_p/ω_L	0.13

The ratio of plasma frequency to the laser frequency (ω_p/ω_L) with ns LIB at intensity $1.27 \times 10^{11} \text{ W/cm}^2$ is thrice as much as that at intensity $3.15 \times 10^{10} \text{ W/cm}^2$. The ionization and consequently the plasma density are very high at higher energies such that the probability of the charge neutral interaction and subsequently the RF emissions is low. With the ps pulses, when the target is focused at intensity of the order of 10^{13} W/cm^2 , the electron densities were very high such that ratio (ω_p/ω_L) is several times higher than that with ns pulses. The ratio (ω_p/ω_L) with ps LIB at intensity of the order of 10^{13} W/cm^2 is 0.13. This is almost 10 times more than that with ns LIB. As a result of this intense ionization, the probability of interaction between the charged particles with neutral atoms and molecules reduces. Thus, the thermalization time, inversely proportional to the electron density of plasma [125], due to the ps-LIB is lesser compared to ns-LIB. Hence, the RF emissions from 7 ns-LIB are observed to be higher than that from

the 30 ps-LIB by about three orders of magnitude [123]. The origin of the emitted frequencies is presented in the following section.

3.3.2 Dependence of RF emissions on focusing conditions

Though the LIB threshold of air [126] is of the order of 10^{12} W/cm², the presence of impurities and aerosol particles in ambient air are known to reduce the breakdown threshold by two or three orders of magnitude [127]. When the focusing conditions are altered, the breakdown threshold also varies accordingly. Thus different focal volumes give rise to different input laser intensities at same laser energies (Fig 3.8).

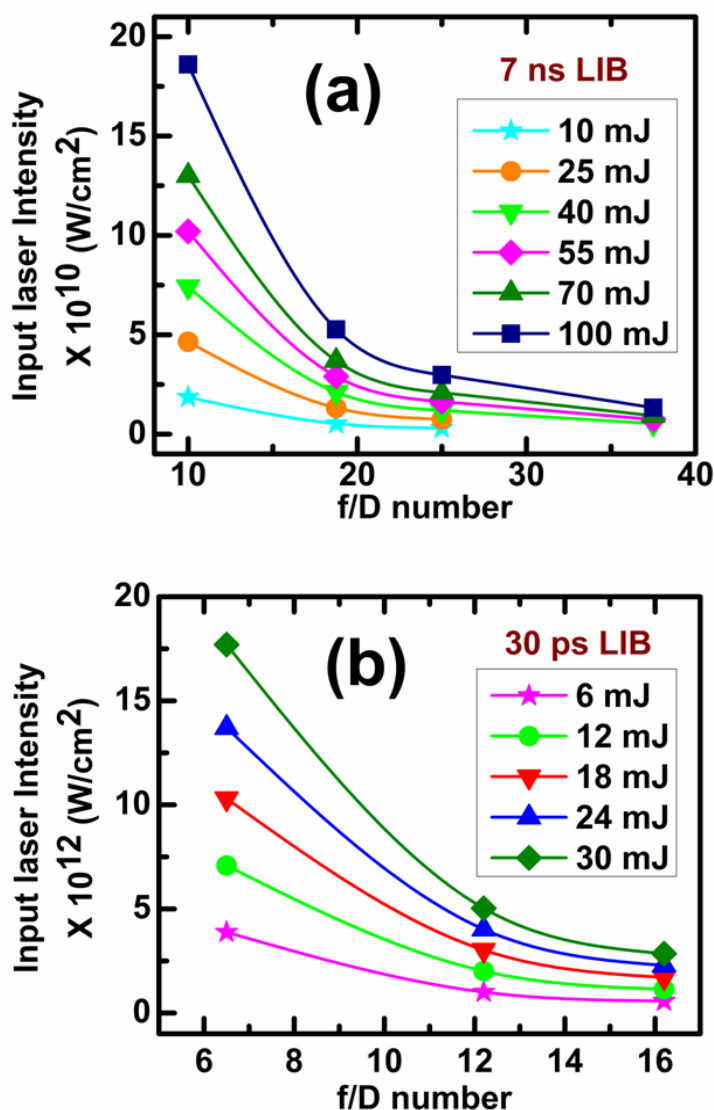


Fig 3.8: Variation of input laser intensity with respect to focal geometry

Chapter 3: RF emissions from LIB of atmospheric air

With both ns and ps LIB, for particular input laser energy, the laser intensity values are relatively higher in the tight focusing geometries. Also, for the input laser energies studied, tight to loose focusing correspond to broad to narrow ranges of intensity respectively. Based on the above discussion, it is understood that the degree of ionization, hence the plasma parameters and the subsequent effects, can be modified by tuning the focusing conditions of the laser. Hence, in order to study the effect of plasma parameters on RF emissions from LIB, the experiments were carried out by focusing the laser beam using converging lenses of different focal lengths (80 mm – 300 mm) leading to the focusing geometries (f/D) in the range of 10-37.5 and 6.5-16.2 in the ns and ps regimes respectively. The RF emission spectra from the ns and ps LIB of atmospheric air at various input laser energies under different focusing conditions are shown in Fig 3.9, 3.10 and 3.11.

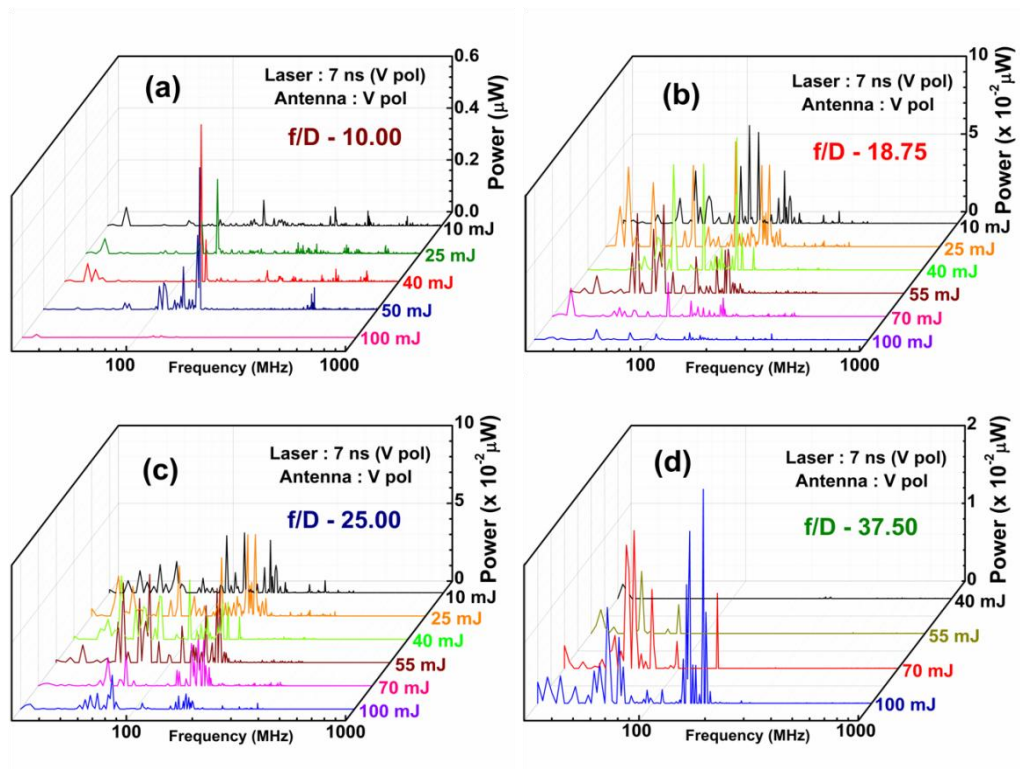


Fig 3.9: RF emissions under different focusing geometries from ns LIB of air

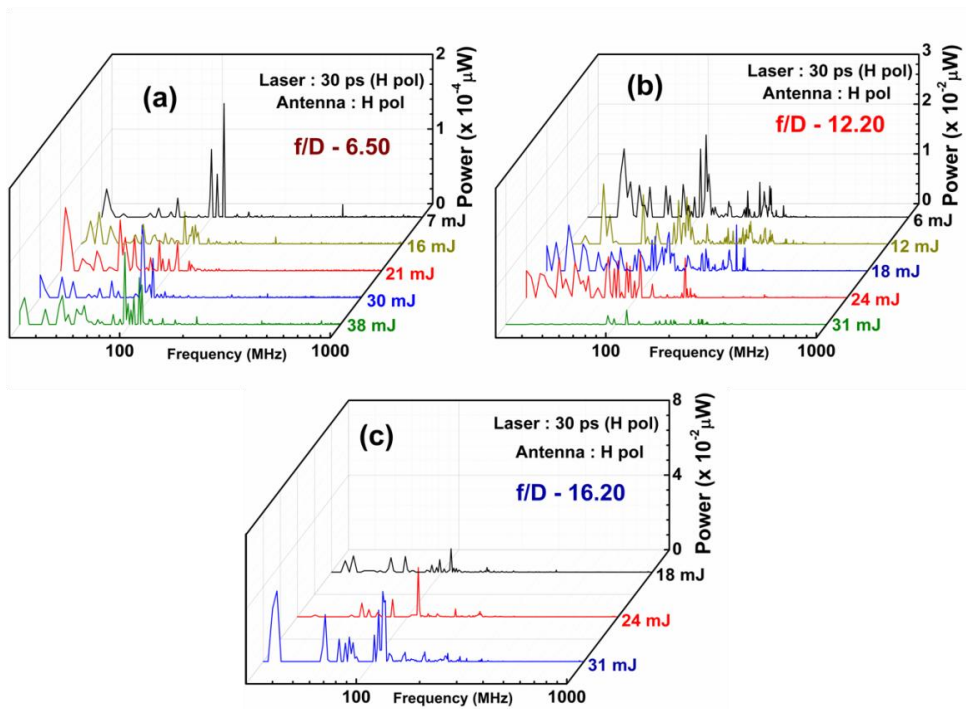


Fig 3.10: RF emissions under different focusing geometries from ps LIB of air

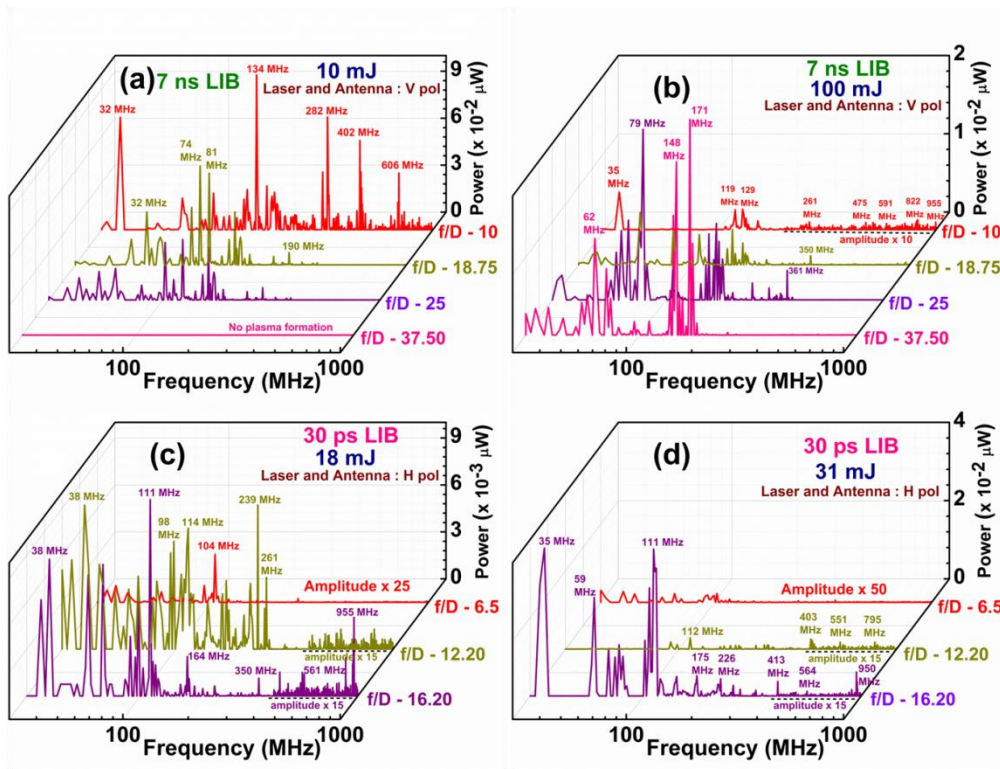


Fig. 3.11: RF emissions from 7 ns LIB at (a) 10 mJ (b) 100 mJ and 30 ps LIB at (c) 18 mJ (d) 31 mJ of air under different focusing geometries. For ns-LIB the laser and antenna are V-Pol and for ps-LIB the laser and antenna are H-Pol. The amplitude of entire spectra due to $f/D \sim 6.5$ of Fig 3.11(c) and 3.11(d) is multiplied for better viewing. The amplitude of spectra due to $f/D \sim 10$ in Fig 3.11(b), $f/D \sim 12.20$, 16.20 in Fig 3.11(c) and 3.11(d) is multiplied in the 400-1000 MHz frequency range for better viewing.

Chapter 3: RF emissions from LIB of atmospheric air

With ns and ps LIB under tighter focusing, the breakdown was observed to happen at lower input laser energies confirming the importance of the generation of seed electrons in the breakdown process. The emitted frequencies were observed to be strongly dependent on the laser parameters (pulse duration, input laser energy etc.) and the focusing conditions. In case of ns LIB at 7 mJ input laser energy, when the focusing geometry (f/D) is varied from 10 to 25 (tight to loose), the dominant frequencies were observed to be limited upto ~ 800 MHz and 200 MHz respectively (Fig 3.11(a)). This effect is observed to be reversed at 100 mJ input laser energy, where the dominant emissions were observed to be limited upto ~ 150 MHz and 400 MHz when the focusing geometry is varied from 10 to 25 respectively (Fig 3.11(b)). Under very loose focusing (f/D 37.5), the dominant emissions were confined upto 200 MHz. The dominant frequencies from ps LIB (both at 18 mJ and 31 mJ input laser energy) were observed to be limited upto ~ 100 MHz under tight focusing (f/D 6.5) and ~ 350 MHz under loose focusing (f/D 16.2) conditions (Fig 3.11(c) and Fig 3.11(d)). The amplitude of emissions was also observed to vary with the laser parameters. In case of ns LIB, at lower input laser energies, the emissions were observed to be higher under tight focusing with the amplitudes coming down at loose focusing conditions (Fig 3.11(a)) as the number of seed electrons and their corresponding energies are too low to propel cascade of ionization which results in RF emissions. At low laser energies (10 mJ), under loose focusing conditions ($f/D = 37.5$), no breakdown was observed. At higher input laser energies, the amplitude of RF emissions from ns LIB was observed to be higher under the loose focusing geometries (Fig 3.11(b)) with an order of difference in amplitude between the emissions in f/D 10 and 37.50. Thus, in order to have appreciable RF emissions from ns LIB, the input laser pulses need not be tightly focused. In case of ps LIB, the emissions were observed to be increasing when traversed from tight to loose focusing geometries (Fig 3.11(c)) with two orders of difference in the amplitude under the extreme conditions of focusing (Fig 3.11(d)). Thus, the favourable intensities that are required to generate detectable RF signals from ps LIB can be achieved under loose focusing conditions.

The emissions from plasma depend on the plasma number density (n_e, n_i) which in turn depends on the laser parameters (energy, pulse duration etc.) and the

recombination process of plasma. The interaction of the plasma constituents will result either in the growth (further ionization) or decay (recombination) of plasma and the corresponding energy release. The outcome of the collisional interaction between electrons and ions depends upon the energy of the electrons. The collisions between electrons, of low relative velocity, with ions (which is common in underdense plasmas) will lead either to radiative recombination (with the emission of photon) or three body recombination (with the emission of a particle) [116]. In case of collisions between high energy electrons and ions, the emission of radiation will fall in high frequency (X-ray) region of the electromagnetic spectrum [12]. In underdense plasmas, as in our case, the interaction of charged particles with neutral atoms and molecules will be dominant [127]. These charge-neutral interactions give rise to emissions in the RF and microwave range of frequencies [117, 123, 128]. Therefore, the RF emissions take place as long as there is interaction between the charged particles and the neutrals in the system. Thus, the RF emissions were observed to be dominant at moderate intensities where the charge-neutral interaction remains higher. As the ionization is intense with the ps pulses, which have relatively higher peak power when compared to the ns pulses, the probability of charge-neutral interaction and the emitted RF powers are lower. In the plasma, the electrons and ions oscillate with their characteristic frequencies. The electron plasma frequency (ω_{pe}) values, under different focusing conditions, were calculated from their respective n_e values as in reference 123. Similarly, the ion plasma frequencies (ω_{pi}) and Debye lengths (λ_D) were estimated using the following equations [127].

$$\omega_{pi}^2 = \frac{n_i Z^2 e^2}{m_i \epsilon_0} \quad (3.1)$$

$$\lambda_D = \sqrt{\frac{\epsilon_0 T_e}{n_e e^2}} \quad (3.2)$$

where n_i and n_e are the ion and electron number densities respectively, T_e is the plasma temperature, Z and m_i are the charge state and mass of the ions respectively. In our case, the atoms in the atmosphere are considered to be singly ionized. Therefore Z is taken to be one and hence $n_e = n_i$. The mass of the N_2^+ ion

Chapter 3: RF emissions from LIB of atmospheric air

(since N₂ is the major atmospheric constituent) is taken to be 2.33×10^{-26} kg. The estimated plasma parameters are given in table 3.4.

Table 3.4. Values of electron density (n_e), electron plasma frequency (ω_{pe}) and ion plasma frequency (ω_{pi}) in ns and ps LIB under different focusing conditions

Parameters	$I\lambda^2$ (Wcm ² μm ²)	f/D #	Electron density $n_e \times 10^{15}$ (cm ⁻³)	Electron plasma frequency $\omega_{pe} \times 10^{12}$ (Hz)	(ω_{pe}/ω_L) $\times 10^{-2}$	Ion plasma frequency ω_{pi} (MHz)	Debye length $\lambda_D \times 10^{-8}$ (m)
7 ns LIB	$\sim 10^{10}$	10.00	8.34	5.15	1	85.5	7.5
		18.75	4.45	3.76	0.8	62.4	10.3
		25.00	3.36	3.27	0.7	54.3	11.9
		37.50	2.24	2.67	0.5	44.3	14.5
	$\sim 5 \times 10^{10}$	10.00	92.6	17.2	3.4	284.8	22.6
		18.75	49.4	12.54	2.5	208.0	3
		25.00	37.0	10.85	2.2	180.0	3.6
		37.50	24.7	8.86	1.8	147.1	4.4
30 ps LIB	$\sim 3 \times 10^{12}$	6.50	1000	56.4	11.3	935.9	0.69
		12.20	530	41.06	8.20	681.4	0.94
		16.20	401	35.72	7.10	592.7	1.09

The oscillating charged species, colliding with neutrals, of the mass almost closer to that of the ions, results in the emission of RF frequencies that are closer to the ion plasma frequencies (ω_{pi}) given in table 3.4. In our experiments, almost all the frequencies closer to ω_{pi} , falling in the 30-1000 MHz range, is observed (Fig 3.11). Owing to relatively smaller velocity of the charged particles (electrons and ions) that collide with the neutrals, the RF power of high frequency emissions (400-1000 MHz) is relatively lower than that of the low frequency emissions (30-400 MHz). The value of ω_{pe} ($\sim 10^{12}$ Hz in case of ns LIB and $\sim 10^{13}$ Hz in case of

ps LIB) are way too higher than the detected RF emission frequencies (which are of the order of 10^6 Hz). The RF emission frequencies well below the characteristic electron plasma frequency, suggests the existence of macroscopic charge fluctuations in the plasma expansion [69]. The plasma while expanding gives rise to the charge separation between electrons and ions, due to drift instability, as the drift velocity of the electrons (~ 1500 m/s) are higher than that of the ions (~ 5 m/s) [99]. This gives rise to induced dipoles within the Debye length (table 3.4) and subsequent emission of radiation [127]. Thus, besides the emissions due to charge-neutral interactions, oscillations of these induced dipoles give rise to the RF emissions. In underdense plasmas, due to such huge velocity difference between the electrons and ions, the electron-ion recombination rate will vary reciprocally with time [116, 127]. This controls the collisions of the charged particles with neutrals and the emission of RF radiation due to induced dipole moments. Increase in these charged particle quasi neutral dipole oscillations tends to increase the RF emissions until the recombination dominates. From these results, it can be understood that the RF emissions from LIB strongly depend on the degree of ionization which in turn depends on the input laser parameters.

When the input laser intensity (by varying the laser pulse duration, input laser energy and focusing conditions) is increased the RF emissions tend to increase as the plasma frequency (ω_p) and dipole moment (p) increase. However, after a certain value of input laser intensity, the damping of plasma brings down the emission of radiation. The damping of the plasma oscillations is predominantly due to collision/recombination and electron-attachment [127]. According to the recombination model [116], the loss of plasma by recombination is proportional to the product of electron and ion number densities ($n_e n_i$). Therefore, the rate of recombination is given by

$$\frac{\partial n}{\partial t} = -\alpha n_e n_i \quad (3.3)$$

where α is the recombination coefficient. After the plasma density becomes lower than its initial value, it decays reciprocally with time ($n \propto 1/\alpha t$). At lower input laser intensities, the number of charged species and their velocities in the underdense plasma is relatively lower and hence the charge particle-neutral

Chapter 3: RF emissions from LIB of atmospheric air

collisions are dominant. In this case, the relaxation time for the kinetic energy of the electrons is longer than that for the average velocity (of the ions and neutrals) by a factor of (m_n/m_e) [116, 127]. Thus at lower laser intensities, n_e (n_i) increases which leads to the increase in ω_{pe} (ω_{pi}) with lower recombination of the plasma. The dipole moment (p) given in equation 2.1, increases with input laser intensity. As a result of this, the RF emissions keep growing with input intensity. At higher laser intensities, the higher value of n_e (n_i) leads to the interaction between low energetic electrons and ions. In this case, recombination will take place at a faster rate when compared to that in plasmas due to lower input intensities reducing the plasma density more drastically. Therefore, the RF emissions were observed to be higher at moderate input intensities.

The RF emissions from LIB depend upon the plasma parameters which in turn depend upon the laser parameters. The major breakdown mechanism with ns laser pulses is avalanche ionization where electrons, interacting with the neutrals, get multiplied in the system under the influence of the laser electric field. The relatively lower pulse duration and higher peak intensity of ps pulses gives rise to intense breakdown compared to that with ns pulses. Hence ionization is the major contribution of breakdown with ps laser pulses. Translating these ideas, the breakdown threshold, beyond which the material gets broken down into plasma state is given by [6, 129]

$$I_{br} \propto \frac{mc\xi_i(1 + \omega^2\tau^2)}{2\pi e^2\tau} \left[g + \frac{1}{\tau_p} \log_e \left(\frac{\rho_{cr}}{\rho_0} \right) \right] \quad (3.4)$$

where, τ_p is the laser pulse duration, ω is the optical frequency, τ is the momentum transfer collision time, m is the electron mass and ξ_i is the ionization energy of the atoms or molecules. The term ‘ g ’ refers to the rate of loss of electron ($\partial n_e/\partial t$) due to diffusion, recombination etc., ρ_{cr} and ρ_0 are the critical and pre ionized densities of the medium respectively. As per equation (3.4), the breakdown with 7 ns pulses were observed to happen at lower intensities ($\sim 10^{10}$ W/cm²) than that ($\sim 10^{12}$ W/cm²) with 30 ps laser pulses. When the target is composed of combination of different elements, the seed electrons for breakdown will be contributed by the element that has the least ionization potential [126]. Thus, the impurities in the target, which tend to increase the pre ionized density (ρ_0), decrease the breakdown

threshold [130]. Under tight focusing conditions, when the focal volume is low, the electron loss due to diffusion out of the focal volume during the laser pulse should be more [6]. Therefore, the electron loss rate ‘g’ will be larger and hence the breakdown threshold (I_{br}) is high under tighter focusing geometries as per equation 3.4. Thus different focal volumes, which correspond to different ‘g’ values, give rise to different input laser intensities at same laser energies. Therefore, the degree of ionization, hence the plasma parameters and the subsequent effects, can be modified by tuning the focusing conditions of the laser. The expected profiles of the plasma due to ns and ps LIB under different focusing conditions can be visualized as shown in fig 3.12.

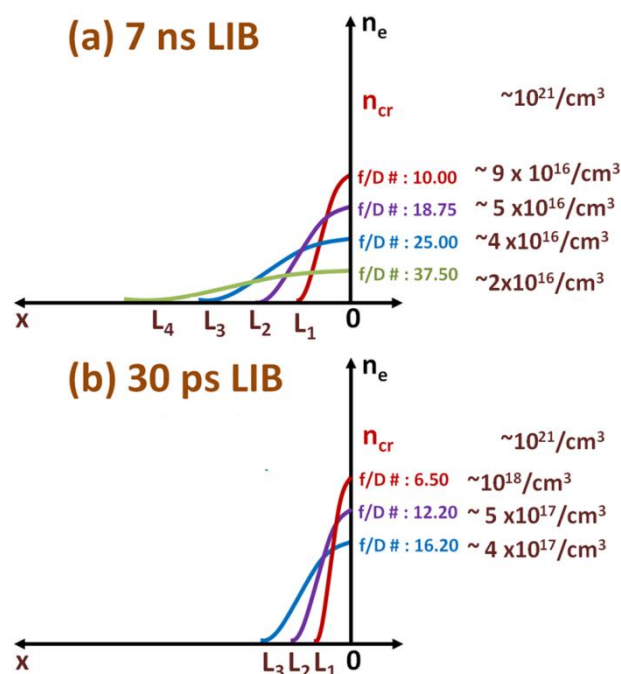


Fig.3.12. Expected plasma profiles under different focusing conditions for (a) 7 ns and (b) 30 ps LIB of air. The laser propagation direction is from $x \rightarrow 0$. The values of n_e corresponding to different f/D numbers are given in table 3.4. The varying plasma profiles indicate that the plasma recombination is relatively slower with ns-LIB and faster with ps-LIB. n_{cr} is the theoretical estimate of electron density, which is 3-5 orders more than that observed in the experiments, beyond which the plasma becomes opaque to the incident radiation.

Under similar experimental conditions, the emissions from ns LIB were observed to be two orders higher than those from ps LIB where, the intense breakdown [124] reduces the probability of interaction of charged particles with the neutrals. As depicted in fig 3.12, the focal volume, which alters the interaction strength of

Chapter 3: RF emissions from LIB of atmospheric air

the plasma constituents, varies as a function of focal geometry (f/D). Hence, in order to compare the results under different f/D , the total RF emissions (integrated over the entire band of detection) were normalized with respect to the focal volume and the solid angle subtended by the detector. The typical values of electron densities (n_e) at the maximum input laser intensity studied in case of ns and ps LIB (from table 3.4) are given in Fig 3.12. The critical density (n_{cr}) for 532 nm laser radiation is $\sim 10^{21}/\text{cm}^3$. In our experiments the value of n_e is observed to be in the range of 10^{16} to $10^{18} /\text{cm}^3$ which is three to five orders of magnitude smaller than the n_{cr} . Consequently, the plasma frequency (ω_p), at higher input laser intensities becomes three times higher than that at lower input laser intensity. The numbers suggest that the plasma is well under the critical values and therefore, there cannot be reflection of the input laser radiation. This is clear from the ratio (ω_{pe}/ω_L) given in table 3.4. The fall in RF emissions at higher laser intensities can be understood from the damping of plasma due to collision/recombination as explained by equations 3.3 and 3.4. The normalized RF output was plotted as a function of $I\lambda^2$ (Fig 3.13), where I is the laser intensity and λ is the wavelength of the input laser radiation in micron.

According to equation (3.4), the breakdown threshold (I_{br}) is proportional to the collision term 'g', which is inversely proportional to the focal geometry. Accordingly, at similar input laser intensities, under different focusing conditions, RF emissions with different amplitudes were observed. In case of ns-LIB, at similar input laser intensities, the RF emissions were observed to be increasing when traversed from loose to tight focusing conditions. This is because of the increase in the number of electrons under tighter focusing conditions. For example, in the ns LIB at the input intensity $\sim 6 \times 10^9 \text{ Wcm}^{-2} \mu\text{m}^2$, the RF emissions under f/D 10 is almost two orders higher than those under f/D 25 (Fig 3.13(a)). In case of ps-LIB, the RF emissions were observed to be decreasing under tighter focusing conditions (Fig 3.13(b)). This is because of the excessive ionization that reduces the charged particle-neutral interaction probability.

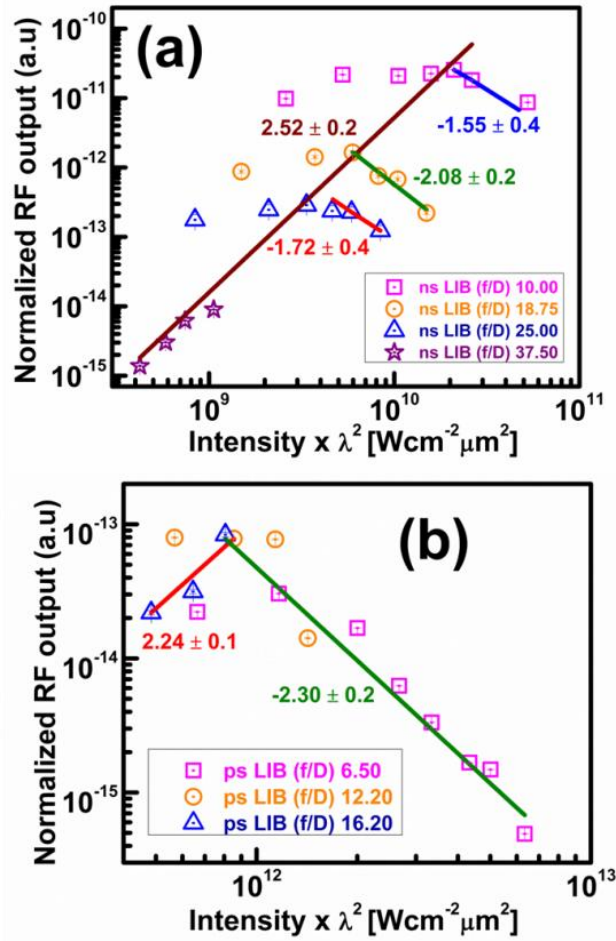


Fig 3.13. $I\lambda^2$ vs normalized RF output from (a) 7 ns and (b) 30 ps LIB of air at different focusing geometries under same laser and antenna polarization conditions.

Under all the focusing conditions, the RF emissions were observed to be significant up to certain input laser intensities beyond which it was observed to fall. The RF emissions from ns LIB, under all the focusing geometries, were observed to linearly increase with slope $\sim 2.52 \pm 0.2$ before attaining maximum at $I\lambda^2$ of $\sim 2.5 \times 10^{10} \text{ Wcm}^{-2} \mu\text{m}^2$. The fall in RF emissions under f/D 10, 18.75 and 25 were with slopes 1.55 ± 0.4 , 2.08 ± 0.2 and 1.72 ± 0.4 respectively. At f/D – 37.50 geometry, no such fall in the RF output was observed with the input laser energy used in our studies. The RF emissions from ps LIB were observed to be increasing with a slope of 2.24 ± 0.1 before falling with a slope of 2.30 ± 0.2 beyond the intensity $\sim 9 \times 10^{11} \text{ Wcm}^{-2} \mu\text{m}^2$. The maximum attainable value of $I\lambda^2 \sim 8 \times 10^{11} \text{ Wcm}^{-2} \mu\text{m}^2$ in ps LIB, under the f/D 16.20 was too low to observe the fall in RF emissions. Thus, the rising portions of the RF emissions from the ns LIB with slope 2.52 ± 0.2 and ps LIB with slope 2.24 ± 0.1 can be accounted for the

Chapter 3: RF emissions from LIB of atmospheric air

increase in the induced dipole moment (p) with the input laser intensity. This is analogous to the scaling laws associated with the evolution of hot electron temperature [131] and laser ablative pressures with the input laser intensity [132]. Also, the slopes of the falling portions in case of ns LIB (1.55 ± 0.4 , 2.08 ± 0.2 and 1.72 ± 0.4) and ps LIB (2.30 ± 0.2) explain the damping of plasma radiation [117, 123] that takes place at high input laser intensities due to recombination of the plasma constituents at a faster rate. The optimum value of $I\lambda^2$, under which the RF emissions are maximum, was found to be $\sim 2.5 \times 10^{10} \text{ Wcm}^{-2}\mu\text{m}^2$ and $9 \times 10^{11} \text{ Wcm}^{-2}\mu\text{m}^2$ in the ns and ps regimes, respectively.

In summary, the RF radiation emitted by the ns and ps LIB of atmospheric air was presented in this chapter. The interaction of charged species with the cluster of atoms and molecules results in the emission of RF radiation over selected spectral regions. Hence, the emissions are from a system which is very far from the completely ionized plasma state. The high peak power of ps laser ensures more ionization reducing the probability of interaction between the charged particles and neutrals. Thus for all the target materials, the RF emissions with 7 ns laser are observed to be higher than those with 30 ps laser. Besides, the signal strength of the emitted radiation was observed to be relatively higher when the polarization of the input laser and the antenna are same. Thus the emitted radiation shows specific polarization property associated with the input laser pulses. The spectral signatures from both ns and ps LIB were observed to be slightly varying, with focusing geometry, with the dominant emissions intact. The strength of the emissions from ns and ps LIB were observed to be decreasing and increasing respectively while traversing from tight to loose focusing conditions. Thus, the focusing conditions are found to play an important role in the generation of seed electrons and the subsequent RF emissions. The observed RF emissions are observed to match with the ion plasma frequency (ω_{pi}) confirming the role of neutral atoms and molecules in the emissions. The optimum laser intensity ($I\lambda^2$), under which the RF emissions are maximum, can be tuned by the right choice of focal geometry under which the laser pulses are focused. Analogous to the scaling laws describing laser-matter interactions, the RF emissions scale with respect to $I\lambda^2$. The slopes of the rising and falling portions of RF emissions with $I\lambda^2$, under different focal geometries, indicate the buildup of induced dipole moments and the

Chapter 3: RF emissions from LIB of atmospheric air

damping of plasma due to collisions/recombination respectively. This optimal window of $I\lambda^2$ (10^{10} - 10^{11} $\text{Wcm}^{-2}\mu\text{m}^2$), which gives rise to RF emissions of relatively higher strength, can be generated by choosing the focusing geometry of the input laser pulses.

Chapter IV

Radio emissions from laser induced breakdown of solid targets

This chapter contains the results of the studies carried out on the observation and characteristics of RF emissions from ns and ps LIB of solid targets.

To understand the significance of the target material in the plasma formation and the associated RF emissions from LIB, three different classes of target materials; conductors (copper, aluminum, SS304 and brass), insulators (alumina, Teflon, PVC and naphthalene) and dielectrics (borosilicate glass, Mica, BaTiO₃, ZrSnTiO₄ and LiNbO₃) were chosen. The laser-matter interaction that leads to different values of plasma density (n_e) for different materials, determines the charge-neutral interactions and the subsequent emissions. The emitted frequencies were observed to match with the estimated ion-plasma frequency (ω_{pi}) values, confirming the role of ions in the RF emissions. At very low input laser energies, the materials of same electrical properties were observed to be grouped with respect to the RF emissions. The amplitude of conducting samples was observed to be relatively higher than the other classes. This is because of the relatively lower ionization potential of metallic samples which, during laser-matter interaction, yield sufficient electrons that contribute to the plasma. As in the case of atmospheric air, the emissions from solids at high input laser energies were observed to be falling down due to the faster plasma recombination rate. In case of ps LIB, the ratio of plasma frequency (ω_p) to the laser frequency (ω_L) was observed to be approaching unity. Hence, at high input energies, the laser-plasma interaction is considerably reduced which brings down the RF emissions.

Chapter 4: RF emissions from LIB of solid targets

In the previous chapter, the interaction of laser with atmospheric air and its subsequent effects on the emission of low frequency radiation and their characteristics were presented. In this chapter, similar studies with the solid targets are presented. The local heating, due to the laser electric field, gives rise to more seed electrons for breakdown in case of solid targets [1-6]. Hence, the laser breakdown threshold for solids is lesser than that of gases. Also, the electron density (n_e) and thus, the plasma frequency (ω_p) are much higher for solid targets compared with gas targets [14]. According to the Maxwell's equations, the variation of the electric field of the electromagnetic beam contains electrical conductivity (σ) term which is given in equation 4.1[133].

$$\nabla^2 E = \sigma\mu \frac{\partial E}{\partial t} + \epsilon\mu \frac{\partial^2 E}{\partial t^2} \quad (4.1)$$

Thus, the propagating electromagnetic wave is influenced by the electrical conductivity of the medium. Hence, the laser-matter interaction with targets of different ' σ ' will be different. Because of the availability of pool of free electrons in metals [134], the amount of heating, due to the laser field, that takes place in conducting samples is much higher than that in case of insulating and dielectric samples [135]. Therefore, the aim was to study the RF emissions from samples of different classes of electrical conductivity. In the class of conductors, targets made of single atom (aluminum and copper) and alloys (SS304 and Brass) were opted for the experiments. Aluminum, copper and SS304 were chosen as they have been used in the standardization of many LIBS based experiments. The other alloy, brass, is chosen so that the emissions from brass, whose major component is copper, can be compared to that from copper. Besides insulators (alumina, teflon, PVC and naphthalene) and dielectrics (borosilicate glass, mica, BaTiO₃, ZrSnTiO₄ and LiNbO₃) were chosen as targets. Most of the target materials were commercially procured whereas the ceramic samples were compacted and sintered (to their maximum packing densities) in the laboratory. The 7 ns and 30 ps pulses were focused with the same lens in the focal geometry (f/D) ~ 10 and 6.5 ns and ps regimes respectively. Single shot-LIB was ensured with the target materials mounted on an electronically controlled XY translation stages (M-443, LTA-HA, and ESP-300, M/s. Newport). The laser beam was focused on the target material

ensuring that no air breakdown was happening. An average of RF spectra over 100 laser shots was considered for analysis.

4.1 Effect of antenna polarization

The RF spectra from ns and ps LIB of metal targets with different antenna polarization are shown in Fig 4.1. With both ns and ps LIB, the emitted frequencies were observed to vary with antenna polarization. With ns pulses, the lines with V-pol antenna were strong and well resolved (Fig 4.1a and 4.1b), whereas with ps pulses, the frequency lines with H-pol antenna were observed to be dominant and better resolved (Fig 4.1c and 4.1d). Hence in solids, as in the case of air, the signal reception was observed to be better when the laser and antenna polarization are same [117, 123]. Thus, the analyses were emphasized with similar laser and antenna polarization conditions.

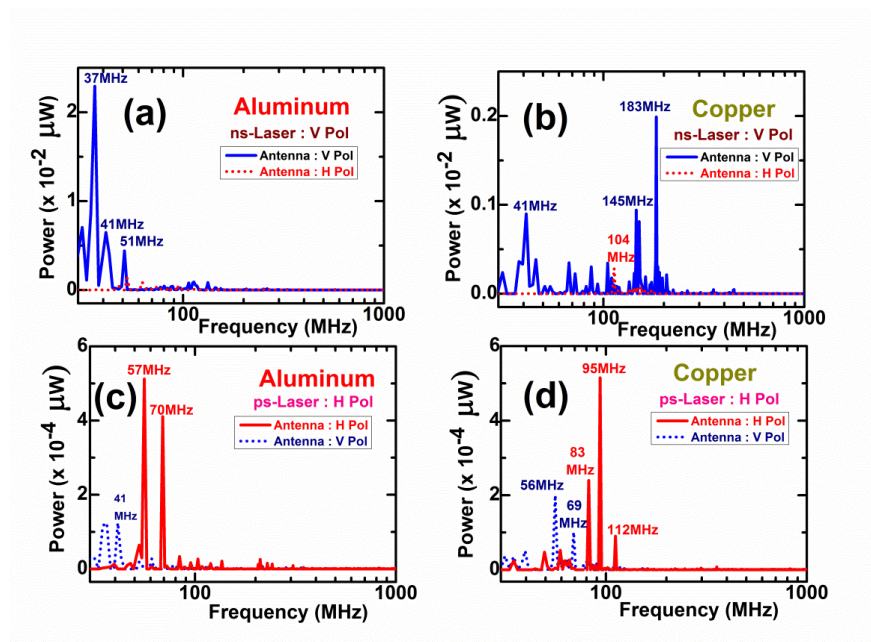


Fig 4.1: RF emissions with different antenna polarization from (a) Aluminum (b) Copper from 7 ns LIB at 5 mJ and (c) aluminum (d) copper from 30 ps LIB at 5 mJ.

4.2 Data analysis

4.2.1. RF emissions from LIB of conductors

The input laser energy dependent RF emissions from the ns and ps LIB of conducting samples are given in Fig 4.2 and Fig 4.3 respectively.

Chapter 4: RF emissions from LIB of solid targets

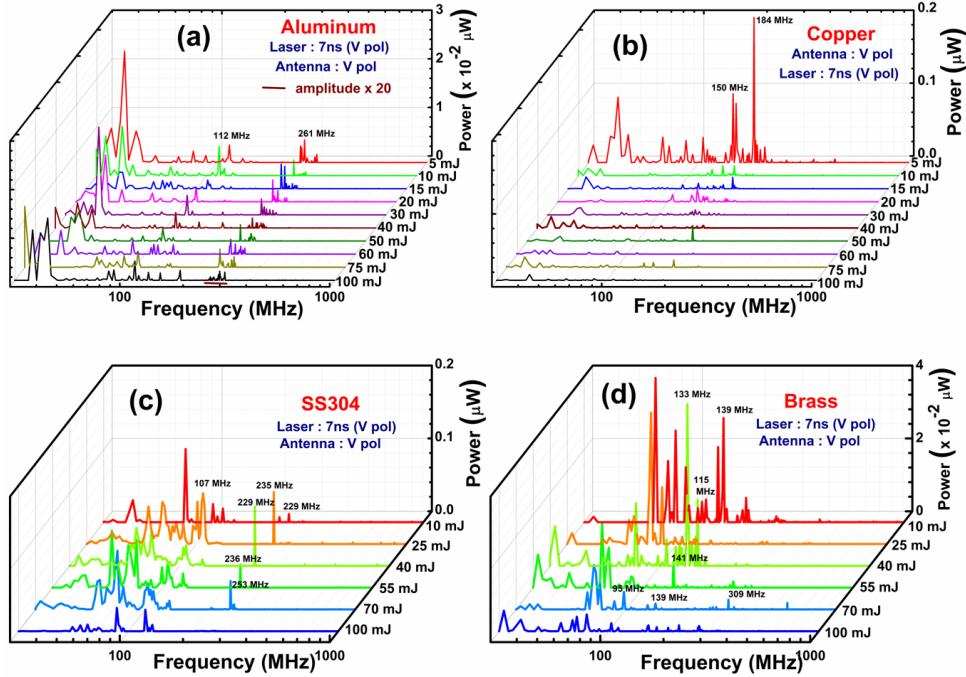


Fig 4.2: RF emissions from 7 ns LIB of conductors with same laser and antenna polarization. 250-270 MHz is amplified in 4.2 (a) by 20 to view the frequencies better.

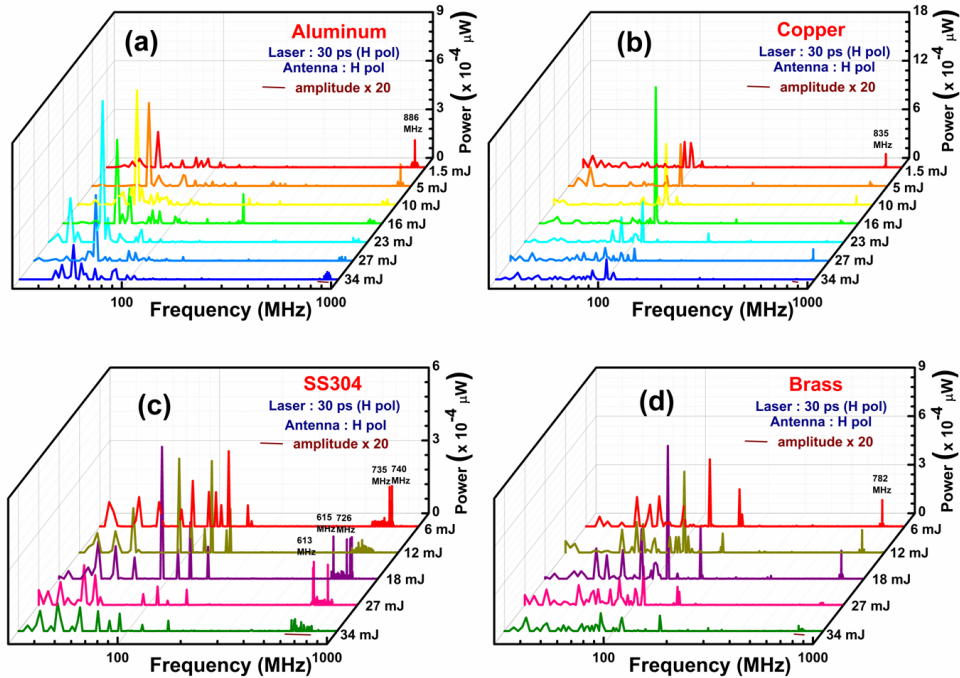


Fig 4.3: RF emissions from 30 ps LIB of conductors with same laser and antenna polarization. 850-900 MHz, 820-840 MHz, 600-760 MHz and 760-800 MHz are amplified in 4.6 (a), 4.6 (b), 4.6 (c) and 4.6 (d) respectively, by 20 to view the frequencies better.

Chapter 4: RF emissions from LIB of solid targets

The RF spectra from ns and ps LIB of the conducting samples were observed to fall in different and distinguished spectral bands. The dominant emissions from the ns LIB of copper and aluminum were observed to fall in 136 MHz and 35 MHz respectively. The relatively high frequency emissions (above 200 MHz) were observed from ns LIB of SS304. These show the significance of the target material in the RF emissions from LIB. Common RF bands were observed for materials that contain similar elemental identities. For example, the peaks over 70-200 MHz in ns LIB and 50-70 MHz in ps LIB are found common for both copper and brass, whose major constituent is copper. However, the bands above 150 MHz were observed from the ps LIB of brass, but not from that of copper. Fig 4.4 gives the emissions from conducting targets, under similar experimental conditions. The detailed tabulation of RF peaks from the ns and ps LIB of all the materials studied, under different antenna polarization, is provided in table 4.1.

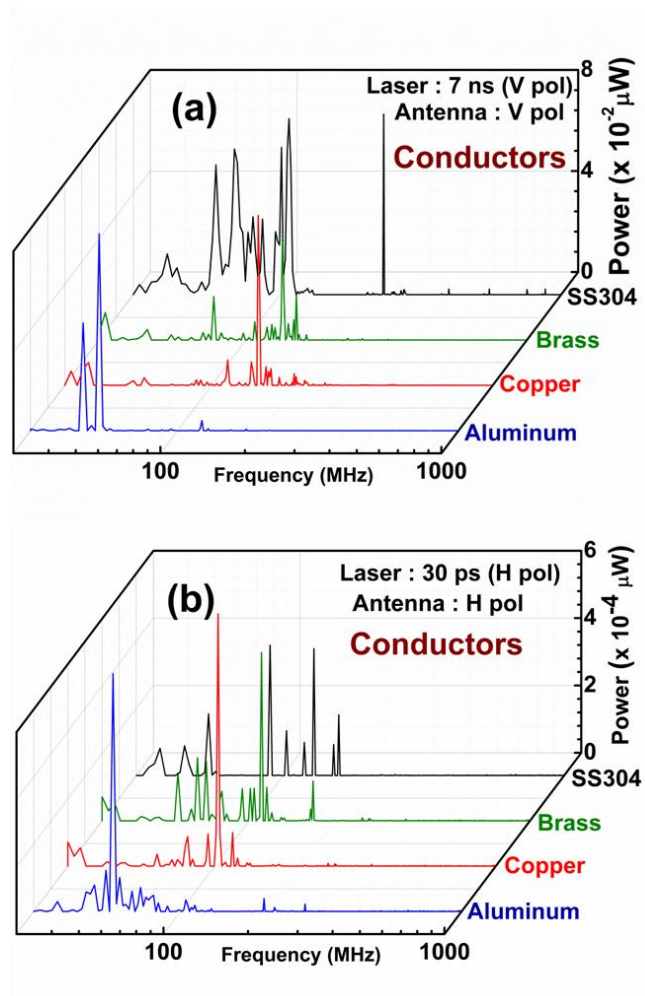


Fig 4.4: RF emissions from (a) 7 ns LIB at 25 mJ and (b) 30 ps LIB at 12 mJ of conductors

Chapter 4: RF emissions from LIB of solid targets

Table 4.1: Bands of RF emissions from LIB of conductors with different antenna polarization

Target Material	Material density 'ρ' (g/cc)	Electrical conductivity 'σ' (S/m)	ns LIB		ps LIB	
			V pol antenna bands (MHz)	H pol antenna bands (MHz)	V pol antenna bands (MHz)	H pol antenna bands (MHz)
Copper	8.96	5.96×10^7	70-200	100-200	40-70	80-120
Aluminum	2.70	3.50×10^7	30-60, 260-270	40-100	30-50	50-70
Brass (Cu, Zn etc.,)	8.56	1.67×10^7	70-310	60-200	50-70, 150-155	50-70, 80-130, 160-165
SS304 (Fe, Cr, etc.,)	7.92	1.45×10^6	80-130, 220-255	80-130, 190-220	40-60, 150-155	40-60, 80-120, 150-155

4.2.2. RF emissions from LIB of insulators

The input laser energy dependent RF emissions from the ns and ps LIB of insulators are given in Fig 4.5 and 4.6 respectively. The comparison of the RF emissions from different insulators is given in Fig 4.7.

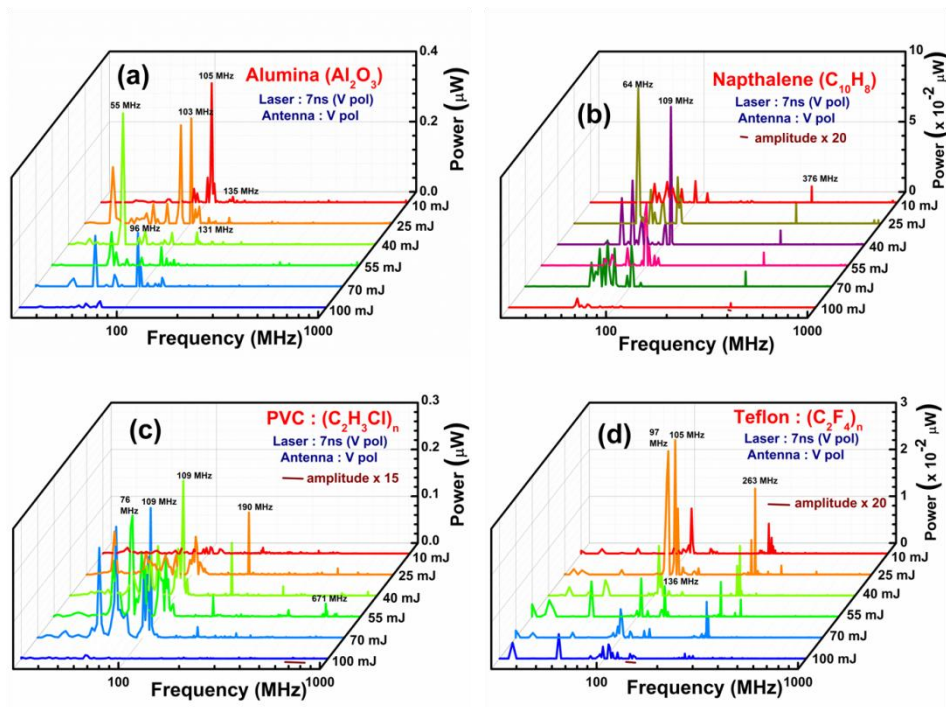


Fig 4.5: RF emissions from 7 ns LIB of insulators with same laser and antenna polarization. 370-380 MHz, 650-850 MHz and 130-140 MHz are amplified in 4.5 (b), 4.5 (c) and 4.5 (d) respectively, by 20 to view the frequencies better.

Chapter 4: RF emissions from LIB of solid targets

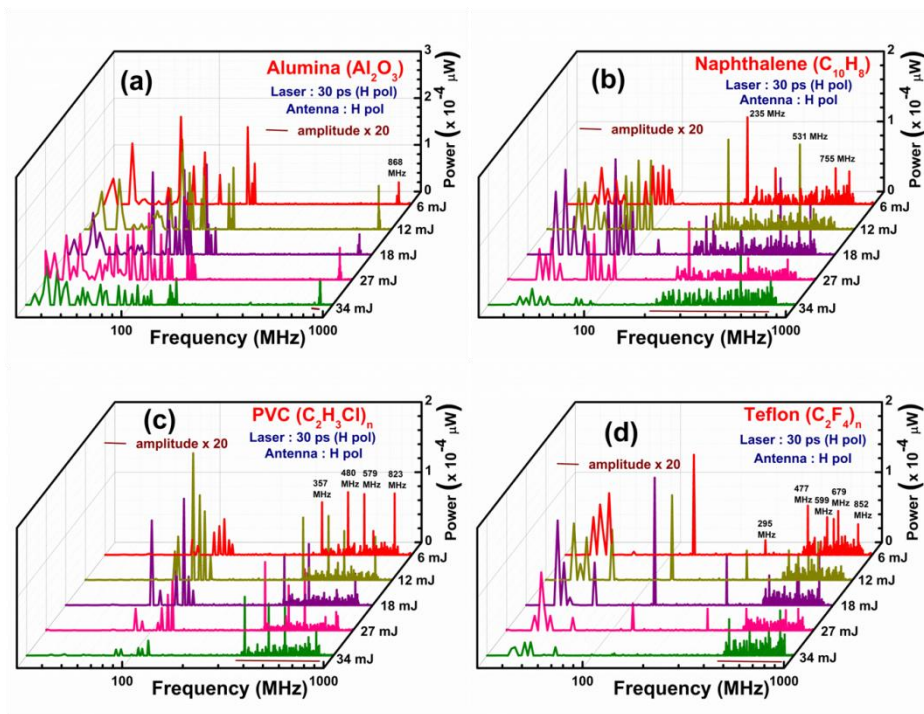


Fig 4.6: RF emissions from 30 ps LIB of insulators with same laser and antenna polarization. 850-870 MHz, 200-800 MHz, 350-850 MHz and 450-900 MHz are amplified in 4.6 (a), 4.6 (b), 4.6 (c) and 4.6 (d) respectively, by 20 to view the frequencies better.

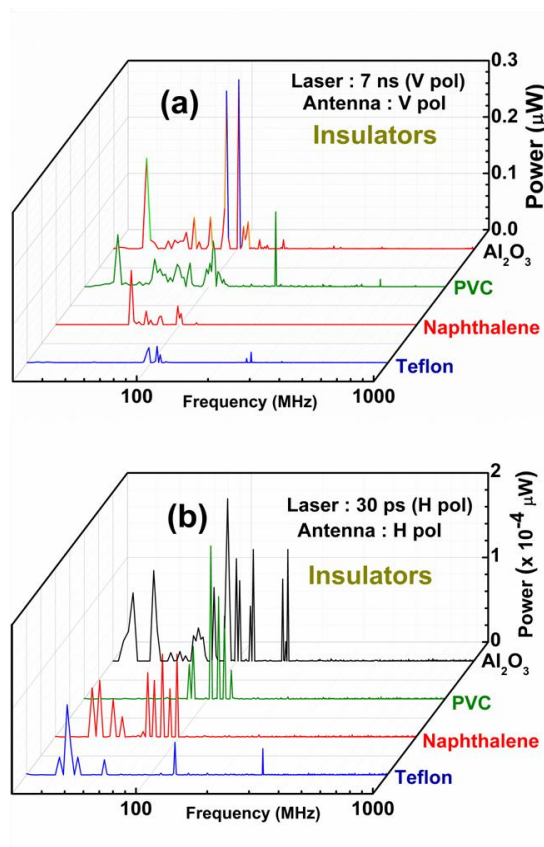


Fig 4.7: RF emissions from (a) 7 ns LIB at 25 mJ and (b) 30 ps LIB at 12 mJ of insulators

Chapter 4: RF emissions from LIB of solid targets

The RF spectra from ns and ps LIB of the insulators were observed to have several RF bands specific to the material interacting with laser. Some overlaps in the bands below 120 MHz from ns and ps LIB of different targets were observed. However, bands of considerable strength beyond 250 MHz were observed only from the ns and ps LIB of teflon. Also, ns LIB of PVC at V-pol antenna is observed to emit radiation around 190 MHz which is not seen with other materials. In case of insulators, the bands from ps LIB appear to be sharper and spread over than those from ns LIB, indicating the role of input laser intensity in the plasma formation and the RF emissions from the LIB of insulators. Table 4.2 gives the details of the bands from ns and ps LIB of insulators.

Table 4.2: Bands of RF emissions from LIB of insulators with different antenna polarization

Target Material	Material density 'ρ' (g/cc)	Electrical conductivity 'σ' (S/m)	ns LIB		ps LIB	
			V pol antenna bands (MHz)	H pol antenna bands (MHz)	V pol antenna bands (MHz)	H pol antenna bands (MHz)
Alumina (Al ₂ O ₃)	3.95	10 ⁻¹⁵	50-60, 100-135	70-130	50-70, 140-150	40-45, 150-170, 860-870
Naphthalene (C ₁₀ H ₈)	1.14	10 ⁻¹⁶	50-80, 110-115, 370-380	80-100	80-100	40-60, 70-100, 230-240, 531-535, 750-758
PVC (C ₂ H ₃ Cl) _n	1.38	10 ⁻¹⁴	50-110, 180-190, 665-675	70-110	50-70, 110-130	80-85, 110-130, 355-825
Teflon (C ₂ F ₄) _n	2.20	10 ⁻²⁴	90-120, 250-280	110-120, 280-290	50-55, 150-170, 250-255	40-50, 62-67, 128-132, 292-298, 475-860

4.2.3. RF emissions from LIB of dielectrics

The input laser energy dependent RF emissions from the ns and ps LIB of dielectric targets are given in Fig 4.8 and 4.9 respectively. The RF spectra from ns and ps LIB of the dielectrics were observed to have spectral bands that are unique with respect to each material of its class. The comparison of the RF emissions from different dielectrics is given in Fig 4.10. Unlike conductors and insulators, the frequency emissions from dielectrics were observed to extend upto 400 MHz.

Chapter 4: RF emissions from LIB of solid targets

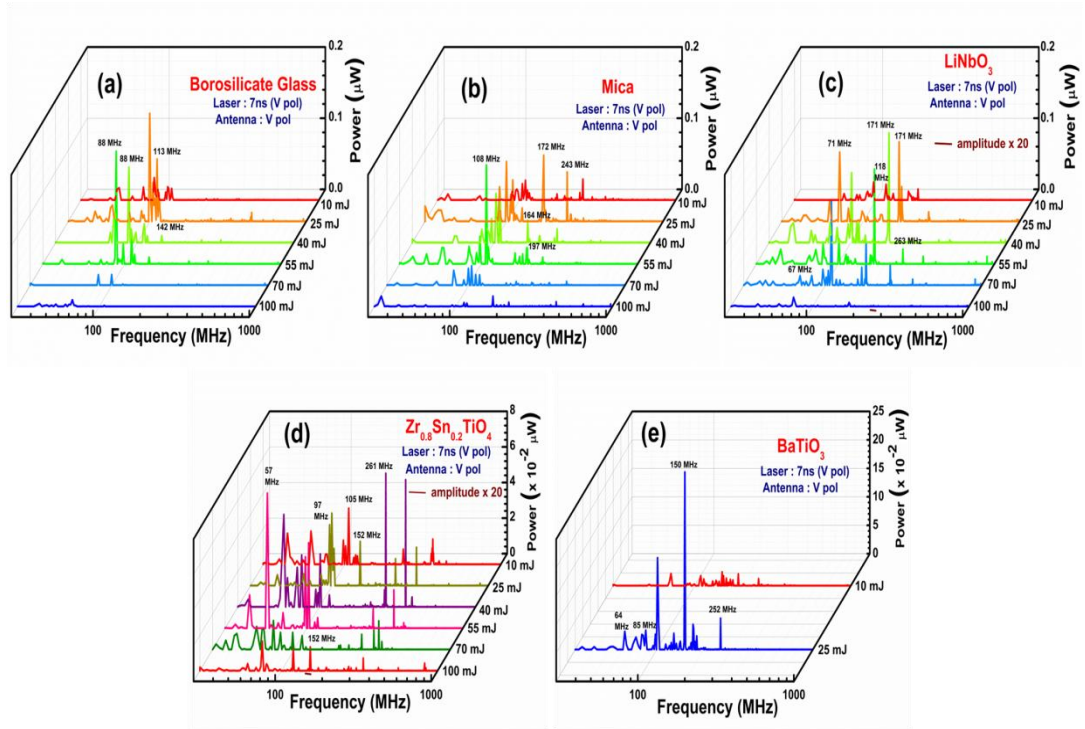


Fig 4.8: RF emissions from 7 ns LIB of dielectrics with same laser and antenna polarization. 255-265 MHz and 145- 155 MHz are amplified in 4.8 (c) and 4.8 (d) respectively, by 20 to view the frequencies better.

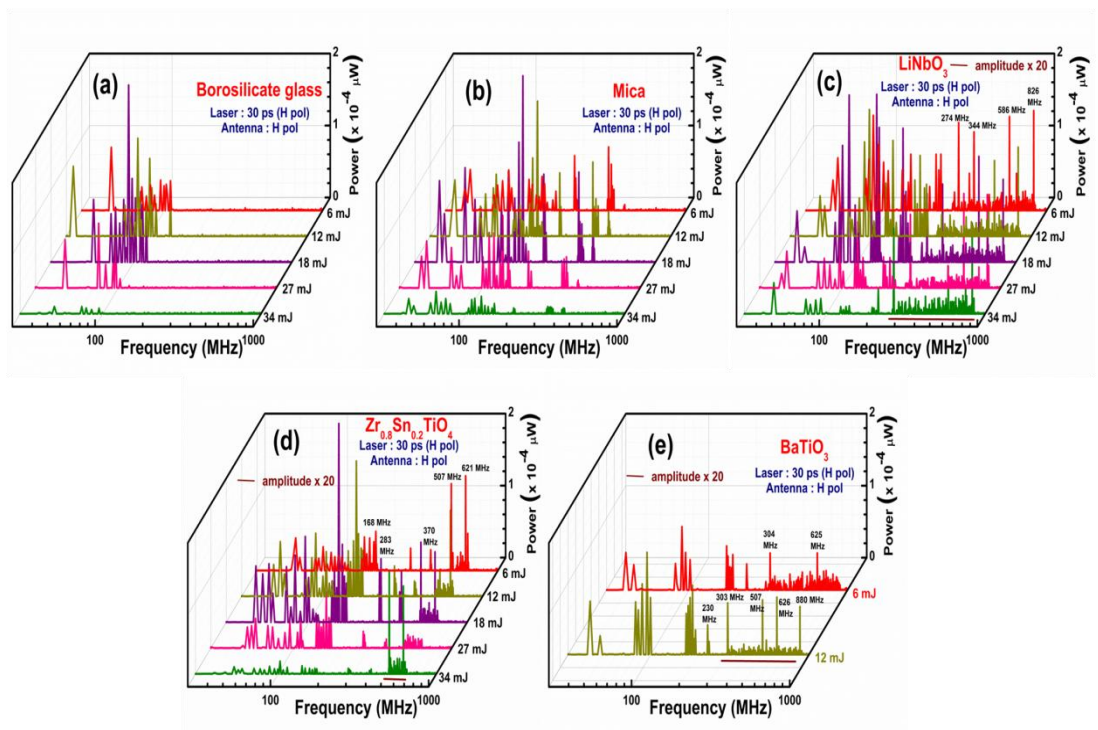


Fig 4.9: RF emissions from 30 ps LIB of dielectrics with same laser and antenna polarization. 250-900 MHz, 500-700 MHz and 300-900 MHz are amplified in 4.9 (c), 4.9 (d) and 4.9 (e) respectively, by 20 to view the frequencies better.

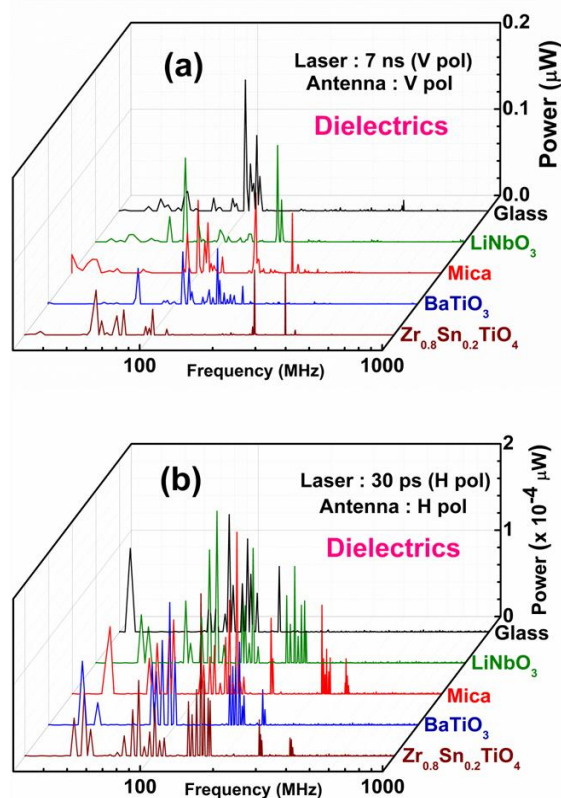


Fig 4.10: RF emissions from (a) 7 ns LIB at 25 mJ and (b) 30 ps LIB at 12 mJ of dielectrics

With ns LIB, the intensities of RF emissions from borosilicate glass, Mica and LiNbO_3 were observed to be similar. However, the intensity of RF emissions from the ns LIB of $\text{Zr}_{0.8}\text{Sn}_{0.2}\text{TiO}_4$ was observed to be an order less than that from the other compounds. For ps LIB, as the laser intensity is higher when compared to that of ns LIB, slightly high powered RF emissions over higher frequencies (> 200 MHz) were observed from the perovskite oxides (BaTiO_3 , ZrSnTiO_4 and LiNbO_3). When compared to the other dielectrics studied, the RF emission bands from borosilicate glass were observed to be narrower, both in case of ns (80-120 MHz) and ps LIB (70-110 MHz) of borosilicate glass. Within the dielectrics, the compounds that contain elements of lower atomic (Z) and mass (A) numbers (Borosilicate glass and Mica) and the compounds that have high Z and A values (BaTiO_3 , ZrSnTiO_4 and LiNbO_3) have shown interesting RF emissions with intensity. In one of the studies, ablation pressure (P) is proportional to $(A/2Z)^{1/3}$ where, A and Z are the mass and atomic numbers respectively [131]. Hence ‘P’ should be higher for elements of higher Z. In another study on the scaling of X-ray intensity with the input laser intensity, the plasma properties were observed to be

Chapter 4: RF emissions from LIB of solid targets

dependent on Z [136]. Hence, the emission of higher frequencies from the perovskite oxides can be attributed to the influence of the atoms of higher Z. The atomic numbers of Zr (40), Nb (41), Sn (50), Cs (55), Ba (56) in the dielectrics are much higher than those in the borosilicate glass, conductors and insulators. The RF emissions from the LIB of the perovskite oxides were observed to be similar, barring few variations. Table 4.3 gives the details of the bands from ns and ps LIB of dielectrics.

Table 4.3: Bands of RF emissions from LIB of dielectrics with different antenna polarization

Target Material	Material density 'ρ' (g/cc)	Electrical conductivity 'σ' (S/m)	ns LIB		ps LIB	
			V pol antenna bands (MHz)	H pol antenna bands (MHz)	V pol antenna bands (MHz)	H pol antenna bands (MHz)
Glass (Borosilicate)	2.203	10^{-13}	80-120, 140-145	70-120	60-90	70-110
Mica (K, Na, Ba, Cs, Al, Zn, Si, Ti, Li, Mg etc.,)	1.9	10^{-15}	80-130, 160-170, 240-260	60-80, 120-135, 150-170, 230-250	50-70, 90-140, 200-205, 310-315	40-45, 60-80, 100-150, 195-200, 280-285, 320-325, 400-410
Lithium Niobate (LiNbO ₃)	4.63	10^{-12}	100-130, 160-180, 260-265	110-130, 160-170	40-60, 100-130, 170-180	40-45, 70-100, 120-140, 180-220, 270-830
Barium Titanate (BaTiO ₃)	4.49	10^{-9}	70-200, 250-260	70-200, 250-260	40-45, 80-85, 120-160	38-42, 80-100, 170-190, 230-233, 300-880
Zirconium Tin Titanate (Zr _{0.8} Sn _{0.2} TiO ₄)	4.33	10^{-6}	60-155, 250-270, 320-350	60-120, 190-200	50-80, 120-145, 240-260	50-53, 70-110, 140-170, 280-285, 370-625

4.3 Discussion

The RF emissions from LIB were observed to be material specific meaning that the interaction of laser with every material is unique. This is because of the specific outermost electronic configuration and the associated properties, bonding etc. of a particular material. The laser radiation can interact only with the electrons of the atoms of the material, as the heavier nuclei cannot follow the high frequencies of the visible radiation. Also, the core electrons usually have very

Chapter 4: RF emissions from LIB of solid targets

high binding energies and so, the laser can strongly interact only with the loosely bound electrons [137]. Therefore, besides the laser parameters, the plasma number density (n_e , n_i) depends on the properties of the target material. This degree of ionization, which depend upon the input laser parameters and the target properties, decide the RF emissions. Considering that the targets under laser irradiation are singly ionized, the ion plasma frequencies (ω_{pi}) in case of ns LIB and ps LIB, were estimated using equation 3.1 as in chapter 3. The electron density (n_e) values for some of the samples are estimated from LIBS experiments while that for the rest of the samples were obtained from the literature [14, 138-144], under similar intensity conditions. Table 4.4 and 4.5 gives the estimated values of ion plasma frequencies in case of ns and ps LIB of the studied targets respectively.

Table 4.4: Estimated ion plasma frequencies (ω_{pi}): ns LIB of targets

Target	Laser intensity range (W/cm ²)	Electron density (n_e) range (cm ⁻³)	Estimated ion plasma frequency values (MHz)	
			Atomic species	Molecular species
Conductors	$3 \times 10^{10} - 7 \times 10^{10}$	$1 \times 10^{17} - 3 \times 10^{17}$	Cu ⁺ : 141,185 Al ⁺ : 260 Fe ⁺ : 235 Cr ⁺ : 243 Ni ⁺ : 229 Mn ⁺ : 236 C ⁺ : 325 Zn ⁺ : 139	(Fe ₂ O ₃) ⁺ : 110 (CuO ₂) ⁺ : 94, 150 (Mn ₃ O ₄) ⁺ : 110 (CuO) ⁺ : 131
Insulators	$1 \times 10^{10} - 8 \times 10^{10}$	$1 \times 10^{16} - 4 \times 10^{16}$	Al ⁺ : 103 O ⁺ : 133 C ⁺ : 107, 133, 190 H ⁺ : 376, 671 Cl ⁺ : 110 F ⁺ : 105	(Al ₂ O ₃) ⁺ : 53 (C ₁₀ H ₈) ⁺ : 39 (C ₂ H ₃ Cl) ⁺ : 83 (C ₂ F ₄) ⁺ : 46 (C ₂) ⁺ : 75, 94, 134 (H ₂) ⁺ : 258, 460 (O ₂) ⁺ : 95 (F ₂) ⁺ : 75
Dielectrics	$9 \times 10^9 - 6 \times 10^{10}$	$2 \times 10^{16} - 9 \times 10^{16}$	B ⁺ : 140 Si ⁺ : 87, 171 O ⁺ : 115, 171, 242, 254, 263 Al ⁺ : 164 K ⁺ : 108 Na ⁺ : 188 Mg ⁺ : 184 F ⁺ : 197 Li ⁺ : 261 Nb ⁺ : 71 Ba ⁺ : 87 Ti ⁺ : 146, 151 Zr ⁺ : 106 Sn ⁺ : 95	(BaTiO ₃) ⁺ : 66 (LiNbO ₄) ⁺ : 64 (ZrSnTiO ₃) ⁺ : 60 (O ₂) ⁺ : 121, 180, 185

Chapter 4: RF emissions from LIB of solid targets

Table 4.5: Estimated ion plasma frequencies (ω_{pi}): ps LIB of targets

Target	Laser intensity range (W/cm ²)	Electron density (n_e) range (cm ⁻³)	Estimated ion plasma frequency range (MHz)	
			Atomic species	Molecular species
Conductors	$1 \times 10^{12} - 4 \times 10^{12}$	$7 \times 10^{18} - 1 \times 10^{19}$	Cu ⁺ : 1169, 1250 Al ⁺ : 2150 Fe ⁺ : 1247 Cr ⁺ : 1292 Ni ⁺ : 1216 Mn ⁺ : 1257 C ⁺ : 2693 Zn ⁺ : 1153	(Fe ₃ O ₄) ⁺ : 612 (Fe ₂ O ₃) ⁺ : 737, 885 (Cu ₂ O) ⁺ : 779, 833 (Mn ₃ O ₄) ⁺ : 616 (Mn ₂ O ₃) ⁺ : 742 (Ni ₂ O ₃) ⁺ : 725
Insulators	$5 \times 10^{12} - 8 \times 10^{12}$	$6 \times 10^{17} - 6 \times 10^{18}$	Al ⁺ : 1689 O ⁺ : 2192 C ⁺ : 755, 821, 852 H ⁺ : 2894, 2662 Cl ⁺ : 836 F ⁺ : 677	(Al ₂ O ₃) ⁺ : 868 (C ₁₀ H ₈) ⁺ : 231 (C ₂ H ₃ Cl) ⁺ : 359 (C ₂ F ₄) ⁺ : 295 (C ₂) ⁺ : 533, 579, 601, (H ₂) ⁺ : 1826, 1985 (O ₂) ⁺ : 1551 (F ₂) ⁺ : 479
Dielectrics	$6 \times 10^{12} - 8 \times 10^{12}$	$9 \times 10^{17} - 1 \times 10^{18}$	O ⁺ : 826, 880 Li ⁺ : 1254 Nb ⁺ : 343 Ba ⁺ : 301 Ti ⁺ : 509 Zr ⁺ : 369 Sn ⁺ : 280	(BaTiO ₃) ⁺ : 231 (LiNbO ₄) ⁺ : 272 (ZrSnTiO ₃) ⁺ : 165 (O ₂) ⁺ : 584, 623

It is evident that the emitted radio frequencies, shown in figures 4.2-4.10, correspond to the estimated ion-plasma frequencies shown in tables 4.4 and 4.5. The estimated values are observed with ± 3 MHz frequency error, which is the minimum frequency that the spectrum analyzer can resolve. In case of conducting samples, the estimated ω_{pi} values in ps LIB were observed to be in GHz range which is beyond the detection range of the antenna. Some of the peaks in the MHz region can be accounted for the contributions from the oxides of the elements present in the system. The wide range of ω_{pi} values for a particular atomic and molecular species is due to the variations in the input laser intensity. Also, the plasma number density of LIB of a two or multi atomic system depends upon the pre ionized densities and thus the breakdown threshold of the individual atoms in the system (as per equation 3.4). Therefore, even under the same intensity conditions, the ω_{pi} values of an atomic or molecular species in two different compounds can be different. Therefore, besides laser parameters, the sample parameters also determine the RF emissions from LIB. The normalized RF emissions over the entire range of detection, from ns and ps LIB of all the

materials at very low input laser energy (10 mJ in ns LIB and 6 mJ in ps LIB), were plotted as a function of peak with maximum amplitude (Fig 4.11).

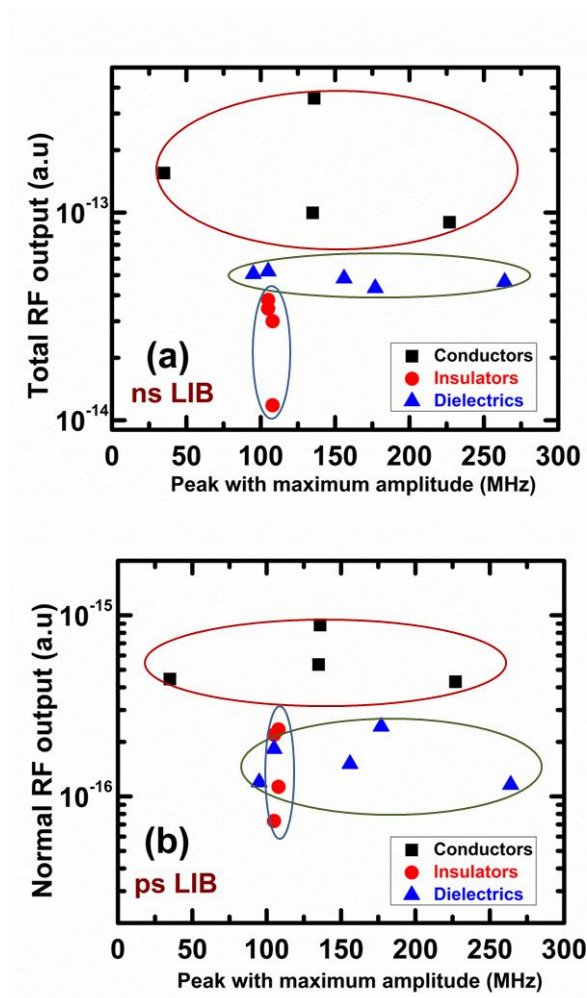


Fig 4.11: Normalized total RF output from (a) 7 ns LIB and (b) 30 ps LIB of the materials studied with same laser and antenna polarization

The materials of same class were observed to get grouped with respect to the RF emissions. The emissions from the conducting samples were observed to be higher than the non conducting samples by an order or two, at these laser energies, emphasizing the importance of electrical properties of the target material (as specified in the Maxwell's equations). As the ionization potential of the conducting samples is relatively lower [145] than the insulating and dielectric samples, the laser-matter interaction with metallic samples tends to give rise to sufficient electrons, even at very low input laser energies. Moreover, in the field of laser radiation, the electrons in the conduction band of the target, behave as free electrons. Therefore, under the influence of the laser field, the metallic samples that consist of plenty of conduction band electrons, contribute to the plasma [146].

Chapter 4: RF emissions from LIB of solid targets

Also, because of the availability of pool of free electrons, the amount of heating that takes place in conducting samples is much higher than that in case of insulating and dielectric samples [147]. Thus, the RF emissions from the conducting samples are shooting up at low input laser energies. However, at higher input laser energies, the number of neutrals in case of conductors becomes relatively lesser leading to lower RF emissions. Consequently, the separation between conductors and non conductors is not happening at higher input laser energies. The emission of RF radiation from LIB is observed to be dependent on the amount of input energy supplied in creating the plasma source. The variation in the normalized RF output from ns and ps LIB, as a function of input laser energy, is given in figure 4.12.

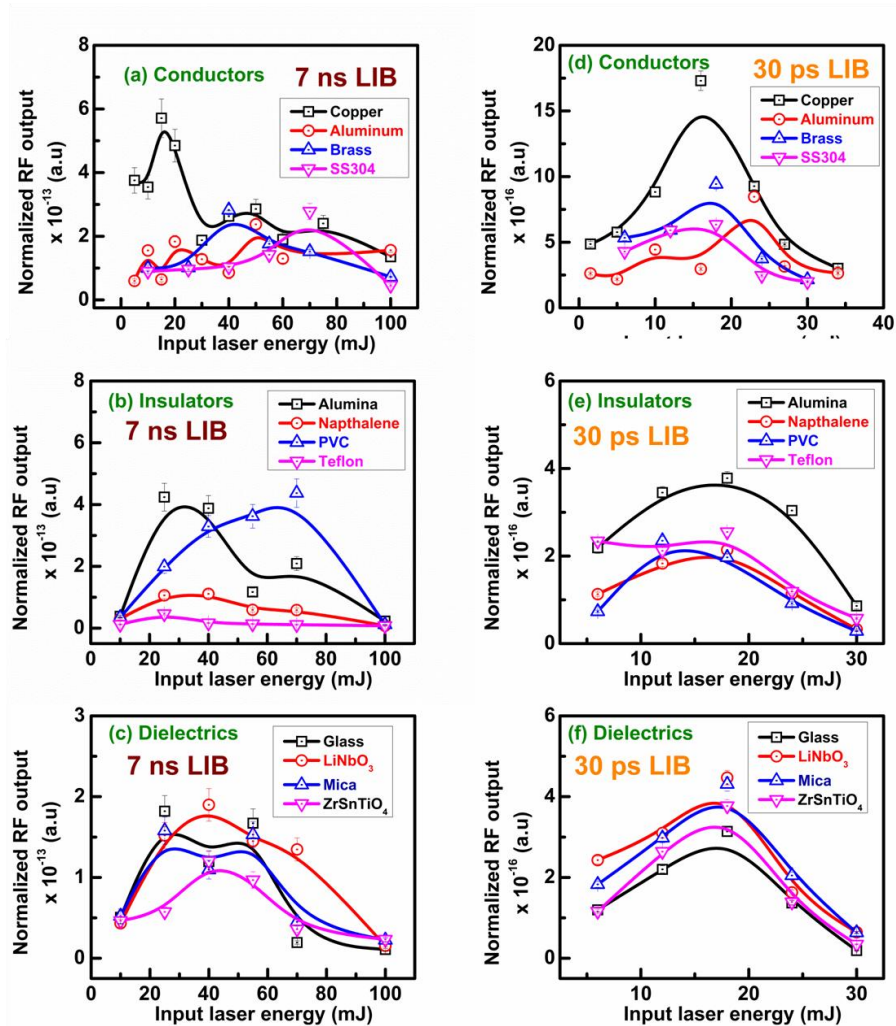


Fig 4. 12: Dependence of input laser energy on RF emissions from ns and ps LIB of the targets

Chapter 4: RF emissions from LIB of solid targets

Similar to that of atmospheric air, the total RF emissions, from ns and ps LIB of all the materials, were observed to be increasing upto certain input laser energies before coming down at high energies. This shows the effect of recombination of the plasma constituents at higher input laser energies. To further understand the effect of input laser energy, the values of ' ω_p ' from the ns and ps LIB of a few materials were calculated from the corresponding ' n_e ' values. To estimate the n_e values from the stark broadening [14] of the spectral lines in the visible region, LIBS data was collected from the 7 ns LIB of copper and aluminum. The n_e value of ns LIB of borosilicate glass was obtained from the literature [144]. Similarly, the typical values of n_e in case of ps LIB of aluminum and copper were obtained from the literature [138, 139]. The n_e and corresponding ω_p , from the LIB of the target materials in the ns and ps regimes are given in table 4.6.

Table 4.6: Values of n_e and ω_p in ns and ps LIB of targets

LIB	Input laser intensity (W/cm ²)	Plasma parameters	Aluminum	Copper	Borosilicate glass
ns LIB	$\sim 3.15 \times 10^{10}$	$n_e \times 10^{15} \text{ cm}^{-3}$	148	430	17
		$\omega_p \times 10^{12} \text{ Hz}$	21.7	37	1
		ω_p/ω_L	0.04	0.07	0.002
	$\sim 1.27 \times 10^{11}$	$n_e \times 10^{16} \text{ cm}^{-3}$	480	764	160
		$\omega_p \times 10^{13} \text{ Hz}$	12.4	15.6	7.14
		ω_p/ω_L	0.25	0.31	0.14
ps LIB	$\sim 10^{13}$	$n_e \times 10^{18} \text{ cm}^{-3}$	1000	100	-
		$\omega_p \times 10^{13} \text{ Hz}$	178.4	56.4	-
		ω_p/ω_L	3.57	1.13	-

Chapter 4: RF emissions from LIB of solid targets

In case of ns LIB, the ratio of ω_p and ω_L for copper and aluminum samples, at the input laser intensity $\sim 1.27 \times 10^{11} \text{ W/cm}^2$, are about 5-7 times than those the input laser intensity $\sim 3.15 \times 10^{10} \text{ W/cm}^2$. Hence, the recombination is proportionally high at higher input laser intensity. The n_e values in case of ns LIB of borosilicate glass were observed to be very low compared to that of the conducting samples. Due to this, the ratio of ω_p and ω_L for glass under these input conditions was observed to be very low when compared to that of copper and aluminum (Table 4.6). However, similar to the case of metallic samples, the RF emissions from ns LIB of borosilicate glass were observed to be coming down at higher laser intensities. [Fig 4.12c].

Also, An electromagnetic wave with frequency ' ω_L ' can penetrate into the plasma and interact with the medium of resonance frequency ' ω_p '. However, if ω_p is approaching ω_L , the reflectivity of the medium will be increasing [148]. When $\omega_p > \omega_L$, the electromagnetic wave cannot propagate into the plasma and it will be reflected back. The ratio of ω_p and ω_L ($5 \times 10^{14} \text{ Hz}$) is unity for the n_e value of about $2.76 \times 10^{19} \text{ cm}^{-3}$ where the plasma becomes opaque to the incident radiation. With the ps pulses, when the target materials were focused at intensity of the order of 10^{13} W/cm^2 , the electron densities were very high such that ratio ω_p/ω_L is several orders higher than that with ns pulses. In case of ps LIB of aluminum ($\omega_p/\omega_L = 3.57$) and copper ($\omega_p/\omega_L = 1.13$), the ratio is more than one which makes the plasma opaque to the incident radiation. Therefore, there is hardly any laser-plasma interaction at high input laser intensities in the ps LIB of target materials. Thus, with 30 ps pulses, the RF emissions drastically come down.

In summary, the RF emissions from solid targets were presented in this chapter. The laser-matter interaction that leads to different ' n_e ' values for different materials, determines the charge-neutral interactions and the subsequent RF emissions. The emitted frequencies were observed to be matching with the ion-plasma frequency ' ω_{pi} ' which confirms the role of ions in the RF emissions. Also, the electrical conductivity (σ) was observed to play an important role in the RF emissions from LIB. At very low input laser energies, the materials of same electrical properties were observed to be grouped with respect to the RF emissions with the amplitude of conducting samples relatively higher than the other classes.

Chapter 4: RF emissions from LIB of solid targets

This indicates the importance of the properties of the target material in the laser-matter interaction. The energy dependence of RF emissions from LIB of the materials show that the RF emissions of considerable strength can be obtained at lower input laser energies, as the charge-neutral interactions will be higher at relatively lower input laser energies. At higher input laser energies, the RF emissions from the LIB of all the materials were observed to fall due to the higher recombination plasma rates. In case of ps LIB of some targets, the emissions come down because of the plasma opacity for the incoming radiation. This is experimentally confirmed from the calculation of the ratio of ω_p and ω_L from the electron density values.

Chapter V

Radio emissions from laser induced breakdown of copper powder compacts

This chapter contains the results of the work carried out on the investigation of RF emissions from LIB of compacted copper micro powders.

Since the laser- matter interaction efficiency is reported to be improved with the surface modified targets, LIB of the targets made up of powders of different particle sizes and their contribution in the RF emissions were studied with four different grades of copper powders of different average particle sizes (2 μm , 15 μm , 40 μm and 420 μm) were used. The powders were compacted and heat treated, without allowing any grain growth, to vary the packing density besides improving the handling strength. For every powder grade, with a particular particle size, pellet with 60%, 70% and 80% of the theoretical density of copper was used as the target.

When compared with the bulk sintered sample, the emissions from the compacted micron powders were observed to be higher and lower at low and high input laser energies respectively. This is due to the difference in the surface properties of these samples. The compacted powders, due to their surface roughness, absorb most of the input laser radiation compared to the bulk sintered sample which, due to its highly polished surfaces, reflects away most of the incident input radiation. When the target (with a particular packing density) is composed of smaller particles, due to enhanced local field effect, the breakdown (under same experimental conditions) becomes relatively intense than those with targets (of same density) composed of larger particles.

5.1 Introduction

Tuning the input laser parameters [149] (as discussed in chapter 3) is a common way to tune the conditions that favour electromagnetic emissions, of desired frequency and characteristics, from the resulting plasma. Variation in the experimental environment such as changing the ambient gas [150] or working in vacuum [151] can also result in the enhancement of the emitted radiation. One of the most effective ways of increasing the efficiency of energy transfer from the laser to the sample is by modifying the surface of the target. It was reported that nano particles deposited on the surface of the target significantly lowers the breakdown threshold, owing to the enhanced electric field [152-160]. Also, it was studied that the microflakes and the impurities present on the target surface tend to bring down the breakdown threshold [156, 161] because of the local increase in the laser irradiance due to the size dependent properties of the particles present on the surface. The shock velocity of the laser induced shock waves were observed to be increasing with the number of periodic surface structures on the target, as the plasma trapping is proportional to the number of surface structures [162]. Another study reveals the enhancement in hard X-ray Bremsstrahlung emission due to the enhancement in the light coupling and hot electron production in case of grating targets [163].

Consider a target made up of smaller particles of radius 1 μm instead of a bulk target of radius 1 cm (Fig 5.1). The total surface area of the target made of smaller particles is 10,000 times higher than the bulk target. Based on the above results [152-163], the laser-matter interaction with such a target material should be result in the improved efficiency of energy transfer from the laser to the target material. According to studies of Leela et al, more and more plasma trapping should take place with targets made of finer particles, as the number of interparticle boundaries that fall within the laser spot diameter ($2\omega_0$) is analogous to the increased surface structures [162]. Therefore, to understand the effect of sample surface on the RF emissions from LIB, experiments with target materials packed with particles of different sizes were planned. The effect of enhancement of laser induced breakdown was observed with the deposition of metallic nano powders [156] and no evidence of enhancement was reported with non-metallic samples. From these, it is evident that the free electrons (due to the deposition of

metal coating) on the target play a major role in the enhancement of breakdown. Hence, the studies were planned with metal powders. Also, the impurities in the form of binder can be avoided with metallic powders because of their ease in the compaction due to the availability of more slip systems [134].

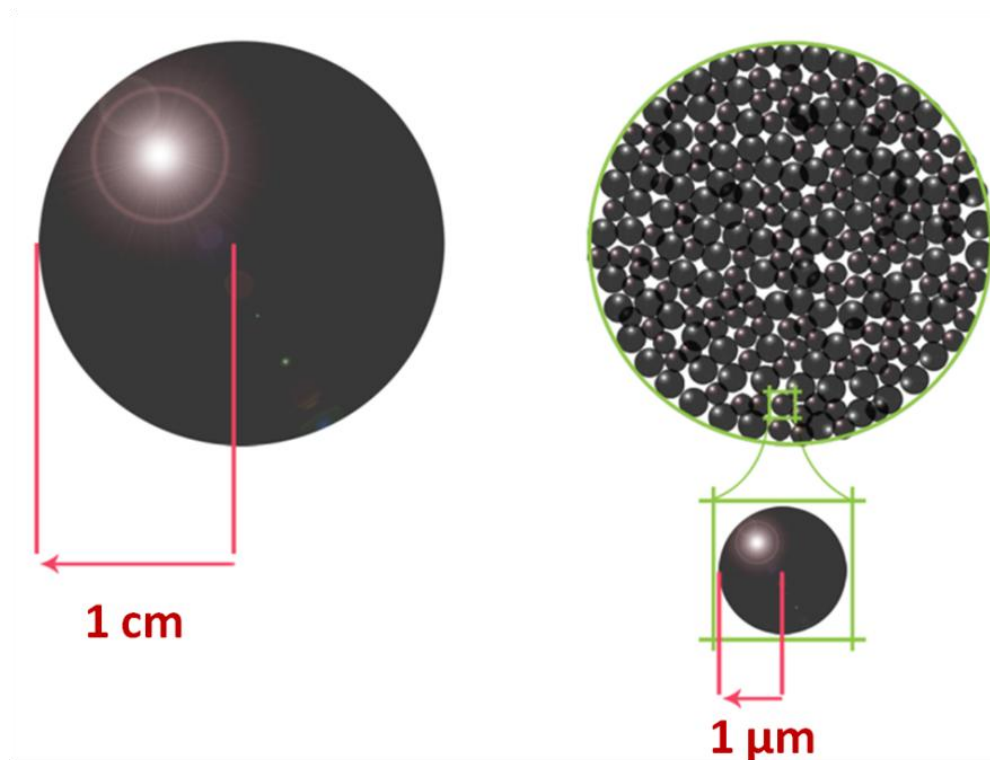


Fig 5.1: Illustration of target made of smaller particles

Therefore, for systematic studies and understanding of the effect of target surface on RF emissions from LIB, four grades of copper powders of different particle sizes (ranging 2-420 μm) were obtained from Sigma Aldrich. Before proceeding with the compaction of these powders, the images of the powder particles were scanned at different magnifications. The image analyses of these scanning electron microscope (SEM) images were utilized to arrive at the estimation of the particle size distribution and the average particle size of the powder grades. The SEM image and the corresponding size distribution of the as received copper powders of different grades are shown in Fig 5.2. It is observed that the distribution of the finer powders were narrower compared to those with the coarser ones.

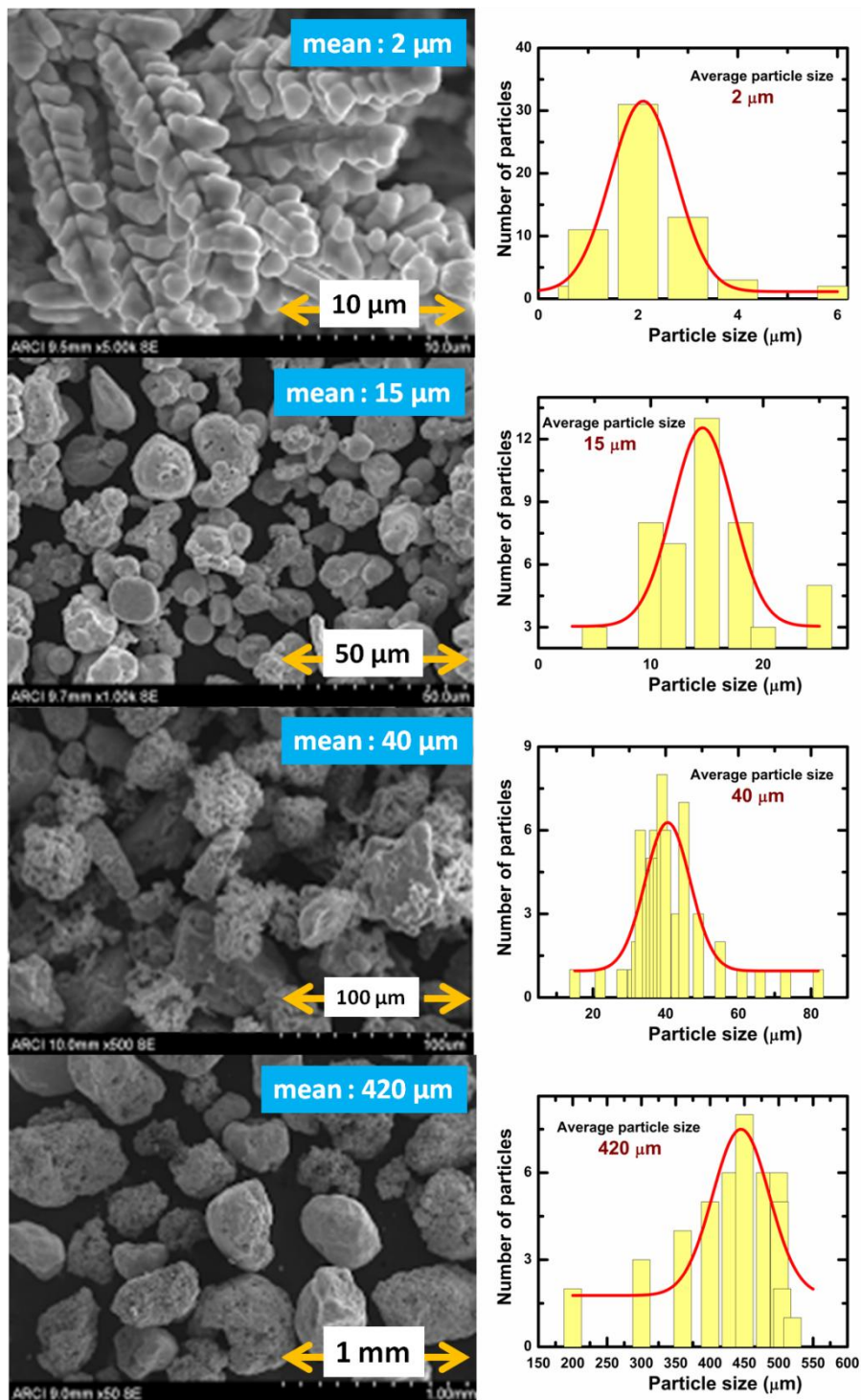


Fig 5.2: SEM images of the as received copper powders and their corresponding particle size distribution fits

5.2 Sample preparation

All the powders were pressed into many number of 3 cm square pellets by the application of pressure ranging 55-165 MPa. The compacted samples were of different packing densities, since compaction is a function of applied pressure

[164] as well as the particle size of the powders [165]. The handling strength of the pellets was observed to be too low to perform the laser based experiments. In a study, it was reported that the mechanical properties of copper pellets were increased without much change in the grain size by heating the pellets at temperature much lesser than the melting temperature (1085°C) at very high heating rates [166]. Based on this, three sets of the pressed samples were taken and each set was heated at different temperature (400°C, 500°C and 600°C) at a heating rate of 30°C/min. Once the samples attain the respective set temperatures, they were immediately transferred to the room temperature. With considerable improvement in the handling strength, the heat treated pellets were observed to have a wide range of packing density (measured by the Archimedes technique) based on the powder particle size, compaction pressure and heating temperature. The SEM images of the pellets pressed with maximum pressure and heat treated at 600°C are shown in Fig 5.3.

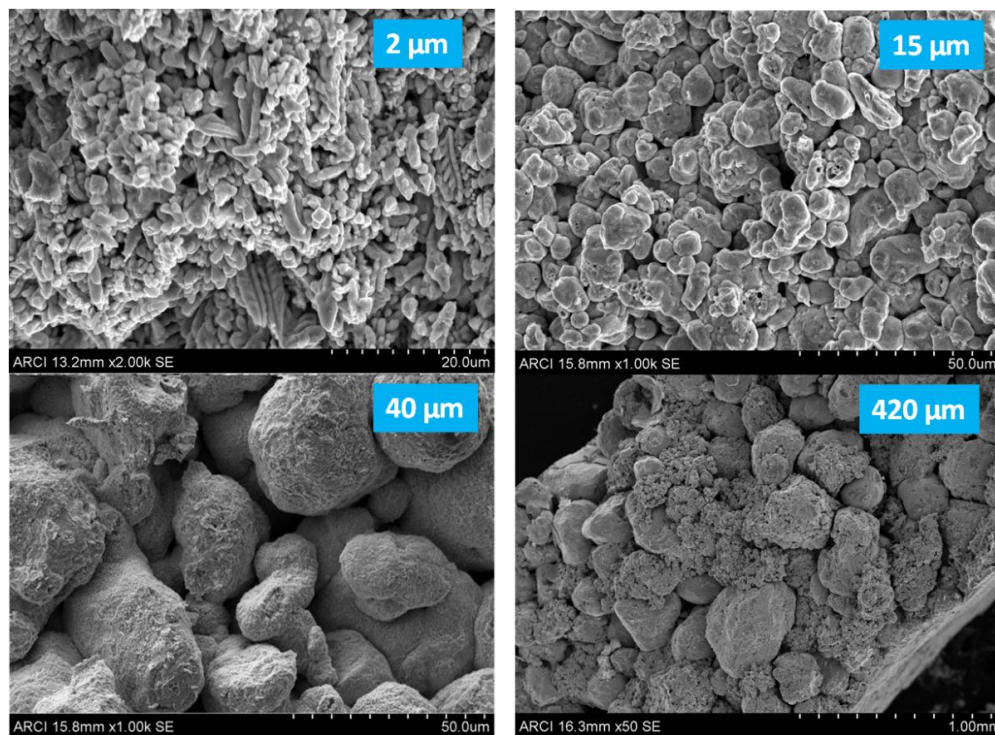


Fig 5.3: SEM images of the copper samples heat treated at 600°C

The SEM images of the heat treated samples show densely packed copper compacts. The images also reveal that there is no grain growth at 600 °C as reported by Zheng et al [166]. Hence, the heat treatment of the copper powder compacts has resulted in densification of the compacts without grain growth

thereby keeping the particle properties intact. For every powder grade, with a particular particle size, one pellet with 60%, 70% and 80% of the theoretical density of copper was chosen. The compaction pressures and the corresponding temperatures to achieve the desired density of the pellet of each powder grade are given in table 5.1. Hence, pellets with 4 different particle sizes and 3 different packing densities (12 samples), without losing the significance of particle properties were obtained for the laser-matter interaction studies.

Table 5.1: pressure and temperature used to prepare the compacts

Particle size (μm)	$(60 \pm 2) \%$ of theoretical density		$(70 \pm 2) \%$ of theoretical density		$(80 \pm 2) \%$ of theoretical density	
	Temperature ($^{\circ}\text{C}$)	Pressure (MPa)	Temperature ($^{\circ}\text{C}$)	Pressure (MPa)	Temperature ($^{\circ}\text{C}$)	Pressure (MPa)
2	500	55	500	165	600	165
15	400	165	500	110	600	110
40	400	110	500	55	600	55
420	400	55	400	165	500	165

5.3 Results and discussion

The laser pulses (532 nm) were focused (with lens of 80 mm focal length) in the focal geometry (f/D) 10 and 6.5 in case of ns and ps LIB respectively. Single shot-LIB was ensured with the target materials mounted on an electronically controlled XY translation stages (M-443, LTA-HA, and ESP-300, M/s. Newport). An average of RF spectra over 100 laser shots was considered for analysis. The RF emissions from 7 ns LIB and 30 ps LIB of 80% dense copper compacts were compared to those from the bulk sintered copper sample. The respective RF bands from the ns and ps LIB of bulk sintered copper (as presented in chapter 4) were observed in case of all the compacted powders. The emissions from the ns LIB of the compacts were observed to be in 70-200 MHz range with the most prominent peaks around 144 MHz. Similarly, from the ps LIB of the targets, the emissions were observed in 80-120 MHz range with the most prominent peaks at ~ 103 MHz. However, the amplitude of emissions was observed to vary with respect to the particle size of the compacts. At lower input laser energies, the emissions from ns and ps LIB of bulk sintered target were observed to be very low when

Chapter 5: RF emissions from LIB of copper powder compacts

compared to the compacted copper powders. This trend is seen to be reversed at higher input laser energies.

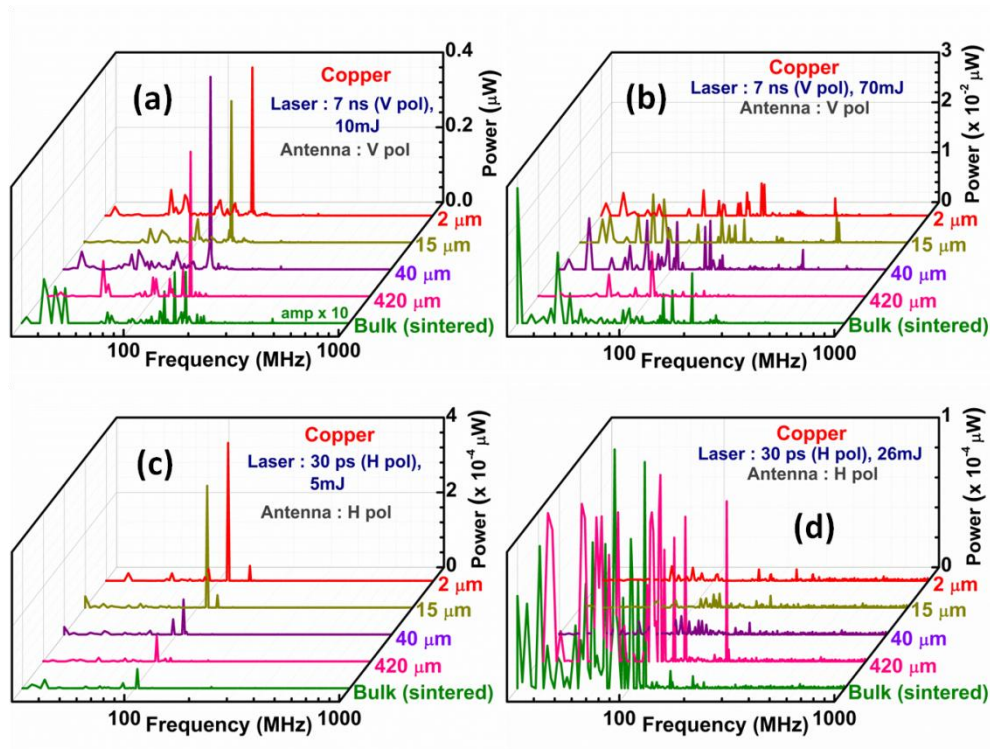


Fig 5.4: RF emissions from ns LIB at (a) 10 mJ (b) 70 mJ and 30 ps LIB at laser energies (c) 5 mJ (d) 26 mJ of 80 % dense copper powder compacts and the bulk sintered copper.

The number of particles that fall within the laser spot diameter ($2\omega_0$) changes with the target material. In case of finer particles, more number of particles (with more number of inter-particle boundaries) fall within $2\omega_0$. Hence, plasma trapping in the interparticle boundaries has an important effect on the observed emissions. Since the focal spot diameter ($\sim 140 \mu\text{m}$ with ns and ps pulses) is relatively low, the laser pulse will hardly see any difference between the bulk sintered sample and the compact of $420 \mu\text{m}$ particles (unless the laser encounters the inter-particle boundaries). Despite, the emissions from $420 \mu\text{m}$ compact was observed to be higher at lower input energies and lower at higher energies. This is due to the difference in the energy transfer from the laser to the target. As a result of high reflection, due to the polished surface, the laser energy absorbed by the bulk sintered copper is low when compared to the powder compacts [167]. This is experimentally confirmed from the reflectance of the 80% dense powder compacts and the bulk sintered copper sample (Figure 5.5).

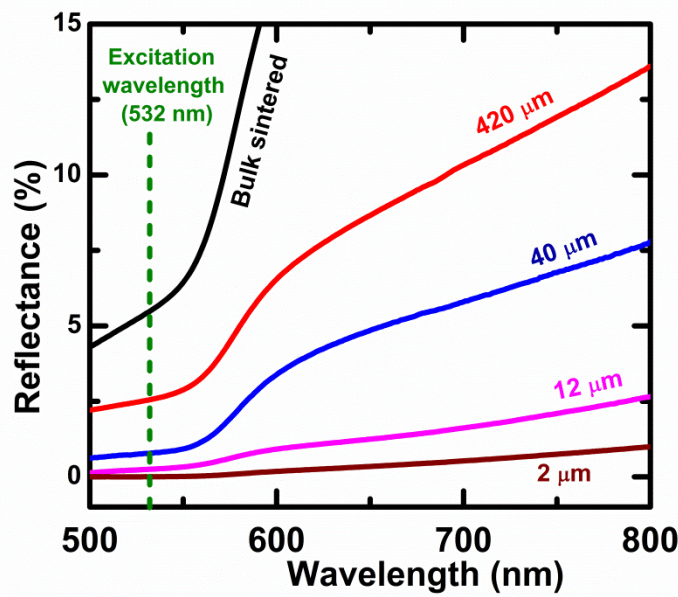


Fig 5.5: Reflectance spectra of bulk sintered copper and 80 % dense compacts of copper powders of different particle sizes. The line shows the laser excitation wavelength (532 nm) used for LIB

The reflectance of laser light, at the excitation wavelength (532 nm), is observed to be proportional to the size of the particles with which the compacts were made up of. When light is scattered by a spherical particle that is neither too smaller nor too larger in diameter, when compared to the wavelength of the incident radiation, the radial and angular dependent solutions of the scattered radiation can be derived from the Mie theory of scattering [168, 169]. The scatterer, under certain conditions, can resonate with the incoming radiation to generate whispering gallery modes (WGM) that can be considered as standing waves which may be decomposed into two counterpropagating waves travelling around the spherical particle. These optical resonances lead to a strong confinement of the electric field around the particle of interaction. The WGM, and the corresponding increase in the local electric field, are a function of the morphology i.e. size, shape and refractive index of the scatterer. Any perturbation in the morphology will lead to the shift in the WGM. Hence, WGM is also called as morphology dependent resonance (MDR) [170]. In this way, the interaction of laser with compacts made up of copper particles of 2 μm, the closest to the excitation wavelength (0.532 μm), results in the strong enhancement in the local electric field. This gives rise in the increased laser-matter interaction and the subsequent increase in RF emissions

from the target made up of 2 μm powders, even at relatively lower input laser intensities. Since the reflection from the bulk sintered target is higher, its degree of breakdown remains the least when compared to the powder compacts. Thus, the RF emissions from the LIB of bulk sintered copper are observed to be relatively low at high energies and high at low laser energies. Thus, the variation in the RF strength was due to the effect of target surface, which gets modified with respect to the size of the particles that are packed. The enhancement in the laser matter interaction, in case of targets with fine particles, gives rise to more seed electrons for the buildup of plasma. Thus, even at lower input energies, the emissions from powder compacts of finer particles are significant compared to those from the compacts of coarser particles and the bulk sintered copper target. At higher input energies, the excessive ionization in case of finer powders reduces the electron-neutral interaction [123]. Thus the RF emissions from the LIB of finer powder compacts fall. The report on higher electron density of LIB of copper nano powders than bulk sintered copper [171] supports the results obtained in our experiments. The RF emissions, from the powder compacts of different particle size with different packing densities, are given in figures 5.6 – 5.13.

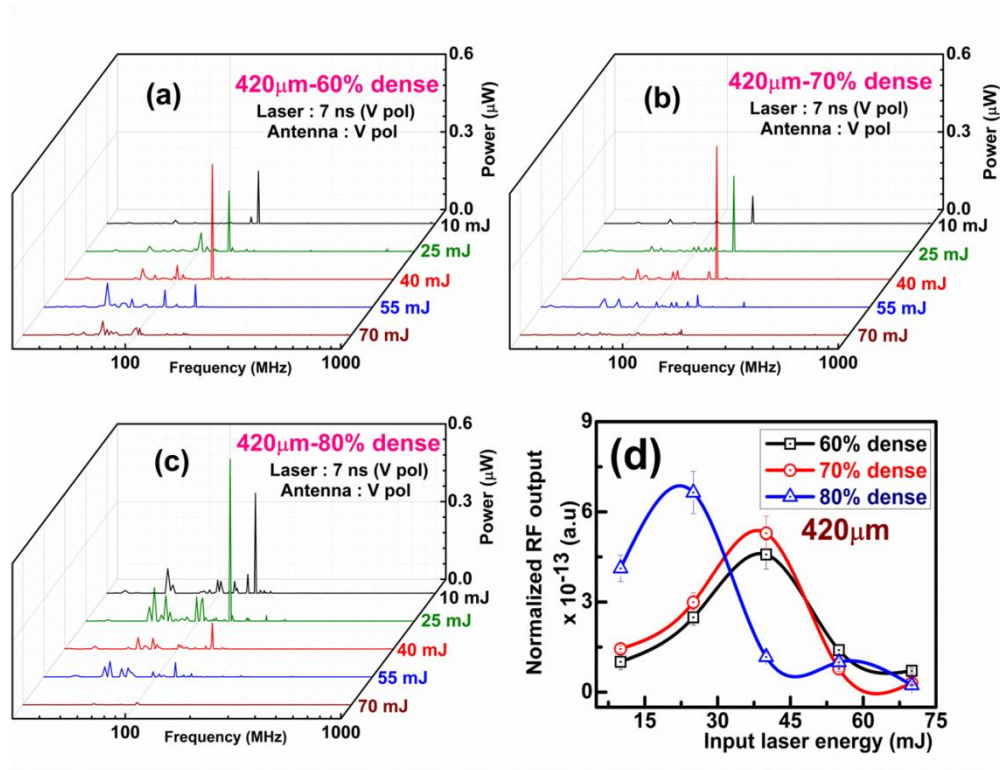


Fig 5.6: RF peaks from 7 ns LIB of 420 μm copper powder packed to (a) 60% (b) 70% (c) 80% density of copper and (d) Normalized RF output from all the three samples

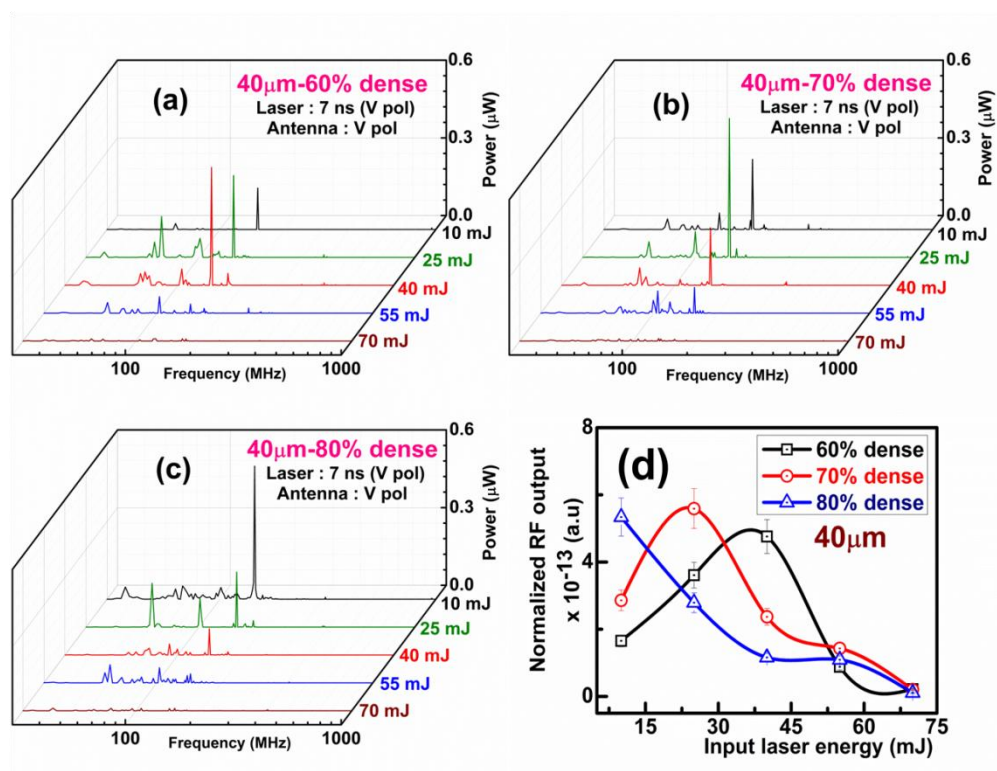


Fig 5.7: RF peaks from 7 ns LIB of 40 μm copper powder packed to (a) 60% (b) 70% (c) 80% density of copper and (d) Normalized RF output from all the three samples

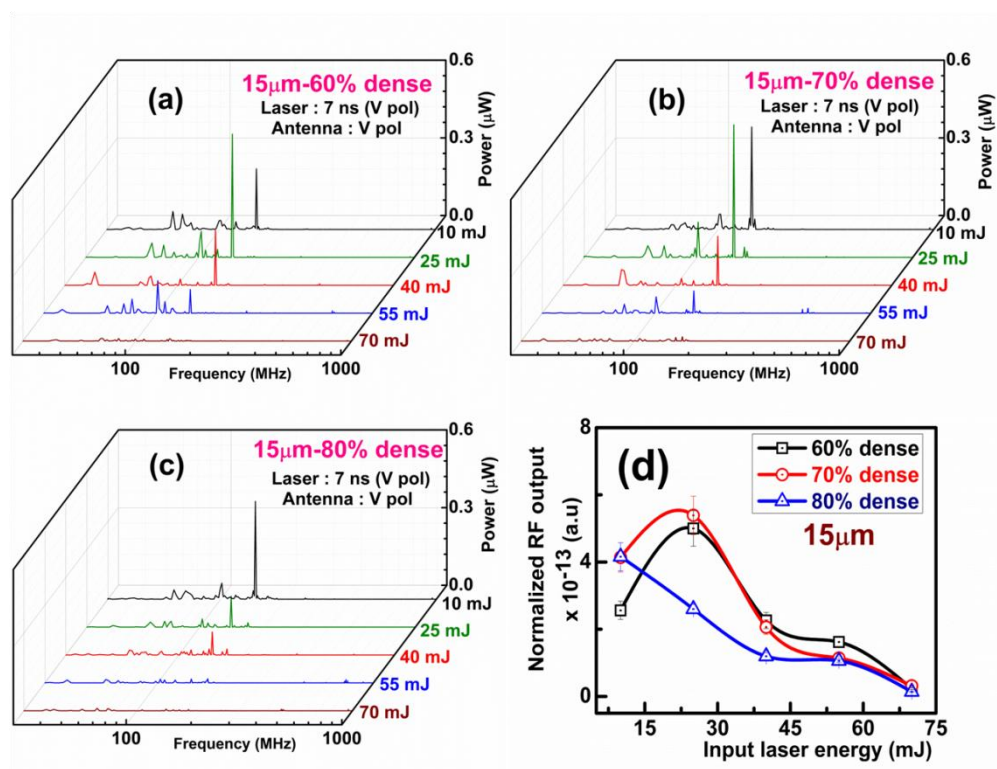


Fig 5.8: RF peaks from 7 ns LIB of 15 μm copper powder packed to (a) 60% (b) 70% (c) 80% density of copper and (d) Normalized RF output from all the three samples

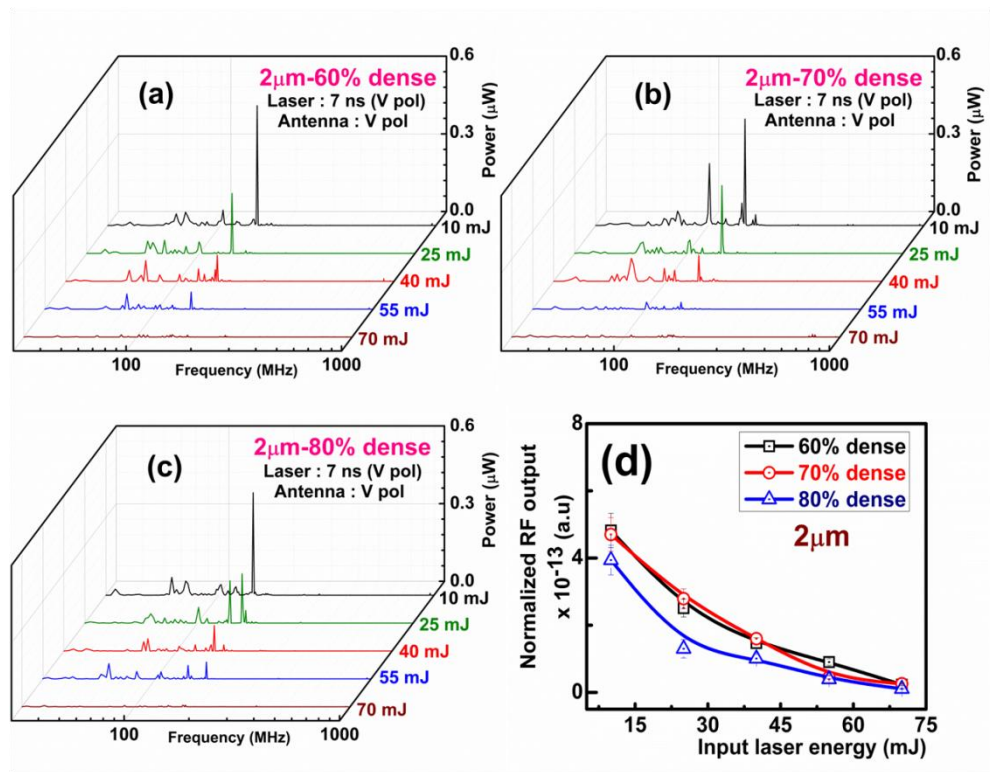


Fig 5.9: RF peaks from 7 ns LIB of 2 μm copper powder packed to (a) 60% (b) 70% (c) 80% density of copper and (d) Normalized RF output from all the three samples

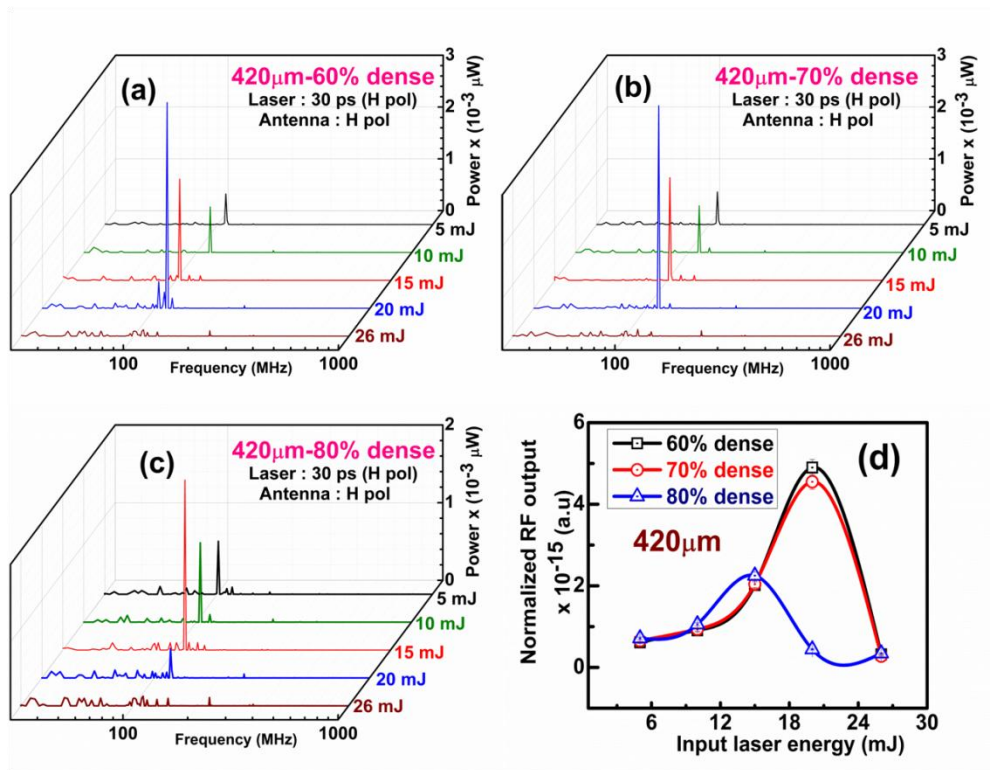


Fig 5.10: RF peaks from 30 ps LIB of 420 μm copper powder packed to (a) 60% (b) 70% (c) 80% density of copper and (d) Normalized RF output from all the three samples

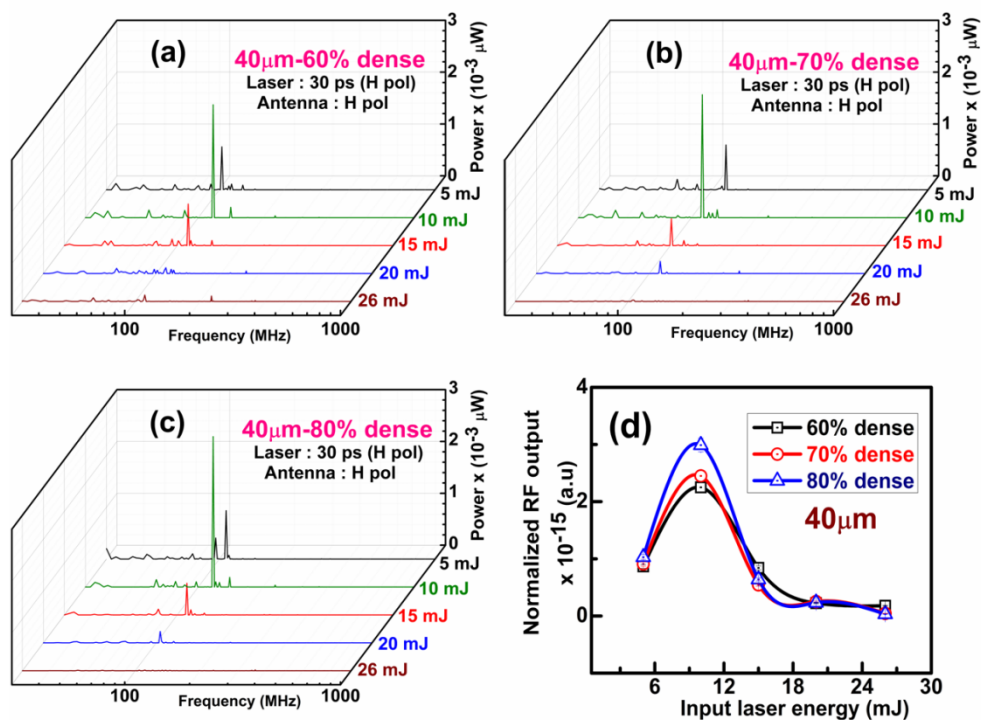


Fig 5.11: RF peaks from 30 ps LIB of 40 μm copper powder packed to (a) 60% (b) 70% (c) 80% density of copper and (d) Normalized RF output from all the three samples

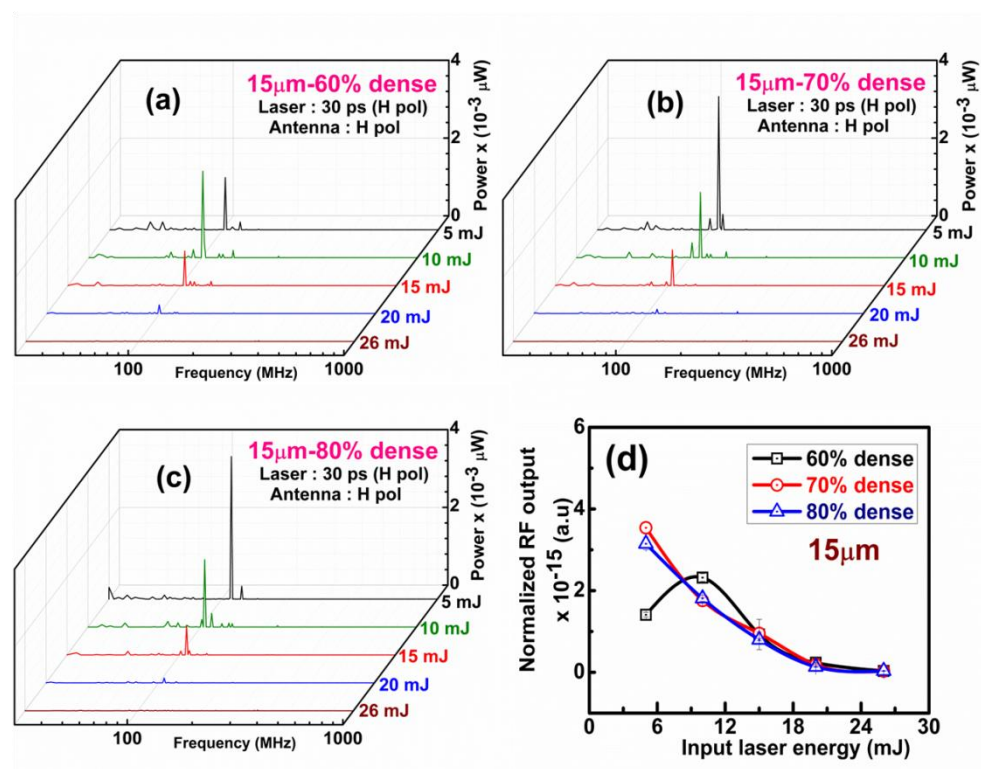


Fig 5.12: RF peaks from 30 ps LIB of 15 μm copper powder packed to (a) 60% (b) 70% (c) 80% density of copper and (d) Normalized RF output from all the three samples

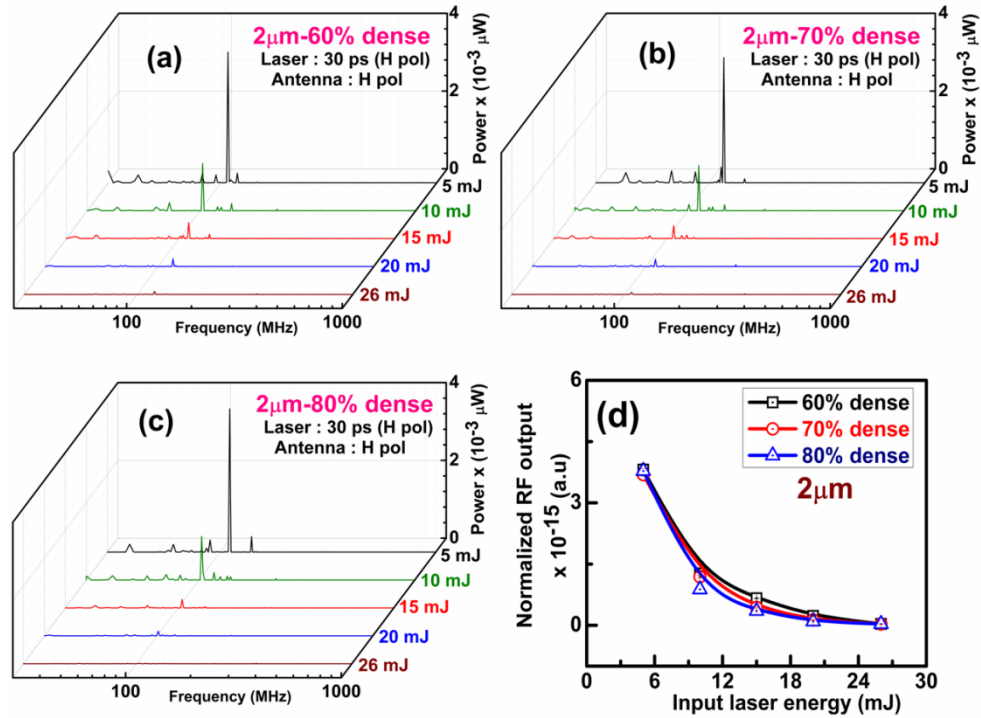


Fig 5.13: RF peaks from 30 ps LIB of 2 μm copper powder packed to (a) 60% (b) 70% (c) 80% density of copper and (d) Normalized RF output from all the three samples

From Figures (5.6 – 5.13), it is observed that the amplitude of emissions depends upon packing density of the particles in the target (besides the size of the particles in the target). However, the respective frequency bands from ns and ps LIB were observed to be invariant with the change in packing density of the target. The normalized RF output was observed to be increasing upto certain input laser energy, beyond which the emissions were observed to fall. For all the samples, with the increase in the packing density, the maximum RF output was observed to be shifted towards the lower Input laser energies. For the maximum packing density studied (80%), the RF emissions were observed to be maximum at lower input laser energies and minimum at higher input laser energies. For example, in case of 80 % dense compacts of 420 μm particles, the maximum RF emissions from ns and ps LIB were observed at 25 mJ and 15 mJ laser energies respectively. For 60% and 70% dense compacts, the maximum RF emissions from ns [Fig 5.6d] and ps LIB [Fig 5.10d] were observed to be at higher input laser energies compared to those from 80% dense samples. This is observed as a consequence of intense breakdown of target (with a fixed particle) with higher packing densities where the number of atoms within the laser spot diameter will be higher.

Chapter 5: RF emissions from LIB of copper powder compacts

The generation of seed electrons and their interaction with the atomic clusters to emit secondary electrons result in the avalanche of electron generation and electron-neutral interaction till the plasma attains equilibrium [6]. Hence, the emission of radiation from the LIB of a particular target increases with the increase in the charge-neutral interaction [123]. At higher laser energies, due to higher plasma recombination rate the charge-neutral interaction comes down. Thus, the RF emissions were observed to fall at higher input laser energies. From the shift of maximum normalized RF output from the LIB of denser samples towards the lower input laser energies, it is understood that the breakdown was intense for samples with higher packing densities. For samples with finer powders and higher packing densities, the breakdown is too intense, to generate RF in the range of detection, within the range of energies under which the studies were carried out. Hence, the raising part of the curves was not observed for targets with finer particles and higher packing. The effect of particle size on the normalized RF output from ns and ps LIB of copper compacts, with fixed packing density, is shown in Fig (5.14 and 5.15).

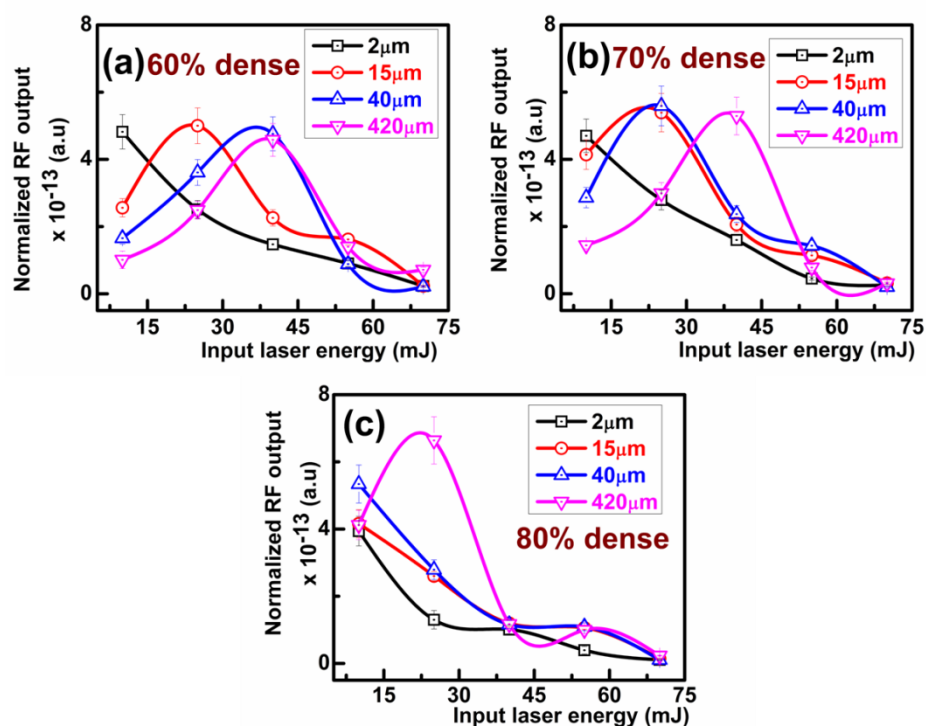


Fig 5.14: Normalized RF output from 7 ns LIB of all the powders compacted to (a) 60% (b) 70% and (c) 80% density of copper

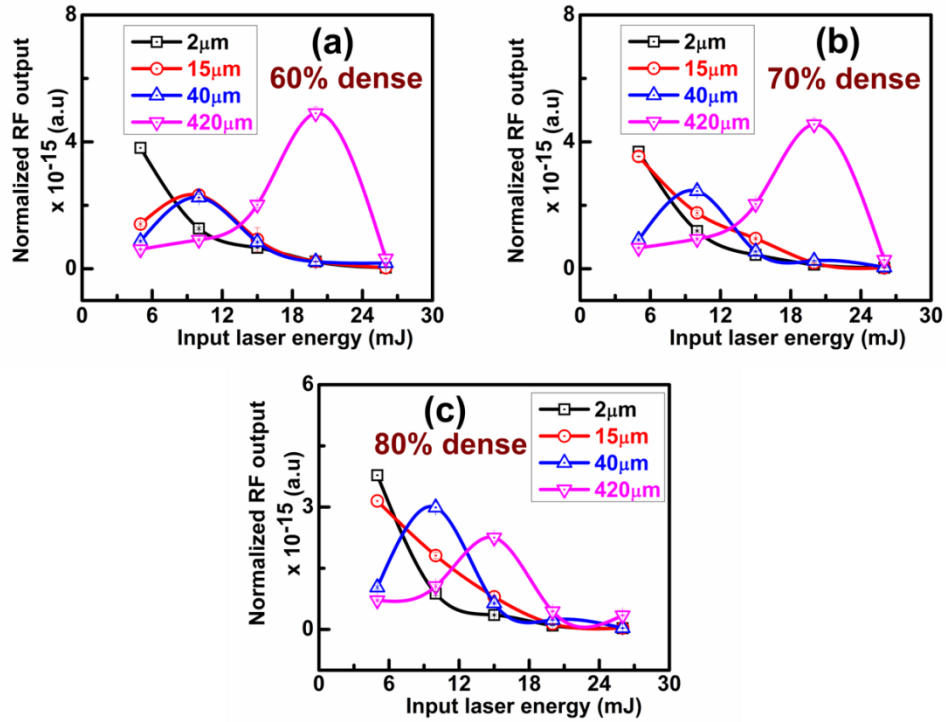


Fig 5.15: Normalized RF output from 30 ps LIB of all the powders compacted to (a) 60% (b) 70% and (c) 80% density of copper

With decreasing particle size, the maximum of the normalized RF output was observed to shift towards the lower input laser energies. For the minimum particle size studied (2 μm), the RF emissions was observed to be maximum at lowest input laser energy used in the studies. Also, for these samples, the RF emissions were observed to be minimum at higher input laser energies. For example, the maximum of RF emissions from ns LIB of 60% dense compacts of 420 μm , 40 μm , 15 μm and 2 μm powders were observed to be at 40 mJ, 40 mJ, 25 mJ and 10 mJ respectively (5.14a). The maximum of RF emissions from ps LIB of 60% dense compacts of 420 μm , 40 μm , 15 μm and 2 μm were observed to be at 20 mJ, 10 mJ, 10 mJ and 5 mJ respectively (5.15a). These are due to the size dependent enhancement in breakdown of targets made up of finer particles. To summarize the effect of particle size and the packing density on RF emissions from the LIB of the compacts, the normalized RF output at two extreme input laser energies, was plotted as a function of particle size of the powders (Fig 5.16 and Fig 5.17).

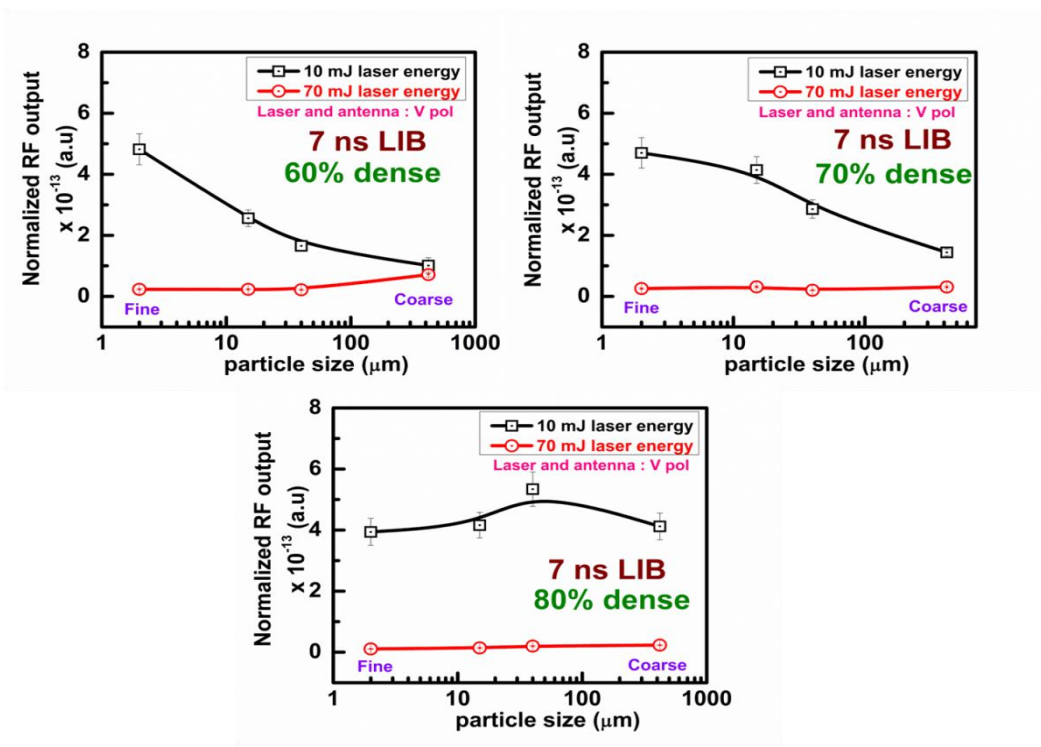


Fig 5.16: Normalized RF output, as a function of particle size of the powders, at the extreme laser energies from 7 ns LIB of all the powders compacted to (a) 60% (b) 70% and (c) 80% density of copper

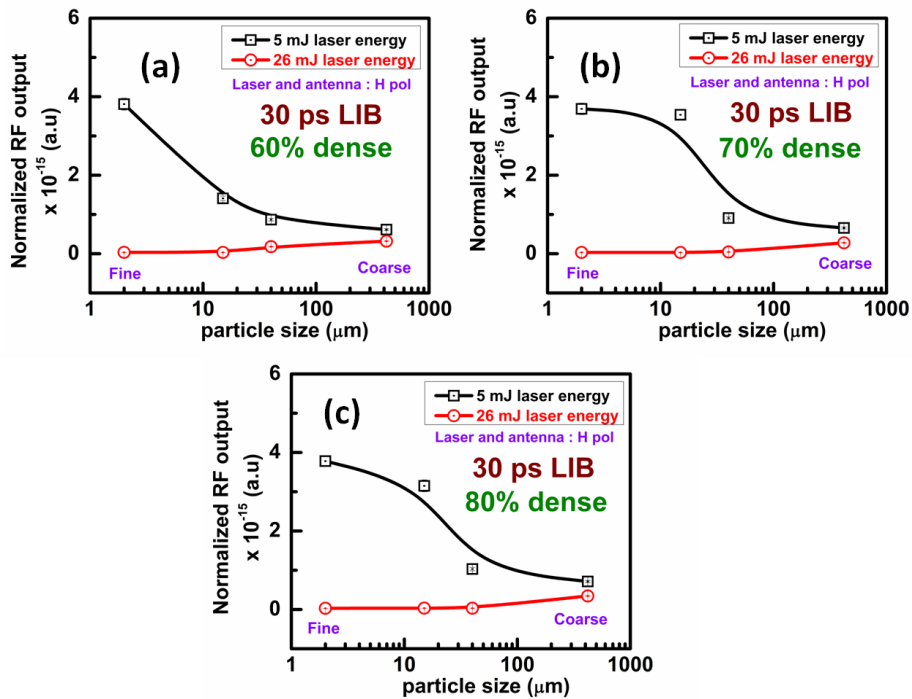


Fig 5.17: Normalized RF output of the samples, as a function of particle size of the powders, at the extreme laser energies from 30 ps LIB of all the powders compacted to (a) 60% (b) 70% and (c) 80% density of copper

From the above plots (Fig 5.16 and Fig 5.17), it is observed that the emissions, at 10 mJ and 5 mJ in case of ns and ps LIBs respectively, increase when the particle size of the target comes down. On the other hand, the emissions, at 70 mJ and 26 mJ in case of ns and ps LIBs respectively, decrease with the decrease in the particle size of the target. This is the evidence, in terms of RF emissions, of increased laser-matter interaction in case of fine particles which offer sufficient electrons to interact with neutrals at low energies and brings down the RF emissions due to excessive ionization at high energies. Hence, in both ps and ns LIBs, the difference in the total RF output at these extreme energies was observed to be higher when the target material is made up of finer particles. The difference in the normalized RF emissions was observed to be decreasing with increasing particle size (Fig 5.16 & 5.17). In case of ns LIB, this difference (in case of coarse particles) was observed to be increasing with the packing density (Fig 5.16) of the compacts unlike in the case of ps LIB (Fig 5.17). This is because of the difference in the laser intensities in case of LIB in ns and ps regimes.

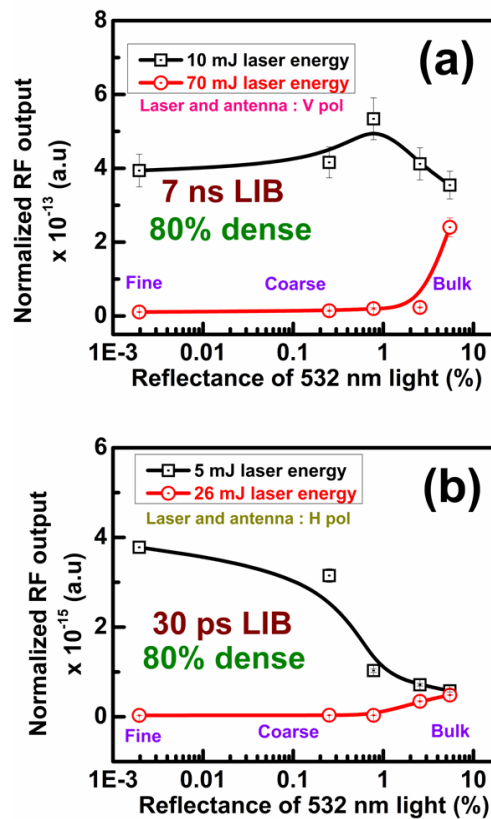


Fig 5.18: Normalized RF output of the samples, as a function of reflectance (at 532 nm) at the extreme laser energies from 80% dense copper samples from (a) ns LIB and (b) 30 ps LIB.

In order to compare the emissions from the LIB of bulk sintered sample to those of compacted powder targets, the normalized RF output was plotted as a function of reflectance of the targets at the excitation wavelength (532 nm). The emissions from the LIB of bulk sintered copper target were compared with those from the 80% dense powder compacts of different particle sizes (Fig 5.18). With the inclusion of the bulk sintered target in the plot, the normalized RF output from LIB, at extreme input laser energies was observed to converge with the increase in the reflectance of the excitation wavelength at the target. Further, the normalized RF emissions from ns LIB of all the copper samples (compacts and the bulk sintered), at high input laser energies, are compared in Fig 5.19.

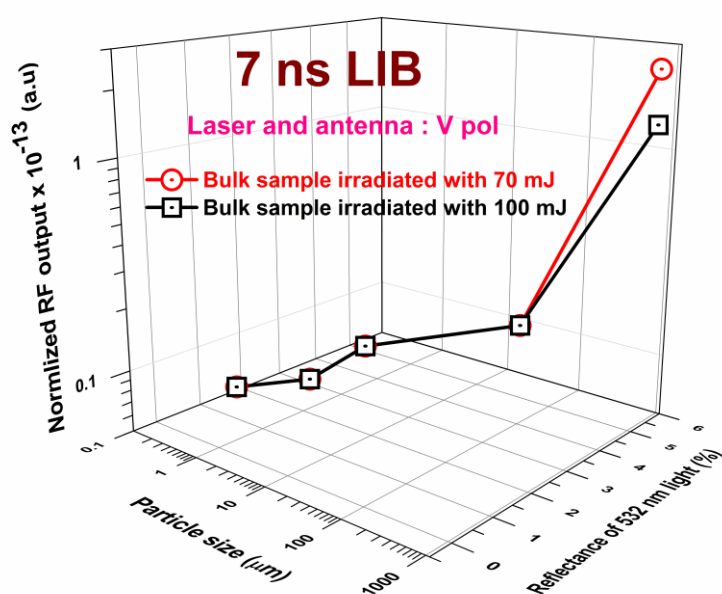


Fig 5.19: Normalized RF output from the ns LIB of the samples (powder compacts and the bulk sintered sample), as a function of granularity at high input laser energies

It is observed that the RF emissions from the LIB of bulk sintered copper sample at 100 mJ is lower than that at 70 mJ. Thus, the strength of emissions from the LIB of bulk sintered sample is observed to be approaching that of the copper compacts. Further increase in the input laser energy will match the strength of emissions from all the samples. Therefore, at high laser intensity and at longer irradiation times, the RF emissions from the LIB of the compacts become more and more similar, as a consequence of hydrodynamic expansion of plasma, to that from the bulk sintered target. The concept of granularity of the target disappears

under these input laser conditions. Similarly, from Fig 5.18 (b), it is evident that the emissions from ps LIB of bulk sintered target, at high input energies, become more similar to those of the powder compacted targets. When laser ablation is carried out with ultrashort pulses, the surface property of the target in the plasma evolution plays a major role. Therefore, from our studies, it is evident that both 7ns and 30 ps pulses are too long to be fit into the ultrafast domain.

The emissions from ns LIB and the ps LIB of the copper powder compacts are compared (Fig 5.20). The major difference between the emissions from ns LIB and ps LIB under similar experimental conditions, besides the frequency bands, is the strength of emissions. The emissions from 7 ns LIB were observed to be almost 2-3 orders higher than those from 30 ps LIB.

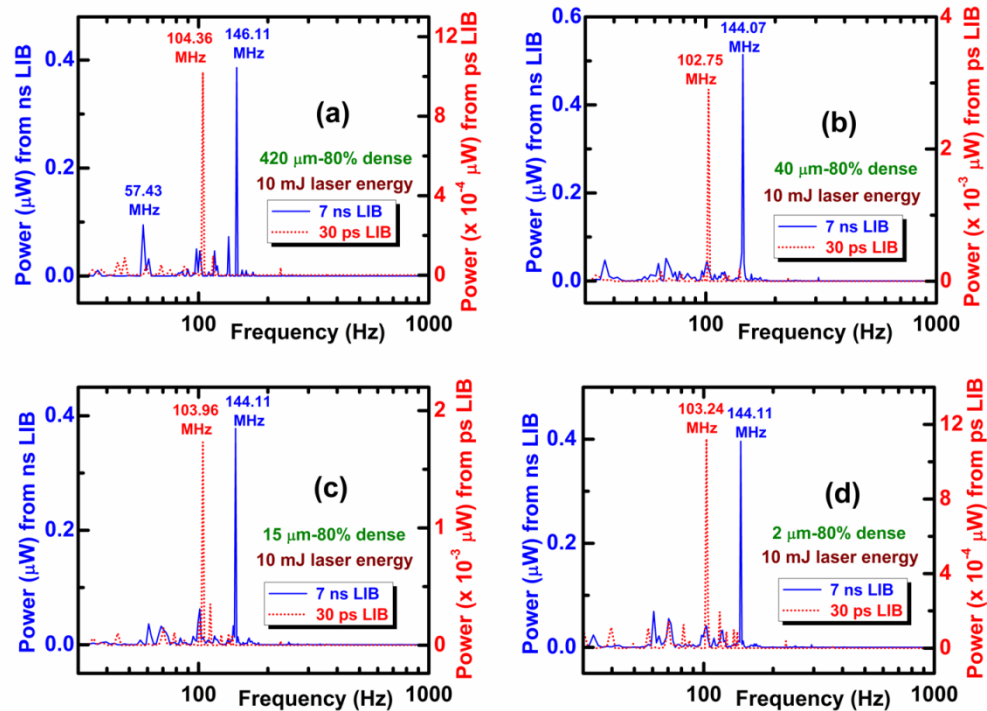


Fig 5.20: Comparison of RF peaks from 7 ns LIB and 30 ps LIB of 80% dense copper compacts made of particles of size (a) 420 μm (b) 40 μm (c) 15 μm and (d) 2 μm

Since the intensity of ps pulses is two orders more than that of the ns pulses, the breakdown is intense in the ps regime [124]. Because of this, the value of electron density will be high which in turn will reduce the thermalization time [125]. Thus the plasma from ps LIB will attain the equilibrium state relatively sooner than that from ns LIB. Also, ns pulses, due to relatively longer duration, thermalize the

Chapter 5: RF emissions from LIB of copper powder compacts

plasma more compared to ps pulses [172]. Therefore, the recombination rate is much higher in case of ps LIB and thus the emissions from ns LIB is observed to be about two orders higher than those from ps LIB.

In summary, the RF emissions from ns and ps LIB of copper targets of different particle sizes and packing densities were studied. These results suggest that the laser matter interaction is different for targets with different particle size and packing density. When compared with the emissions from the sintered sample, the emissions from the powder compacts were observed to be lower and higher at low and high input laser energies respectively. This is due to the difference in the surface properties of unsintered samples which, due to their surface roughness, absorb most of the input laser radiation. On the other hand sintered samples which, due to their highly polished surfaces, reflect away most of the incident input radiation. The generation of seed electrons and the subsequent avalanche breakdown requires very low laser energies in case of targets with finer particles and high packing densities. Therefore, when the target (with a particular packing density) is composed of smaller particles, via enhanced local field effect, the breakdown (under same experimental conditions) becomes relatively intense than those with targets (of same density) composed of larger particles. As a result of this, the RF emissions, from the LIB of these samples, attain the peak at relatively lower input laser energies. At the same time, due to very intense breakdown at higher input laser energies, the probability of charge-neutral interaction becomes very less. Hence, there is hardly any RF emission from these samples at higher input laser energies. Thus, the RF emissions can be manipulated by tuning the surface properties of the target materials. As per the studies carried out, the RF emissions are maximum under the following conditions.

Table 5.2: Conditions under which the RF emissions are maximum

Laser/ Experimental parameters	7 ns LIB	30 ps LIB
Laser energy	10 mJ	5 mJ
Laser polarization	Vertical	Horizontal
Antenna polarization	Vertical	Horizontal
Particle size of the target material	2 μ m	2 μ m
% of theoretical density of the target material	80	80

Chapter 5: RF emissions from LIB of copper powder compacts

In general, when the target is fine powder particles compacted into a highly dense material, the RF emissions can be maximized under minimum input laser energies under same antenna and laser polarization conditions. Since the RF emissions follow a specific pattern of variation with respect to particle size and the compact density, these studies can be extended to the in situ monitoring of densification and the evaluation of the corresponding sample microstructure during any laser based sintering and welding of materials [173].

**This page is
intentionally
left blank**

Chapter VI

Radio emissions from laser induced breakdown of high energy materials

This chapter contains the results of the studies carried out on the observation and characteristics of RF emissions from ns and ps LIB of high energy materials (HEMs).

LIB of a HEM is analogous to the small scale replication of the corresponding HEM in reaction. Hence, the energy release from the LIB of HEMs can help in the understanding of the dynamics of the reacting HEM. The RF emissions from the LIB of HEMs, with a particular laser, were observed to be similar. However, the emissions from the compounds that contain nitrogen and NO₂ groups were observed to be different from those from the compounds that do not contain nitrogen. The emissions are observed to match with the ion plasma frequencies (ω_{pi}) which confirms the significance of nitrogen in the RF emissions. Thus, the studies on RF emissions from the ns and ps LIB of HEMs seem to be promising in differentiating compounds that have nitrogen and that are nitrogen free. Therefore, the development of a tool for the detection of explosives from the RF emissions from LIB is possible. The laser matter-interaction and the associated dynamics decide the RF emissions from LIB. Hence, the frequencies and amplitudes of RF emissions from the LIB of HEMs were observed to be different with ns and ps laser pulses.

6.1 Introduction

High energy materials are those in which large amount of chemical energy is stored in. When triggered, under certain conditions, the stored chemical energy is released in different forms i.e. kinetic, thermal, electromagnetic, mechanical etc [174]. HEMs can be explosives or non explosives. Based on the chemical properties they can be classified as given in Fig 6.1.

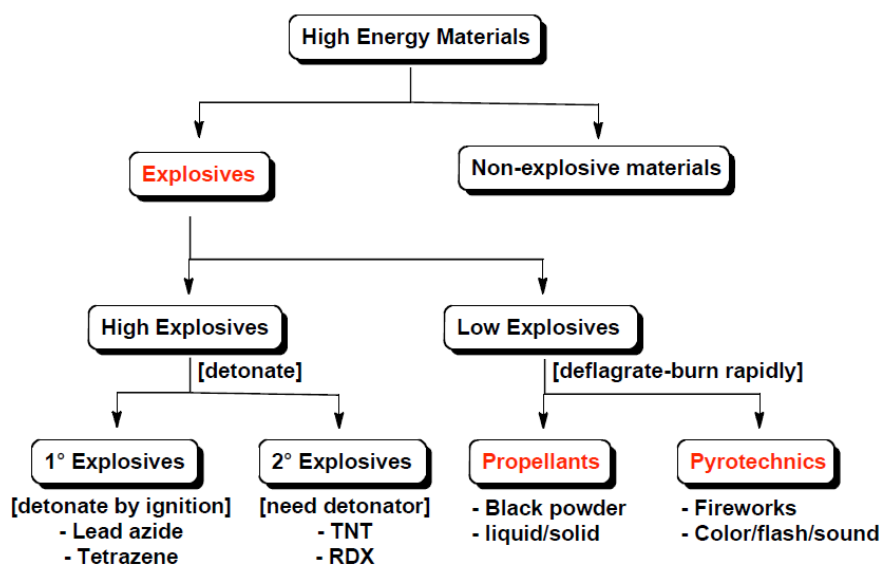


Fig 6.1: Classification of High energy materials (HEMs). Taken from [166]

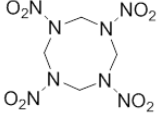
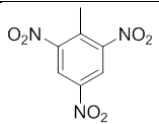
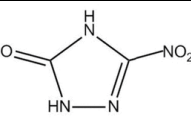
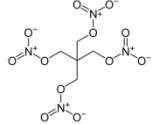
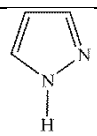
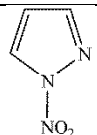
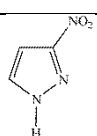
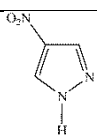
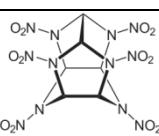
An HEM can be a material made up of single chemical compound or combination of different compounds in any of the physical states (solid, liquid or gas). A reaction of HEM at relatively faster rate is termed as detonation ($5000 - 10000 \text{ ms}^{-1}$) whereas the slower reaction rate of explosives is known as deflagration ($300 - 3000 \text{ ms}^{-1}$) or burning. With the supply of external energy, the detonation of an explosive can be achieved. The explosive materials that are very sensitive and are exploded due to small amount of excited energy are called as primary explosives. The other type of explosives that hardly react to mechanical and thermal energies but detonate due to the explosion of primary explosives are called as secondary explosives. The material that demarcate the primary and secondary explosives are Pentaerythritol tetranitrate (PETN) where any explosive more sensitive than PETN is categorized under primary explosives. The chemical compounds that are used to produce energy for the fluid movement or vehicle/projectile propulsion is called as propellants. The science of utilizing compounds to undergo self-

Chapter 6: RF emissions from LIB of HEMs

contained/self-contained exothermic chemical reactions to generate thermal, mechanical, electromagnetic energies are called pyrotechnics. When a HEM is considered for any application chemical/thermal stability, sensitivity, oxygen balance, heat of formation/explosion, gases evolved, detonation pressure/velocity and explosive power are the important characteristics to be taken care of [174].

A reacting HEM releases a large amount of heat and pressure by rapid self-sustaining exothermic decomposition reaction. The temperature generated is in the range of 3000 – 5000°C and the gases produced expand almost around 12000 – 15000 times than the original volume. The entire phenomenon takes place in a few microseconds, accompanied by a shock and loud noise. In the previous chapters, the phenomena similar to the reaction of HEMs, in a controlled manner, are mimicked in the lab by the breakdown of different target materials using pulsed laser sources. As mentioned in chapter 1, the temperature of the plasma due to LIB will be of the order of 3000-10,000 K which is similar to that of a reacting HEM. In this way, LIB of HEMs, in a lab controlled environment, will be the small scale replication of a reacting HEM. Therefore, laser ablation of HEMs is an effective route to systematically study the science of energy release of a reacting HEM. The understanding of the distribution of energy and the dynamics of HEMs, during reaction, is crucial to develop applications in the areas of defense and security. Remote and wireless detection of hazardous materials, under ambient environment, is one of the areas under investigation for a long time and also the need of the hour. The propagation over longer distances with least attenuation makes RF radiation a potential candidate to be considered for this purpose. The material specific emissions reported in chapter 4, suggests the possibility of identification of the materials, besides detection. Based on these, the studies on laser-HEM interaction and their energy release in the RF range of frequencies were initiated. Trinitrotoluene (TNT), Cyclonite (RDX), Pentaerythritol tetranitrate (PETN), nitrotriazalone (NTO), Pyrazoles [175], Hexanitrohexaazaiso (CL20) and Sodium azide (NaN_3) were the high energy organic molecules used in the studies. The details of these HEMs are given in table 6.1

Table 6.1: Details of the HEMs studied

Commonly known as	IUPAC nomenclature	Structure	Chemical formula	No of NO ₂ groups
RDX	1,3,5-Trinitroperhydro-1,3,5-triazine		C ₃ H ₆ N ₆ O ₆	4
TNT	2-Methyl-1,3,5-trinitrobenzene		C ₇ H ₅ N ₃ O ₆	3
NTO	3-Nitro-1,2,4-triazol-5-one		C ₂ H ₂ N ₄ O ₃	1
PETN	[3-Nitrooxy-2,2-bis(nitrooxymethyl)propyl] nitrate		C ₅ H ₈ N ₄ O ₁₂	4
Pyrazole	Pyrazole		C ₃ H ₄ N ₂	0
1-N-Pyrazole	1-Nitropyrazole		C ₃ H ₃ N ₃ O ₂	1
3-N-Pyrazole	3-Nitropyrazole		C ₃ H ₃ N ₃ O ₂	1
4-N-Pyrazole	4-Nitropyrazole		C ₃ H ₃ N ₃ O ₂	1
CL20	2,4,6,8,10,12-hexanitro-2,4,6,8,10,12-hexaazaisowurtzitane		C ₆ H ₆ N ₁₂ O ₁₂	6
Sodium azide	-	Na ⁺ N ⁻ =N ⁺ =N ⁻	NaN ₃	0

6.2 Results and discussion

These HEM powders were compacted into pellets (of decent handling strength) of 10 mm diameter. The RF emissions from 7 ns and 30 ps LIB of these targets under similar laser and antenna polarization, considering the average of RF spectra over 100 single-shot LIB, are shown in Fig 6.2 and 6.3 respectively.

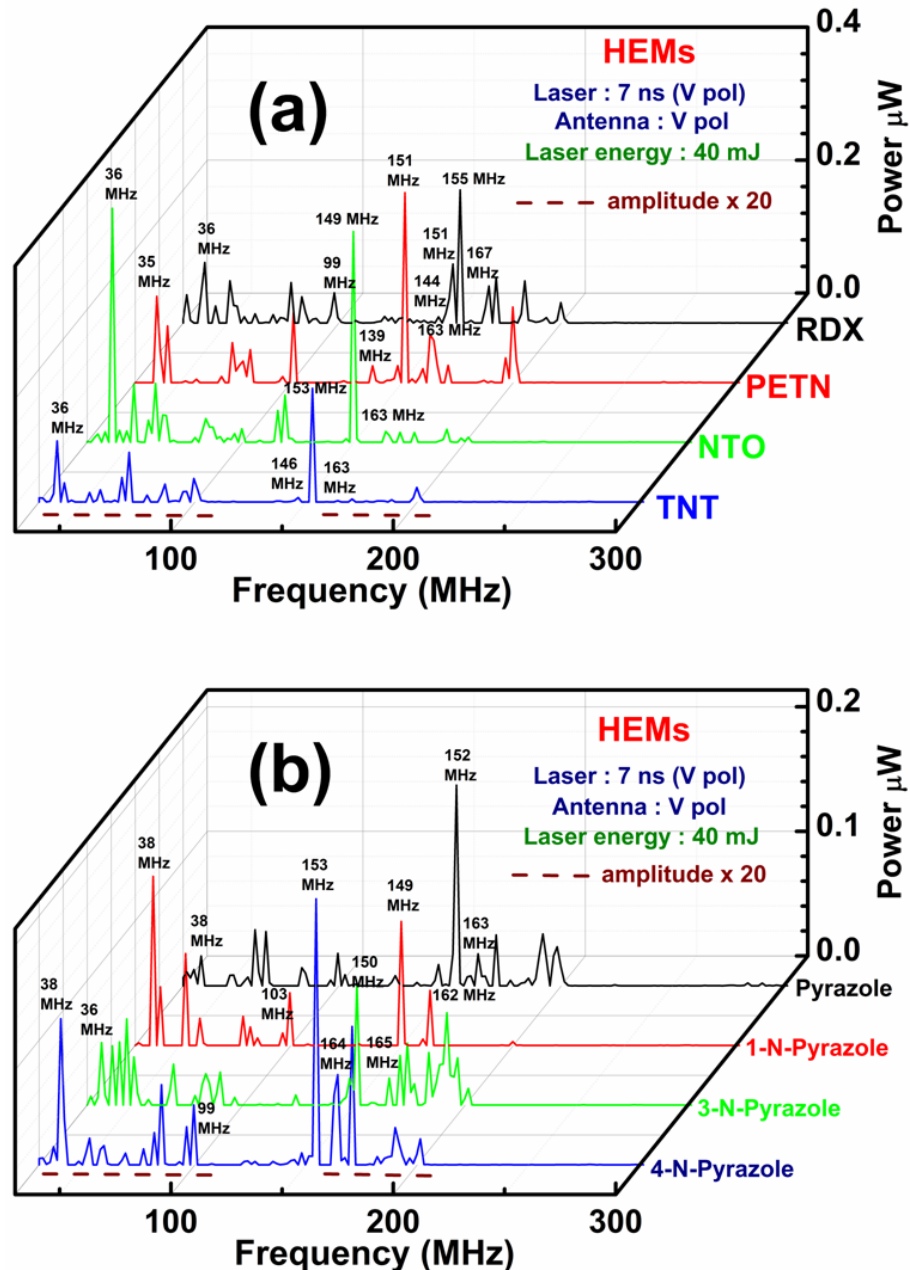


Fig 6.2: RF emissions from ns LIB of (a) primary explosives (PETN, NTO) & secondary explosives (RDX, TNT) and (b) Pyrazole explosives under similar laser and antenna polarization.

The dashed lines represent the bands that are multiplied by 20 to view the signals better

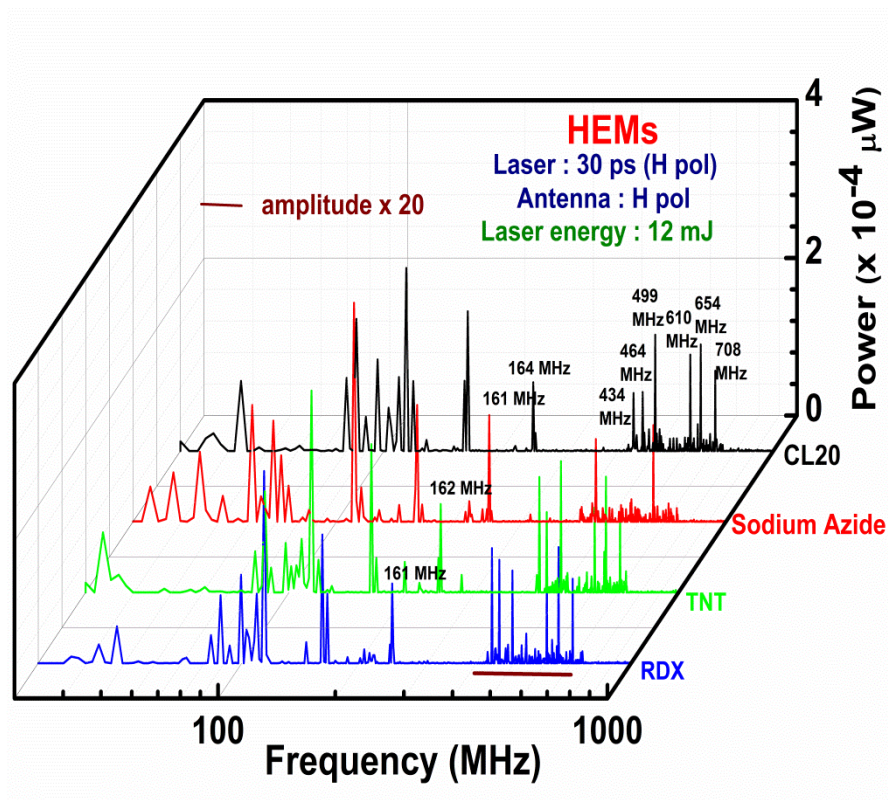


Fig 6.3: RF emissions from ps LIB of HEMs under similar laser and antenna polarization. The lined region represents the bands that are multiplied by 20 to view the signals better

The RF spectra from ns and ps LIB of the different HEMs studied, were observed to be similar with common emission bands. For example, from the RF spectra of ns LIB of all the HEMs, the band at ~150-155 MHz was observed to be dominant (Fig 6.2a and 6.2b). However, other regions of the spectra were amplified (by multiplying the power by a factor of 20) to see several frequency bands which are confined upto ~ 200 MHz. The RF bands in the amplified region of the spectra from the ns LIB of all the organic molecules were observed to be similar, barring a few alterations. Similarly, the RF emissions from ps LIB of the organic molecules studied, were observed to be confined upto 300 MHz (Fig 6.3) with many common frequency bands. The dominant RF emissions from ps LIB from all the organic molecules were observed to be at ~120 MHz. Other than this, the bands at ~160-165 MHz and ~240-245 MHz were observed to be common from the ps LIB of all the HEM targets. The observed RF frequency bands from ns and ps LIB of high energy organic molecules are summarized in tables 6.2 and 6.3 respectively.

Chapter 6: RF emissions from LIB of HEMs

Table 6.2: Prominent RF bands from ns LIB of HEMs

Sample	Chemical formula	RF peak (MHz)
RDX	$C_3H_6N_6O_6$	30-55, 65-97, 145-156, 164-174, 181-198
PETN	$C_5H_8N_4O_{12}$	38-46, 70-83, 96-103, 137-172, 194-202
NTO	$C_2H_2N_4O_3$	33-67, 70-83, 96-103, 137-172, 194-202
TNT	$C_7H_5N_3O_6$	30-45, 51-102, 148-154, 193-201
1-N-Pyrazole	$C_3H_3N_3O_2$	30-43, 51-62, 81-101, 148-165
3-N-Pyrazole		30-54, 70-98, 148-156, 164-203
4-N-Pyrazole		30-61, 67-103, 153-173, 188-203
Pyrazole	$C_3H_4N_2$	30-42, 51-70, 81-104, 143-172, 180-201

Table 6.3: RF bands from ps LIB of HEMs

Sample	Chemical formula	RF peaks (MHz)
Hexanitrohexaazaiso (CL20)	$C_6H_{12}N_6O_{12}$	80-120, 160-165, 240-245, 430-710
Sodium azide	NaN_3	30-80, 110-120, 160-165, 240-245, 430-710
TNT	$C_7H_5N_3O_6$	80-120, 160-165, 240-245, 430-710
RDX	$C_3H_6N_6O_6$	80-120, 160-165, 240-245, 430-710

From the ns LIB of all the organic compounds studied (which contain similar elemental compositions), most of the emissions were observed to be in 30-100 MHz and 135-200 MHz bands. Similarly, In case of ps LIB, the emissions in 80-120 MHz, 160-165 MHz and 240-245 MHz bands were observed in case of all the target materials. However, ps LIB of sodium azide (NaN_3), which is made up only of sodium and nitrogen, was observed to emit radiation in 30-80 MHz band unlike those from the other CHNO compounds. Also, the emissions in 80-110

MHz band (prominent from other HEMs) from the ns LIB of NaN_3 were observed to be missing. To further narrow down, the emissions from naphthalene (C_{10}H_8) which contains only carbon and hydrogen were considered in the analysis. The RF emissions from ns and ps LIB of naphthalene are shown in Fig 6.4.

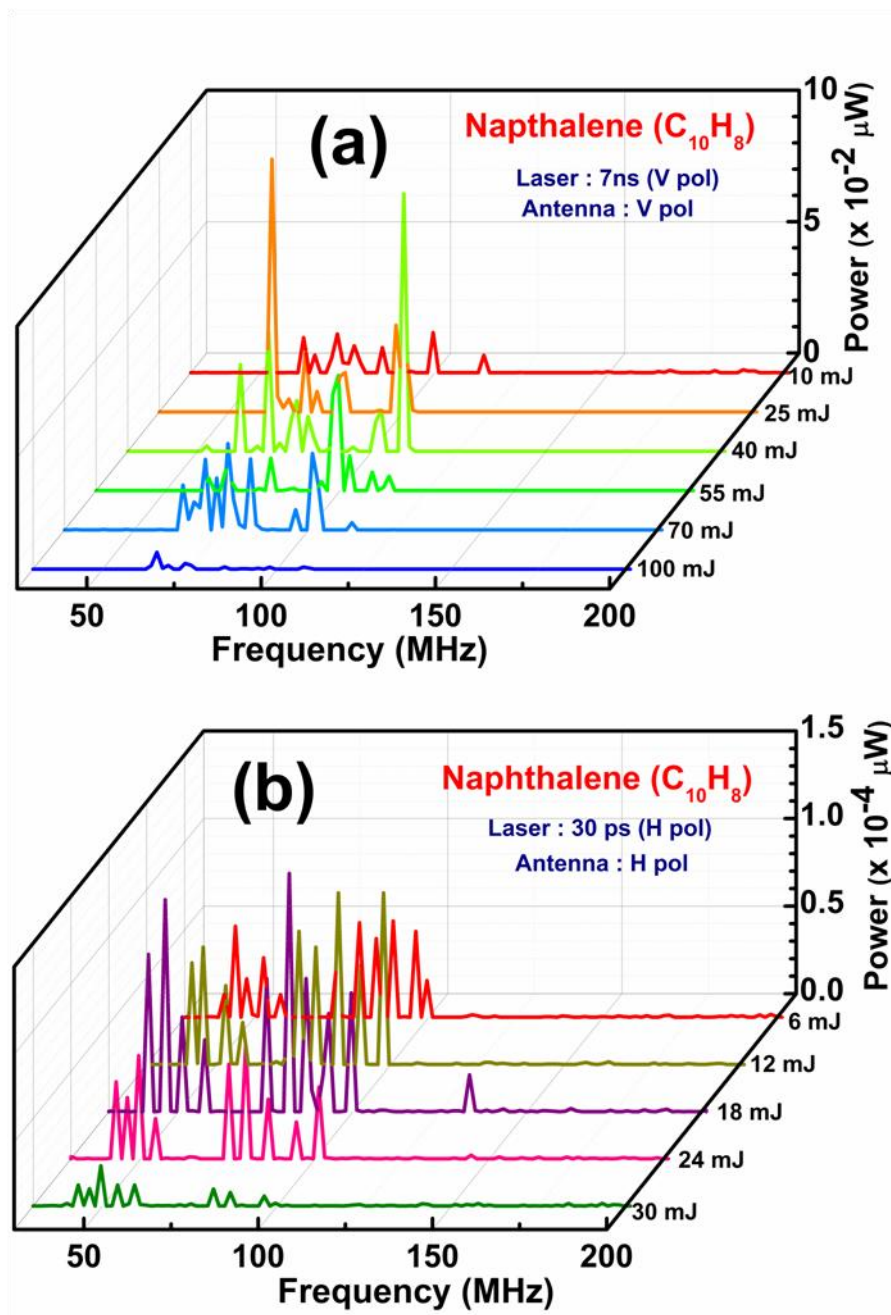


Fig 6.4: RF emissions from (a) ns and (b) ps LIB of naphthalene

The emissions from ns LIB of naphthalene were observed to be in ~ 70 - 110 MHz (Fig 6.4a). Also no prominent peaks were observed around ~ 150 - 155 MHz as in

the organic compounds that contain nitrogen. To confirm these results, the emissions from other nitrogen free organic molecules (studied in chapter 4) were compared with those from HEMs. The emissions from ns LIB, under similar experimental conditions, of different organic compounds made up of different combination of elements are shown in Fig 6.5.

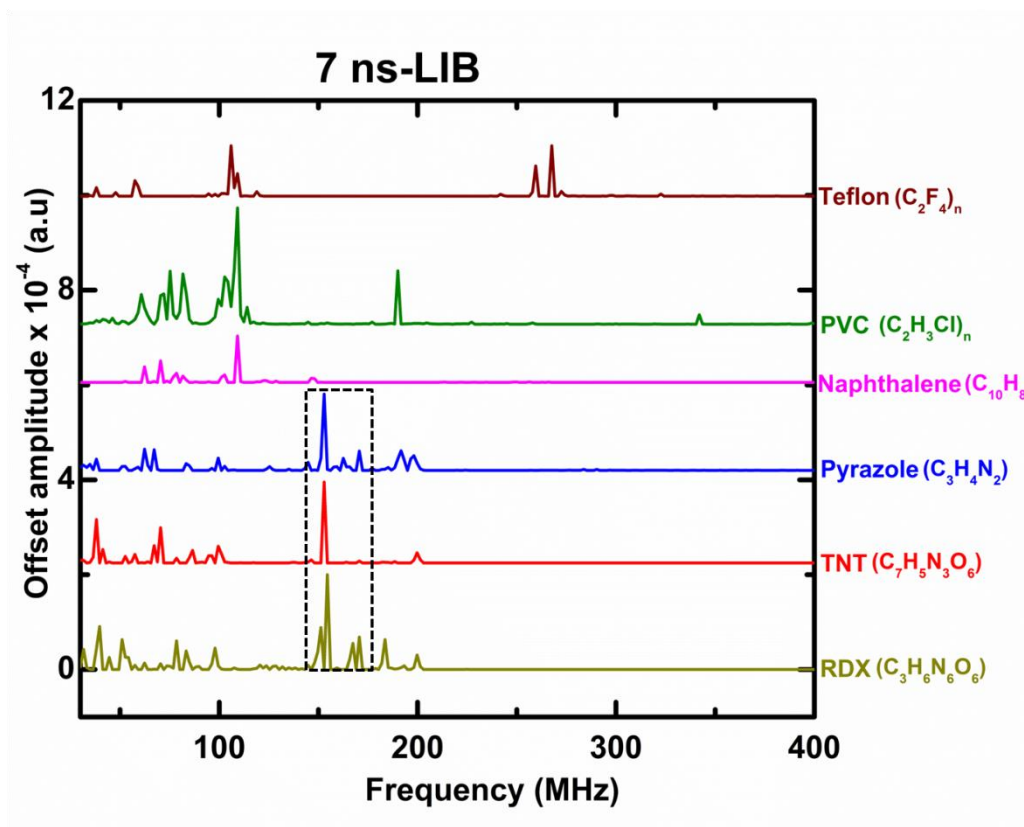


Fig 6.5: RF emissions from ns LIB of different organic molecules

All the organic molecules compared in figure 6.5 are observed to emit radiation in the 30-100 MHz on their respective breakdown with ns laser pulses. The emissions at ~ 110-120 MHz band were observed to be dominant in naphthalene, PVC and teflon which are nitrogen free. There is no observation of spectral lines in this zone of frequencies from the ns LIB of the HEMs. However, the emission of ~150-155 MHz band was observed only in case of nitrogen based high energy compounds. The ns LIB of Pyrazole, that does not possess oxygen, contain the 155 MHz peak as the other CHNO compounds. Also, Naphthalene that is made up only with carbon and oxygen does not contain peak at 155 MHz. Therefore, prominent emission line (155 MHz) seems to signify the importance of nitrogen. In case of ps LIB of naphthalene, the emissions were observed in 45-70 MHz and

80-100 MHz frequency bands (Fig 6.4b). No frequency lines were observed beyond 150 MHz as in the HEM compounds. To check this, the emissions from ps LIB of all the organic compounds studied in chapter 4 were compared with those from the HEMs. (Fig 6.6)

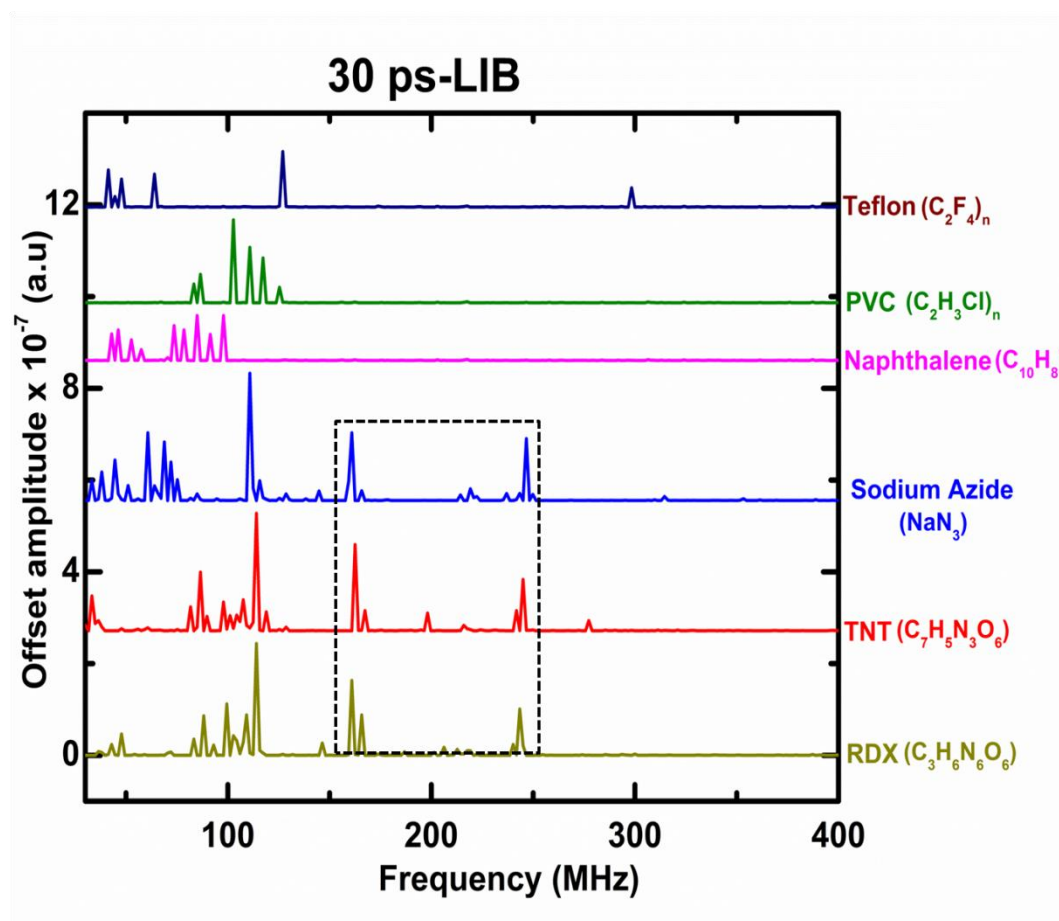


Fig 6.6: RF emissions from ns LIB of different organic molecules

The emissions from ps LIB, of all the molecules compared, are observed to have many lines from 30-130 MHz. Barring a peak at ~ 315 MHz from teflon, there was no significant emission line observed from the LIB of nitrogen free compounds. The spectra from the ps LIB of all the HEMs, which are made up of nitrogen, were observed have 160-165 and 240-245 bands that are absent in the nitrogen free organic molecules. This again appears to signify nitrogen presence in the HEMs. In order to understand the origin of the RF emissions, considering that the target is singly ionized, the ion plasma frequencies (ω_{pi}) of the possible atomic and molecular species of the targets, in case of ns LIB and ps LIB, were estimated using equation 3.1 as in chapter 3. The electron density (n_e) values for

Chapter 6: RF emissions from LIB of HEMs

some of the samples are estimated from LIBS experiments while that for the rest of the samples were obtained from the literature [176], under similar intensity conditions. Table 6.4 gives the estimated values of ion plasma frequencies in case of ns and ps LIB of the HEM targets.

Table 6.4: Estimated ion plasma frequencies (ω_{pi}) of LIB of HEMs

Parameters	Laser intensity (W/cm ²)	Electron density (n _e) range (cm ⁻³)	Estimated ion plasma frequency range (MHz)	
			Atomic species	Molecular species
7 ns LIB	~2×10 ¹⁰	2.5×10 ¹⁶ – 2.6×10 ¹⁶	C ⁺ : 162-164 O ⁺ : 140-143 N ⁺ : 150-152 H ⁺ : 571-577	(C ₃ H ₆ N ₆ O ₆) ⁺ : 38 (C ₅ H ₈ N ₄ O ₃) ⁺ : 32 (C ₂ H ₂ N ₄ O ₃) ⁺ : 58 (C ₇ H ₅ N ₃ O ₆) ⁺ : 38 (C ₃ H ₄ N ₂) ⁺ : 68 (C ₃ H ₃ N ₅ O ₂) ⁺ : 53 (C ₂) ⁺ : 115-119 (H ₂) ⁺ : 393-399 (O ₂) ⁺ : 99-102 (N ₂) ⁺ : 106-113
30 ps LIB	~9×10 ¹¹	4.8×10 ¹⁷ - 5×10 ¹⁷	C ⁺ : 705-707 O ⁺ : 608-612 N ⁺ : 652-655 H ⁺ : 2487-2489	(C ₃ H ₆ N ₆ O ₆) ⁺ : 163 (C ₆ H ₁₂ N ₆ O ₁₂) ⁺ : 163 (C ₇ H ₅ N ₃ O ₆) ⁺ : 164 (NaN ₃) ⁺ : 162 (C ₂) ⁺ : 498-502 (H ₂) ⁺ : 1706-1710 (O ₂) ⁺ : 432-435 (N ₂) ⁺ : 461-465

It is evident that the emitted radio frequencies, shown in figures 6.2 and 6.3, correspond to the estimated ion-plasma frequencies shown in tables 6.4. The estimated values are observed with ± 3 MHz frequency error, which is the maximum resolution of the spectrum analyzer. Therefore the emissions can be accounted for the charge-neutral interactions where the role of ions is prominent. Also, the highlighted portions of the spectra given in figure 6.5 and 6.6 can be accounted for the presence of nitrogen in the compound. Therefore, the emissions that signify the presence of nitrogen may be the starting point of the wireless detection of HEMs. However, the basic differences in the appearance of bands from the ns and ps LIB and their corresponding differences in the amplitudes from HEMs are to be understood. The comparison of emissions from ns and ps LIB of the HEMs are given in Fig 6.7

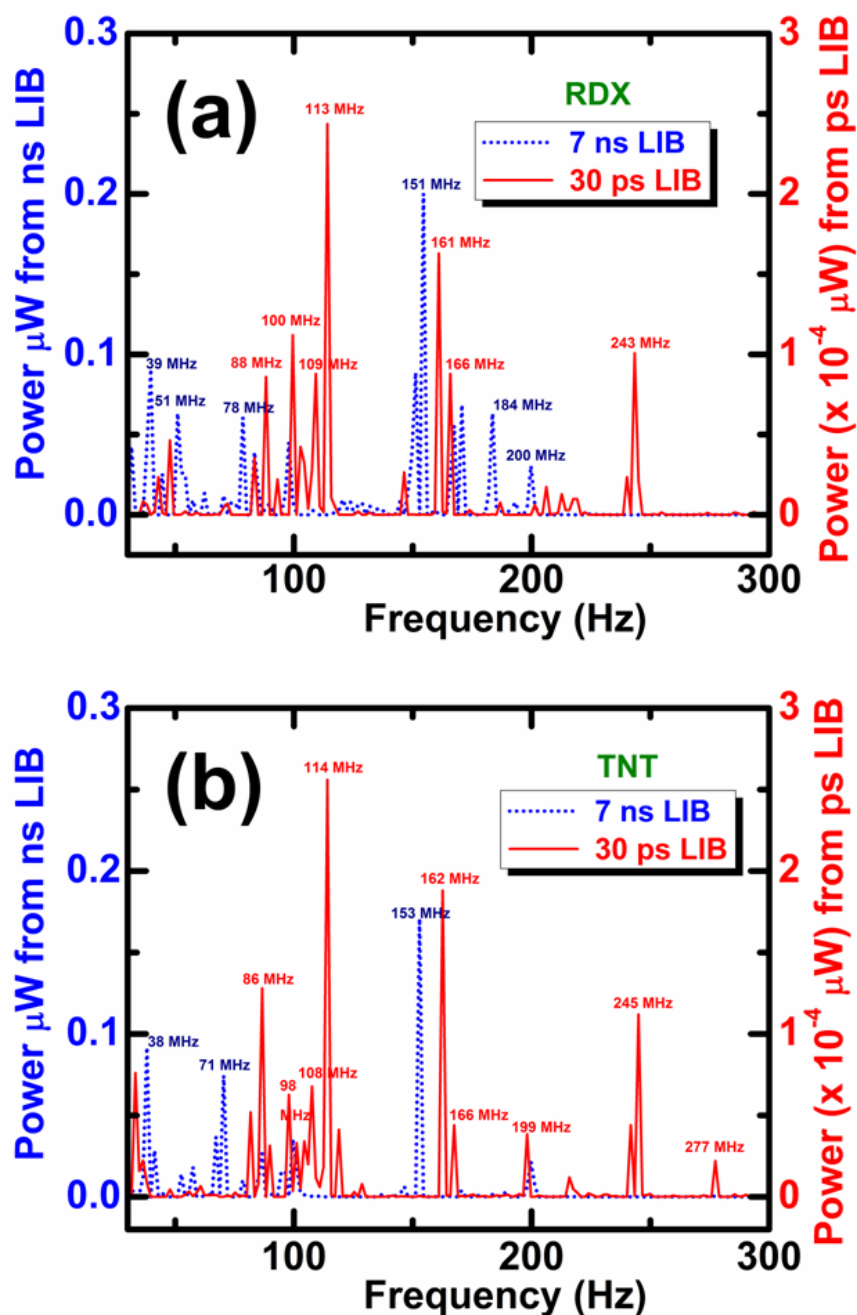


Fig 6.7: Comparison of RF emissions from ns LIB (at 40 mJ laser energy) and ps LIB (at 12 mJ laser energy) of (a) RDX and (b) TNT under similar laser and antenna polarization (V-pol antenna in ns LIB and H-pol antenna in ps LIB)

From Fig 6.7, it is observed that the prominent peaks from ns and ps LIB of a particular HEM are different. The maximum amplitude from the ns LIB of RDX and TNT were observed at 151 MHz and 153 MHz respectively. Also, the dominant peaks from the ps LIB of RDX and TNT were observed at 113 MHz and

114 MHz respectively. Both RDX and TNT, which contain carbon, hydrogen, oxygen and nitrogen, are polyatomic compounds. The breakdown of these polyatomic compounds, by pulsed lasers, will give rise to electrons and ions of all the species present in the compounds. Therefore, the probability of the cross interactions of the plasma constituents of different elements become very high. For example, the electron emitted by the nitrogen atom can interact with N^+ , O^+ , H^+ and C^+ ions in the plasma. Similarly, the electrons from the other atoms are equally probable to interact with these ions. Therefore, a large number of electric dipole interactions, with varying dipole moments (p) that affect the plasma frequency (ω_p), take place. It is these cross interactions that make the resulting RF spectrum richer with plenty of spectral lines. Between RDX and TNT, which have similar chemical compositions, the differences in the emissions were observed because of the difference in the interaction of the ns and ps pulses with the target [123, 124]. Because of the difference in the peak intensities between ns and ps pulses, the plasma parameters like electron density (n_e) and plasma temperature (T_e) will be different in these cases [124]. The plasma frequency ' ω_p ' in case of ps LIB, due to higher value of ' n_e ', will be higher than that with ns pulses. Thus, the difference in the dipolar oscillations in ns LIB and ps LIB tends to give different frequencies from ns and ps LIB. Because of this excessive ionization, the interaction between the charged particles and the neutrals come down in ps LIB. Thus, the RF emissions are observed to be almost three orders lesser in case of ps LIB when compared to that from ns LIB. These basic differences in the ns and ps material interaction lead to create plasmas of different characteristics which result in the difference in RF emissions.

In summary, the results on RF emissions from the ns and ps LIB of high energy materials (HEMs) are presented in this chapter. The studies on RF emissions from the ns and ps LIB of HEMs seem to be promising in differentiating compounds that have nitrogen and that are nitrogen free. The emissions are observed to match with the ion plasma frequencies (ω_{pi}) which confirms the significance of nitrogen in the RF emissions. Thus, the detection of explosives from the RF emissions from LIB seems to be very much possible. However, identification of HEMs from RF emissions has a long way to go. In order to build a database for the detection of HEMs, decent quantities of various HEMs are required. The time

Chapter 6: RF emissions from LIB of HEMs

evolution of the prominent lines, from ns (~155 MHz) and ps LIB (~165 MHz and ~250 MHz) LIB of the HEMs might give a better insight and lead to a technique to identify different high energy molecule. The RF emissions from ns and ps LIB of a particular HEM target confirms that the laser-matter interaction and the associated plasma parameters vary with respect to pulse duration. Thus, the RF emissions and their amplitudes were observed to be different in case of ns and ps LIB of HEMs.

Chapter VII

Summary and future scope

This chapter summarizes the work carried so far, followed by the future scope of the thesis.

The material specific RF emissions from LIB were encouraging to move towards the development of a wireless RF based sensor. The generation of RF emissions at lower input energies and the longer propagation of RF emissions from low energy LIB are some of the desirable factors of remote sample identification technique. The application of analysis techniques like principle component analysis (PCA), k-nearest neighbor (KNN), soft modeling class analogy (SIMCA), discriminant partial least squares(PLS-DA),mean-center analysis (MCA) etc. might enhance the capability in the extraction of analytical information from the emitted RF signals. Besides, time evolution of the spectral lines from HEMs will be important to proceed further in distinguishing them. The on-field detection and analysis of RF emissions from the reaction of an HEM will help us to understand the reliability in the lab studies of the RF emissions from LIB of HEMs. The studies on the possibilities of emissions at higher frequencies with femtosecond lasers will be crucial to arrive at standoff distances that are greater than those achievable with ns and ps laser pulses. In addition to the standoff sample identification, from the results on the LIB of copper powder compacts, the RF emissions from LIB can be developed as a tool for in situ monitoring of densification and the evaluation of the corresponding sample microstructure during any laser based sintering and welding of materials.

7.1 Summary

The phenomena of laser induced breakdown (LIB) and the plasma parameters determine the energy release during plasma expansion. The studies on these emissions (electromagnetic, mechanical, thermal etc.) will be important in understanding the material properties in the excited state. The radio frequency (RF) and microwave emissions from LIB are relatively less explored. The signature emissions, travelling towards the detector over the distance of several light years, reported from the astronomical sources [38-62] encourage the development of a remote sensing tool using radio waves. LIB of materials were reported to be a sophisticated way to generate RF radiation which are proposed to be utilized for laser ground penetrating radar (LGPR) application [99, 100]. Hence, systematic study of RF emissions over 30-1000 MHz region from the LIB of various materials by tuning the laser and target parameters were carried out. The results suggest that the RF emissions from LIB of materials can be a potential tool for standoff sample identification that can have plenty of advantages over the conventional techniques.

7.1.1. Optimization of conditions for maximum RF reception from LIB

After the calibration of the diagnostics with known RF sources and the experiments to improve the signal to noise ratio, the optimization of the experimental conditions were carried out. The studies on radial and angular distribution of RF emissions from LIB of atmospheric air and solid target indicate $\sin^2\theta/r^2$ dependence of electric dipolar radiation (Fig 7.1). From the RF emissions from ns and ps LIB of atmospheric air, it is understood that the interaction of charged particles with the cluster of atoms and molecules results in the emission of low frequency electromagnetic radiation from LIB [121]. The high peak power of ps laser, when compared with ns laser, ensures more ionization [124]. Hence the probability of interaction between the charged particles with neutrals is reduced in ps LIB. Thus, the emissions from ns LIB is found to be about 3 orders higher than those from ps LIB [123]. Also, at higher input laser energies, due to the faster recombination rates, the plasma decays soon. It was observed that the signal reception was better when the laser and the antenna polarization match (Fig 7.1a and 7.1b). Besides, the strength of the signals achieved at lower energies was

observed to be higher even at distances away from the plasma source. At a distance 190 cm away from the plasma, the amplitude of RF emissions from ns LIB at 40 mJ is observed to be ~ 1.8 times greater than that at 55 mJ input laser energy (Fig 7.1c). Similarly, in case of ps LIB, at 300 cm away from the source, the amplitude of emissions at 4 mJ is observed to be ~ 5 times higher than that at 16 mJ laser energy (Fig 7.1d). These are some of the attractive features that support RF emissions from LIB to be utilized for remote sensing.

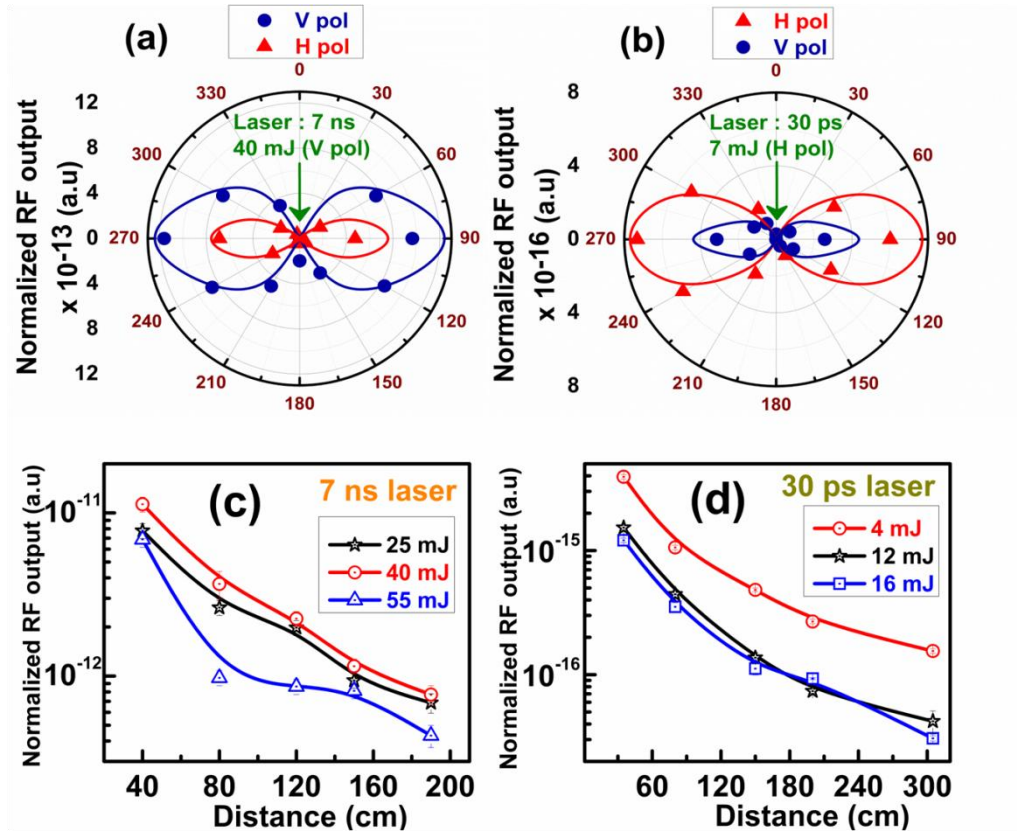


Fig 7.1: Angular and spatial distribution of RF emissions from ns and ps LIB of atmospheric air

The focusing conditions are found to play an important role in the generation of seed electrons and the subsequent RF emissions. The variation of RF emissions with $I\lambda^2$, under different focal geometries, emphasizes the importance of the plasma parameters and the interaction of the plasma constituents in the focal volume, in the RF emissions from LIB. The RF emissions were observed to scale with $I\lambda^2$ similar to that of hot electron temperature and the ablative pressure with intensity [131, 132]. The slope of the rise in RF emissions from ns and ps LIB represents the buildup of induced dipole moment with the input laser intensity. Similarly, the slope of the fall in the emissions, with respect to $I\lambda^2$, indicates the

damping of radiation that takes place at high input laser intensities. The optimal window of $I\lambda^2$ (10^{10} - 10^{11} $Wcm^{-2}\mu m^2$), which gives rise to RF emissions of relatively higher strength, can be generated by choosing the appropriate focusing conditions of ns and ps laser pulses for standoff explosive detection techniques.

7.1.2. Material specific RF emissions from LIB

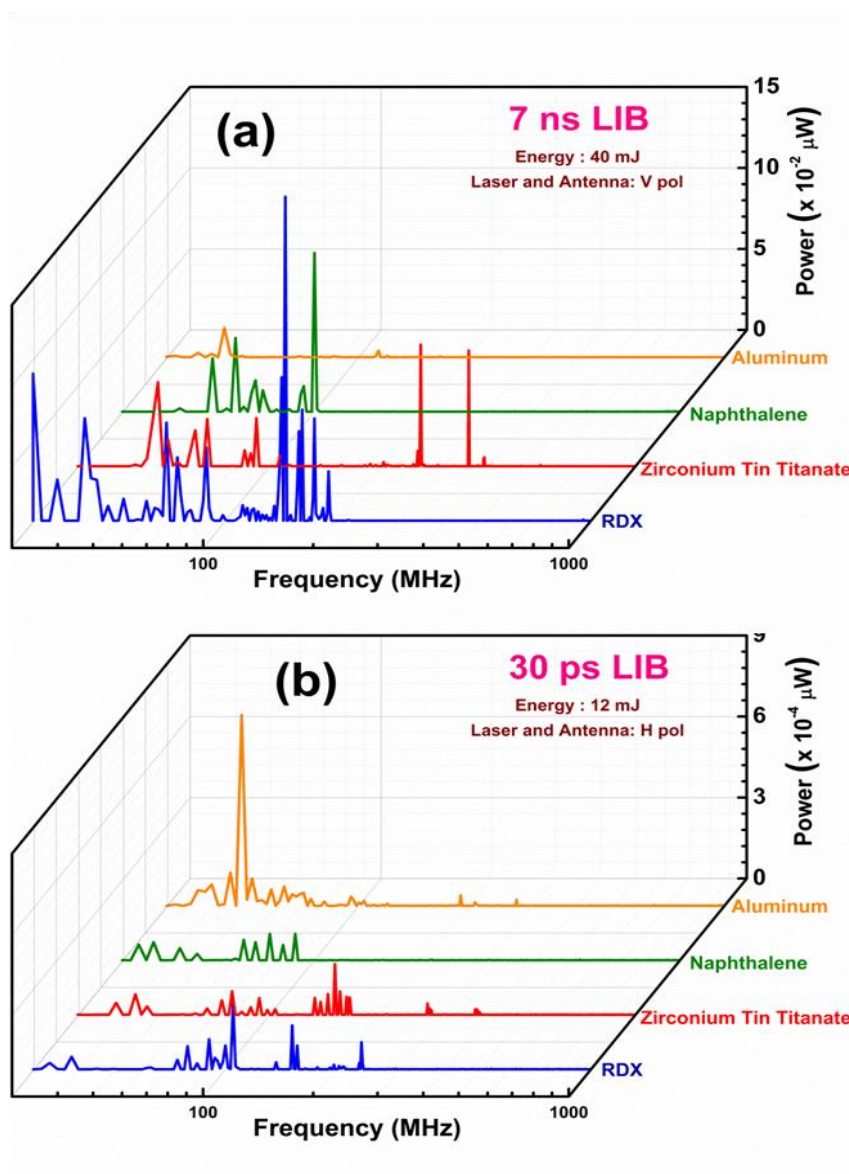


Fig 7.2: Spectral selective RF emissions from (a) ns and (b) ps LIB

After the optimization of the experimental conditions, to understand the significance of the properties of the target material (electrical conductivity ' σ ', material density ' ρ ', surface properties etc.) in the plasma formation and the associated RF emissions from LIB, the experiments were carried out with targets

Chapter 7: Summary and future scope

of variety of material classes: conductors (copper, aluminum, SS304 and brass), insulators (alumina, Teflon, PVC and naphthalene), dielectrics (borosilicate glass, Mica, BaTiO₃, ZrSnTiO₃ and LiNbO₃), compacts of micron sized copper powders (of different particle sizes and packing densities) and HEMs (RDX, PETN, TNT, NTO, CL20, NaN₃ and Pyrazoles). The emissions depend on the laser and material parameters and correspond to the ion-plasma frequencies (ω_{pi}) that are tabulated in 7.1 and 7.2.

Table 7.1: Estimated ion plasma frequencies (ω_{pi}): ns LIB of targets

Target	Laser intensity range (W/cm ²)	Electron density (n_e) range (cm ⁻³)	Estimated ion plasma frequency values (MHz)	
			Atomic species	Molecular species
Conductors	$3 \times 10^{10} - 7 \times 10^{10}$	$1 \times 10^{17} - 3 \times 10^{17}$	Cu ⁺ : 141,185 Al ⁺ : 260 Fe ⁺ : 235 Cr ⁺ : 243 Ni ⁺ : 229 Mn ⁺ : 236 C ⁺ : 325 Zn ⁺ : 139	(Fe ₂ O ₃) ⁺ : 110 (CuO ₂) ⁺ : 94, 150 (Mn ₃ O ₄) ⁺ : 110 (CuO) ⁺ : 131
Insulators	$1 \times 10^{10} - 8 \times 10^{10}$	$1 \times 10^{16} - 4 \times 10^{16}$	Al ⁺ : 103 O ⁺ : 133 C ⁺ : 107, 133, 190 H ⁺ : 376, 671 Cl ⁺ : 110 F ⁺ : 105	(Al ₂ O ₃) ⁺ : 53 (C ₁₀ H ₈) ⁺ : 39 (C ₂ H ₃ Cl) ⁺ : 83 (C ₂ F ₄) ⁺ : 46 (C ₂) ⁺ : 75, 94, 134 (H ₂) ⁺ : 258, 460 (O ₂) ⁺ : 95 (F ₂) ⁺ : 75
Dielectrics	$9 \times 10^9 - 6 \times 10^{10}$	$2 \times 10^{16} - 9 \times 10^{16}$	B ⁺ : 140 Si ⁺ : 87, 171 O ⁺ : 115, 171, 242, 254, 263 Al ⁺ : 164 K ⁺ : 108 Na ⁺ : 188 Mg ⁺ : 184 F ⁺ : 197 Li ⁺ : 261 Nb ⁺ : 71 Ba ⁺ : 87 Ti ⁺ : 146, 151 Zr ⁺ : 106 Sn ⁺ : 95	(BaTiO ₃) ⁺ : 66 (LiNbO ₄) ⁺ : 64 (ZrSnTiO ₃) ⁺ : 60 (O ₂) ⁺ : 121, 180, 185
HEMs	$\sim 2 \times 10^{10}$	$2.5 \times 10^{16} - 2.6 \times 10^{16}$	C ⁺ : 162-164 O ⁺ : 140-143 N ⁺ : 150-152 H ⁺ : 571-577	(C ₃ H ₆ N ₆ O ₆) ⁺ : 38 (C ₅ H ₈ N ₄ O ₃) ⁺ : 32 (C ₂ H ₂ N ₄ O ₃) ⁺ : 58 (C ₇ H ₅ N ₃ O ₆) ⁺ : 38 (C ₃ H ₄ N ₂) ⁺ : 68 (C ₃ H ₃ N ₃ O ₂) ⁺ : 53 (C ₂) ⁺ : 115-119 (H ₂) ⁺ : 393-399 (O ₂) ⁺ : 99-102 (N ₂) ⁺ : 106-113

Table 7.2: Estimated ion plasma frequencies (ω_{pi}): ps LIB of targets

Target	Laser intensity range (W/cm ²)	Electron density (n_e) range (cm ⁻³)	Estimated ion plasma frequency range (MHz)	
			Atomic species	Molecular species
Conductors	$6 \times 10^{12} - 9 \times 10^{12}$	$4 \times 10^{19} - 9 \times 10^{21}$	Cu ⁺ : 4146, 4420 Al ⁺ : 16180 Fe ⁺ : 2870 Cr ⁺ : 2970 Ni ⁺ : 2797 Mn ⁺ : 2890 C ⁺ : 9547 Zn ⁺ : 4087	(Fe ₃ O ₄) ⁺ : 612 (Fe ₂ O ₃) ⁺ : 737, 885 (Cu ₂ O) ⁺ : 779, 833 (Mn ₃ O ₄) ⁺ : 616 (Mn ₂ O ₃) ⁺ : 742 (Ni ₂ O ₃) ⁺ : 725
Insulators	$5 \times 10^{12} - 8 \times 10^{12}$	$6 \times 10^{17} - 6 \times 10^{18}$	Al ⁺ : 1689 O ⁺ : 2192 C ⁺ : 755, 821, 852 H ⁺ : 2894, 2662 Cl ⁺ : 836 F ⁺ : 677	(Al ₂ O ₃) ⁺ : 868 (C ₁₀ H ₈) ⁺ : 231 (C ₂ H ₃ Cl) ⁺ : 359 (C ₂ F ₄) ⁺ : 295 (C ₂) ⁺ : 533, 579, 601, (H ₂) ⁺ : 1826, 1985 (O ₂) ⁺ : 1551 (F ₂) ⁺ : 479
Dielectrics	$6 \times 10^{12} - 8 \times 10^{12}$	$9 \times 10^{17} - 1 \times 10^{18}$	O ⁺ : 826, 880 Li ⁺ : 1254 Nb ⁺ : 343 Ba ⁺ : 301 Ti ⁺ : 509 Zr ⁺ : 369 Sn ⁺ : 280	(BaTiO ₃) ⁺ : 231 (LiNbO ₄) ⁺ : 272 (ZrSnTiO ₃) ⁺ : 165 (O ₂) ⁺ : 584, 623
HEMs	$\sim 9 \times 10^{11}$	$4.8 \times 10^{17} - 5 \times 10^{17}$	C ⁺ : 705-707 O ⁺ : 608-612 N ⁺ : 652-655 H ⁺ : 2487-2489	(C ₃ H ₆ N ₆ O ₆) ⁺ : 163 (C ₆ H ₁₂ N ₆ O ₁₂) ⁺ : 163 (C ₇ H ₅ N ₃ O ₆) ⁺ : 164 (NaN ₃) ⁺ : 162 (C ₂) ⁺ : 498-502 (H ₂) ⁺ : 1706-1710 (O ₂) ⁺ : 432-435 (N ₂) ⁺ : 461-465

Hence, the dominant emissions from the LIB of the targets studied fall in different specific spectral bands. The distinctive band of emissions from ns and ps LIB of the studied HEMs indicates the importance of the presence of nitrogen (Fig 7.2). Therefore, the RF emissions from the LIB of different materials can be developed as a tool for remote identification of samples besides detection.

7.1.3. Separation of material classes from the strength of RF emissions

At very low input laser energies, the materials of same electrical properties were observed to be grouped with respect to the RF emissions. The separation of different classes of materials, due to the RF emissions from ns and ps LIB, is shown in Fig 7.3.

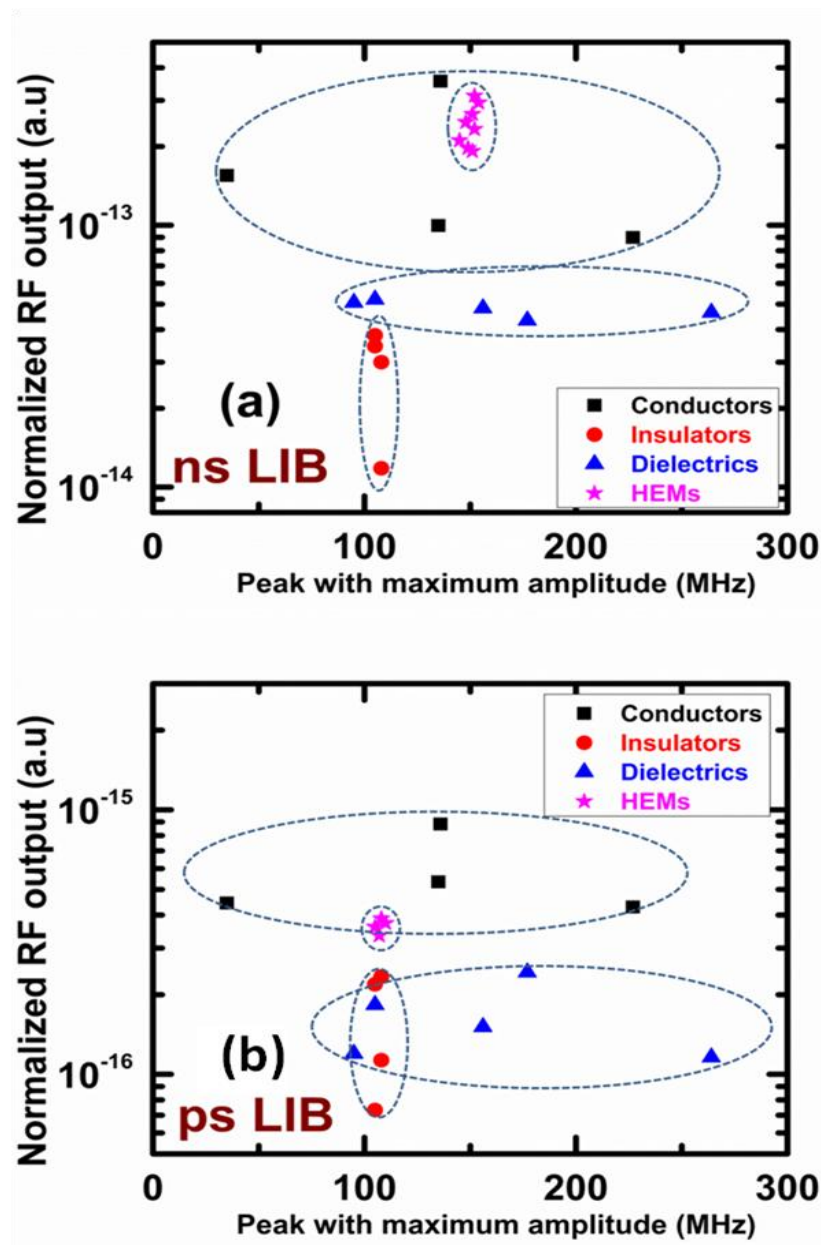


Fig 7.3: Separation of material classes by the strength of the RF emissions from ns and ps LIB

The amplitude of RF emissions from conducting samples, at low laser energies, was observed to be relatively higher than the other classes. This is because of the relatively lower ionization potential of metallic samples which, during laser-matter interaction, yield sufficient electrons that contribute to the plasma. Thus, the charge-neutral interaction and the subsequent emissions from the LIB of conductors are relatively higher. As a result, the RF emissions at low input laser energies separate out metals from non metals. At higher input laser energies, the intense ionization of the metallic targets leaves out very few neutral atoms/molecules in tact that results in the reduction of electron-neutral interaction

Chapter 7: Summary and future scope

and the subsequent RF emissions. In targets other than metals, the emissions become higher at energies higher than that in case of metals. The amplitude of the emissions from ns (at 40 mJ) and ps (at 12 mJ) LIB of HEMs was observed to fall closer to that of the RF emissions from the conducting samples. Therefore, the separation of material categories does not take place at higher input laser energies.

7.1.4. Dependence of input laser energy on RF emissions from LIB

As in the case of atmospheric air, the emissions from solids at high input laser energies were observed to be falling down. At higher laser energies, the increased value of plasma density (n_e), will result in the increase in the recombination rate of the plasma. As a result of this the plasma decays relatively sooner and hence the RF emissions come down. In case of ps LIB, the plasma frequency (ω_p) was observed to approach the laser frequency (ω_L) leading to higher reflectance of incoming laser pulse from the plasma [148]. At high input laser energies, this ratio of plasma frequency (ω_p) to the laser frequency (ω_L), from the ps LIB of some targets, was observed to be approaching unity. Hence, at high input energies, the laser-plasma interaction is considerably reduced which brings down the RF emissions. These were experimentally confirmed from the calculation of plasma frequencies (ω_p) from electron densities (n_e) of LIB of some of the targets.

7.1.5. Dependence of target surface on RF emissions from LIB

The results with micron sized copper compacts suggest that the laser matter interaction is different for targets with different particle size and packing density. The generation of seed electrons and the subsequent avalanche breakdown requires very low laser energies in case of targets with finer particles and high packing densities. When compared with the bulk-sintered sample, the emissions from the compacted micron powders were observed to be higher and lower at low and high input laser energies respectively. This is due to the difference in the surface properties of these samples. The compacted powders, due to their surface roughness, absorb most of the input laser radiation compared to the bulk-sintered sample which, due to its highly polished surfaces, reflects away most of the incident input radiation. Thus, the RF emissions can be manipulated by tuning the surface properties of the target materials. Further studies in this line can pave way for the development of a wireless remote sample identification technique.

7.2 Future scope

The principal component analysis (PCA) technique was applied to a set of LIBS spectra to highlight the variation and bring out the signature patterns in a dataset more clearly [35]. Similar studies with a number of RF spectra from the LIB, under similar experimental conditions, will bring out more clarity in the spectral signatures. Similarly, application of analysis techniques like k-nearest neighbor (KNN), soft modeling class analogy (SIMCA), discriminant partial least squares (PLS-DA), mean-center analysis (MCA) etc. [177] can help in deriving out the analytical information from the RF emissions from LIB making these emissions augment the traditional LIBS technique.

The initial results on the RF emissions from LIB of HEMs shows the need of further studies to distinguish different HEM molecules from the observed RF bands. The most dominant emissions from the ns and ps LIB of all the HEMs were observed to fall under particular bands of frequencies. The time resolved studies of these frequency lines, to understand their evolution with time, have to be carried out to get a better picture of the plasma dynamics in the laser-HEM interaction.

Laser ablation of HEMs, which is the small scale replication of a reacting HEM, was carried out to study the emissions from the LIB of HEM samples. The real field measurement of RF emissions from the reacting HEM molecules will be crucial to check the reliability of the studies on the emissions from LIB.

The experiments carried out were to compare the emission of frequencies from laser induced breakdown of targets with laser pulses that have similar plasma dynamics. Laser pulses of pulse duration < 1 ps fall in the ultrashort category where multiphoton ionization is the major plasma formation mechanism and hence, the equation or breakdown threshold (equation 3.4) is not valid in this case. Therefore in order to draw out the effect of pulse duration, 7 ns and 30 ps pulses with which avalanche breakdown is the plasma formation mechanism were used in our studies. The RF emissions from the LIB of copper powder compacts (chapter 5) show that the plasma evolution under both 7 ns and 30 ps LIB at high input intensities is independent of the surface properties of the target. When laser ablation is carried out with ultrashort pulses, the surface property of the target in

Chapter 7: Summary and future scope

the plasma evolution plays a major role. Therefore, from our studies, it is evident that both 7ns and 30 ps pulses are too long to be fit into the ultrafast domain. Thus, only low frequency emissions (30-1000 MHz) were detected from the ns and ps LIB of different targets. There was hardly any signal detection, of appreciable strength, in the higher frequencies. With ultrafast laser ablation of the targets, the conditions favourable for the generation of higher frequencies (> 1 GHz) may be induced. Therefore, our future plan is to carry out the studies on the possibility of emissions from LIB of materials with femtosecond (fs) pulses and fs filamentation [178] for standoff distances that are greater than achievable with ns and ps laser pulses.

The studies on RF emissions from the copper powder compacts revealed a variation in the RF emissions with respect to particle size and packing density. These results suggest that the RF emissions from LIB can be developed as a tool for in situ monitoring of densification and the evaluation of the corresponding sample microstructure during any laser based sintering and welding of materials [172].

References

- [1] P. Gibbon, "Short Pulse Laser Interactions with Matter: An introduction," *Imperial College Press* (2005).
- [2] J. S. Bakos, "Laser Plasmas '89," *Prog. Quant. Electr.* **14**, 251-288 (1990).
- [3] P. Mulser, R. Sigel and S. Witkowski, "Plasma production by laser," *Phys. Reports.* **6** (3), 187-239 (1973).
- [4] M. S. Brown and C. B. Arnold, "Fundamentals of laser-material interaction and application to multiscale surface modification," *Springer Ser. Mater. Sci.* 91-120 (2010).
- [5] R. W. Boyd, "Nonlinear Optics," Third edition, *Acad. Press* (2003).
- [6] Y. R. Shen, "Principles of Nonlinear Optics," *Wiley* (2002).
- [7] S. Conesa, S. Palanco, and J.J. Laserna, "Acoustic and optical emission during laser-induced plasma formation," *Spectrochim. Acta Part B At. Spectrosc.* **59**, 1395-1401 (2004).
- [8] E. Manikanta, L. Vinoth Kumar, P. Venkateshwarlu, and P. Prem Kiran, "Acoustic shockwave emissions from ns and ps pulsed laser induced breakdown of air," *Tech. Lett.* **10**, 16-19 (2014).
- [9] E. Manikanta, L. Vinoth Kumar, Ch. Leela, and P. Prem Kiran, "Effect of pulse duration on the acoustic frequency emissions during laser induced breakdown of atmospheric air," (under review).
- [10] Ch. Leela, S. Bagchi, V. R. Kumar, S. P. Tewari, and P. P. Kiran, "Dynamics of laser induced micro-shock waves and hot core plasma in quiescent air," *Laser part beams* **31**, 263 (2013).
- [11] Ch. Leela, P. Venkateshwarlu, R. V. Singh, P. Verma and P. Prem Kiran, "Spatio-temporal dynamics behind the shock front from compacted nanopowders," *Opt. Express* **22**, No. S2 (2014).
- [12] A. Zigler, H. Zmora and J.L. Schwob, "The origin of $K\alpha$ radiation in laser-produced aluminum plasma," *Phys. Lett. A.* **63**, 275-278 (1977).
- [13] A. Z. Giovannini and R. S. Abhari, "Three-dimensional extreme ultraviolet emission from a droplet-based laser-produced plasma," *J. Appl. Phys.* **114**, 033303 1-8 (2013).
- [14] J. P. Singh and S. N. Thakur, "Laser-induced breakdown spectroscopy," *Elsevier Science* (2007).
- [15] E. A. Ershov-Pavlov, K. Yu. Katsalap, K. L. Stepanov, and Yu. A. Stankevich, "Time-space distribution of laser-induced plasma parameters and its influence on emission spectra of the laser plumes," *Acta Part B At. Spectrosc.* **63**, 1024-1037 (2008).
- [16] I. B. Gornushkin, A. Ya. Kazakov, N. Omenetto, B. W. Smith, and J. D. Winefordner, "Radiation dynamics of post-breakdown laser induced plasma," *Spectrochim. Acta Part B* **59**, 401-418 (2004).

References

- [17] D. A. Cremers, and L. J. Radziemski, "Handbook of Laser-Induced Breakdown Spectroscopy," *John Wiley & Sons, Ltd.* (2006).
- [18] L. Radziemski and D. Cremers, "A brief history of laser-induced breakdown spectroscopy: from the concept of atoms to LIBS 2012," *Spectrochimica. Acta B.* **87**, 3-10 (2013).
- [19] W. D. Duncan and G. P. Williams, "Infrared synchrotron radiation from electron storage rings," *Appl. Opt.* **22**(18), 2914-2923 (1983).
- [20] H. S. Dunn and M. J. Lubin, "Electromagnetic radiation from a laser produced plasma expanding into a uniform magnetic field," *J. Plasma Phys.* **4**, 573-583 (2009).
- [21] S. Tzortzakis, G. Méchain, G. Patalano, Y. B. André, B. Prade, M. Franco, and A. Mysyrowicz, "Coherent subterahertz radiation from femtosecond infrared filaments in air," *Opt. Lett.* **27**(21), 1944-1946 (2002).
- [22] C. D'Amico, A. Houard, M. Franco, B. Prade, A. Mysyrowicz, A. Couairon and V. T. Tikhonchuk, "Conical Forward THz Emission from Femtosecond-Laser-Beam Filamentation in Air," *Phys. Rev. Lett.* **98**, 235002 1-4 (2007).
- [23] E. Budiarto, J. Margolies, S. Jeong, J. Son, and J. Bokor, "High-intensity terahertz pulses at 1 - kHz repetition rate," *IEEE J. Quantum Electron.* **32**(10), 1839-1846 (1996).
- [24] Y. Zhang, Y. Chen, C. Marceau, W. Liu, Z.-D Sun, S. Xu, F. Theberge, M. Châteauneuf, J. Dubois, and S. L. Chin, "Non-radially polarized THz pulse emitted from femtosecond laser filament in air," *Opt. Express* **16**(20), 15483-15488 (2008).
- [25] T. Nakazato, M. Oyamada, N. Niimura, S. Urasawa, O. Konno, A. Kagaya, R. Kato, T. Kamiyama, and Y. Torizuka, "Observation of coherent synchrotron radiation," *Phys. Rev. Lett.* **63**(12), 1245-1248 (1989).
- [26] D. Dietze, J. Darmo, S. Roither, A. Pugzlys, J.N. Heyman, and K. Unterrainer, "Polarization of terahertz radiation from laser generated plasma filaments," *J. Opt. Soc. Am. B.* **26**(11), 2016-2027 (2009).
- [27] X. Lu, N. Karpowicz, Y. Chen, and X. C. Zhang, "Systematic study of broadband terahertz gas sensor," *App. Phys. Lett.* **93**, 261106 (2008).
- [28] H. Zhong, N. Karpowicz, and X. C. Zhang, "Terahertz emission profile from laser-induced air plasma," *App. Phys. Lett.* **88**, 261103 (2006).
- [29] I. Babushkin, S. Skupin, and J. Herrmann, "Generation of terahertz radiation from ionizing two-color laser pulses in Ar filled metallic hollow waveguides," *Opt. Express* **18**(9), 9658-9663 (2010).
- [30] Z. Y. Chen, J. F. Li, J. Li and Q. X. Peng, "Microwave radiation mechanism in a pulse-laser-irradiated Cu foil target revisited," *Phys. Scr.* **83**, 055503 1-4 (2011).
- [31] F. Curtis Michel, "Intense Coherent Submillimeter Radiation in Electron Storage Rings," *Phys. Rev. Lett.* **48**(9), 580-583 (1982).
- [32] J. Dai, X. Xie, and X.-C. Zhang, "Detection of broadband terahertz waves with a laser-induced plasma in gases," *Phys. Rev. Lett.* **97**, 103903 (2006).

References

- [33] J. M. Dai, X. F. Lu, J. Liu, I. C. Ho, N. Karpowicz and X. Zhang, "Remote THz Wave Sensing in Ambient Atmosphere," *THz Sci. Tech.* **2**, 131-143 (2009).
- [34] A. P. M. Michel, "Review: Applications of single-shot laser-induced breakdown spectroscopy," *Spectrochimica. Acta B.* **65**, 185-191 (2010).
- [35] M. Ashwin Kumar, N. Spegazzini, C. Zhang, A. Siva Kumar, Ramachandra R. Dasari, I. Barman and G. Manoj Kumar, "Less is more: Avoiding the LIBS dimensionality curse through judicious feature selection for explosive detection," *Sci. Reports* **5**, 13169 (2015).
- [36] S. Fujioka, H. Nishimura, H. Takabe, N. Yamamoto, K. Nishihara, D. Salzmann, T. Norimatsi, N. Miyanaga, K. Mima, H. Azechi, A. Sunahara, Y. Shimada, Y. Izawa, K. Nagai, F. Wang, J. Zhong, G. Zhao, Y. Li, Q. Dong, S. Wang, Y. Zhang, J. Zhang, Y. J. Rhee, Y. W. Lee and D. H. Kwon, "Laser-produced plasmas as unique x-ray sources for industry and astrophysics," *J. Phys. Conf. Ser.* **244**, 012001 1-7 (2010).
- [37] C. A. Balanis, "Antenna theory, analysis and design," Third Edition, Wiley (2005).
- [38] F. Yusef-Zadeh, M. Wardle, D. Lis, S. Viti, C. Brogan, E. Chambers, M. Pound and M. Rickert, "74 MHz nonthermal emission from molecular clouds: evidence for a cosmic ray dominated region at the galactic center," *J. Phys. Chem. A.* **117**, 9404-9419 (2013).
- [39] Y. Sato, T. Ono, M. Iizima, A. Kumamoto, N. Sato, A. Kadokura and H. Miyaoka, "Auroral radio emission and absorption of medium frequency radio waves observed in Iceland," *Earth Planets Space* **60**, 207-217 (2008).
- [40] W. Sun and J. Wu, "Calculation of RF emission brightness temperature of high density plasmas clouds in Sun-terrestrial interplanetary space," *ILWS workshop 2006, Goa*, 107-110 (2006).
- [41] M. Abada-Simon, "Comparison of the observational data on flare stars, solar and planetary radio emissions," *Planet Space Sci.* **44**(5), 501-507 (1996).
- [42] W. S. Kurth, D. A. Gurnett, F. L. Scarf and R. L. Poynter, "Detection of a radio emission at 3 kHz in the outer heliosphere," *Nature* **312**, 27-31 (1984).
- [43] Bo. Thide, "Observations of stimulated scattering of a strong high-frequency radio wave in the ionosphere," *Phys. Rev. Lett.* **49**(21), 1561-1564 (1982).
- [44] B. Cecconi, S. Hess, A. Hérisque, M. R. Santovito, D. Santos-Costa, P. Zarka, G. Alberti, D. Blankenship, J. -L. Bougeret, L. Bruzzone, W. Kofman, "Natural radio emission of Jupiter as interferences for radar investigations of the icy satellites of Jupiter," *Planet. Space Sci.* **61**(1), 32-45 (2012).
- [45] P. Zarka, "Plasma interactions of exoplanets with their parent star and associated radio emissions," *Planet. Space Sci.* **55**(5), 598-617 (2007).

References

- [46] K. Beuermann, G. Kanbach and E. M. Berkhuijsen, "Radio structure of the galaxy: thick disk and thin disk at 408 MHz," *Astron. Astrophys.* **153**, 17-34 (1985).
- [47] R. T. Newell and R. M. Hjellming, "Radio emission from the extended chromosphere of alpha orionis," *Astrophys. J.* **263**, 85-87 (1982).
- [48] G. A. Dulk, "Radio emission from the sun and stars," *Ann. Rev. Astron. Astrophys.* **23**, 169-224 (1985).
- [49] W. M. Neupert, "Comparison of solar X-ray line emission with microwave emission during flares," *Astrophys. J.* **153**, 59-64 (1968).
- [50] T. S. Bastian, A. O. Benz and D. E. Gary, "Radio emission from solar flares," *Annu. Rev. Astron. Astrophys.* **36**, 131-188 (1998).
- [51] S. Buitink, W. D. Apel, T. Asch, F. Badea, L. Bähren, K. Bekk, A. Bercuci, M. Bertaina, P. L. Biermann, J. Blümer, H. Bozdog, I. M. Brancus, M. Brüggemann, P. Buchholz, H. Butcher, A. Chiavassa, F. Cossavella, K. Daumiller, F. Di Piero, P. Doll, R. Engel, H. Falcke, H. Gemmeke, P. L. Ghia, R. Glasstetter, C. Grupen, A. Haungs, D. Heck, J. R. Hörande, A. Horneffer, T. Huege, K.-H. Kampert, Y. Kolotaev, O. Krömer, J. Kuijpers, S. Lafebre, H. J. Mathes, H. J. Mayer, C. Meurer, J. Milke, B. Mitrica, C. Morello, G. Navarra, S. Nehls, A. Nigl, R. Obenland, J. Oehlschläger, S. Ostapchenko, S. Over, M. Petcu, J. Petrovic, T. Pierog, S. Plewnia, H. Rebe, A. Risse, M. Roth, H. Schieler, O. Sima, K. Singh, M. Stümpert, G. Toma, G. C. Trinchero, H. Ulrich, J. Van Buren, W. Walkowiak, A. Weindl, J. Wochele, J. Zabierowski, J. A. Zensus, and D. Zimmermann, "Amplified radio emission from cosmic ray air showers in thunderstorms," *Astron. Astrophys.* **467**(2), 385-394 (2007).
- [52] N. O. Renno, A. San Wong, and S.K. Atreya, "Electrical discharges and broadband radio emission by Martian dust devils and dust storms," *Geophys. Re. Lett.* **30**(22), 2140 (2003).
- [53] I. Al Samarai, O. Deligny, D. Lebrun, A. Letessier-Selvon, F. Salamida, "An estimate of the spectral intensity expected from the molecular Bremsstrahlung radiation in extensive air showers," *Astropart. Phys.* **67**, 26-32 (2015).
- [54] A. V. Gurevich, L. M. Duncan, Yu. V. Medvedev and K. P. Zybin, "Radio emission due to simultaneous effect of runaway breakdown and extensive atmospheric showers," *Phys. Lett. A* **301**(3-4), 320-326 (2002).
- [55] H. Falcke and P. Gorham, "Detecting radio emission from cosmic ray air showers and neutrinos with a digital radio telescope," *Astropart. Phys.* **19**, 477-494 (2003).
- [56] J. LaBelle, G. Wyman, "Spontaneous radio frequency emissions from natural aurora in Characterising the Ionosphere," *Technical Report RTO-TR-IST-051*, Chapter 4, 1-22 (2009).
- [57] J. Colvin and J. Larsen, "Extreme Physics: Properties and Behavior of Matter at Extreme Conditions," *Cambridge university press* (2014).

References

- [58] N. Sakai, T. Shiino, T. Hirota, T. Sakai, and S. Yamamoto, "Long carbon-chain molecules and their anions in the starless core, lupus-1A," *Astrophys. J. Lett.* **718**, 49-52 (2010).
- [59] W. B. Somerville, "Interstellar radio spectrum lines," *Rep. Prog. Phys.* **40**(5), 483-565 (1977).
- [60] L. E. Snyder and D. Buhl, "Observations of radio emission from interstellar hydrogen cyanide," *Astrophys. J.* **163**, 47-52 (1971).
- [61] S. D. Bale, "Observation of topside ionospheric MF/HF radio emission from space," *Geophys. Res. Lett.* **26**(6), 667-670 (1999).
- [62] W. R. Barron, E. W. Cliver, J. P. Cronin and D. A. Guidice, "Solar radio emission," in Handbook of Geophysics and the Space Environment, ed. A. S. Jura, AFGL, USAF Chap.11 (1985).
- [63] T. Takano, H. Ikeda, and T. Maeda, "Consideration of the mechanism of microwave emission due to material destruction," *J. App. Phys.* **108**, 83722 (2010).
- [64] K. Maki, E. Soma, T. Takano, A. Fujiwara, and A. Yamori, "Dependence of microwave emissions from hypervelocity impacts on the target material," *J. App. Phys.* **97**, 104911 (2015).
- [65] T. Takano, Y. Murotani, K. Maki, T. Toda, A. Fujiwara, S. Hasegawa, A. Yamori, and H. Yano, "Microwave emission due to hypervelocity impacts and its correlation with mechanical destruction," *J. App. Phys.* **92**, 5550 (2002).
- [66] H. Ohnishi, S. Chiba, E. Soma, K. Ishii, K. Maki, T. Takano, and S. Hasegawa, "Study on microwave emission mechanisms on the basis of hypervelocity impact experiments on various target plates," *J. App. Phys.* **101**, 124901 (2007).
- [67] T. Johnson, I. Linscott, S. Close, D. Strauss, N. Lee, R. Adamo, A. Mocker, R. Srama, and S. Bugiel, "Detection and Analysis of RF Data from Hypervelocity Impacts," *3rd AIAA Atmospheric Space Environments Conference* (2011).
- [68] G. Joseph, "Fundamentals of remote sensing," Second Edition, *Universities press* (2005).
- [69] J. S. Pearlman and G. H. Dahlbacka, "Emission of rf radiation from laser-produced plasmas," *J. Appl. Phys.* **49**, 457-459 (1978).
- [70] G. Gerdin, M. J. Tanis and F. Venneri, "Observation of microwave emission from a plasma focus at frequencies well below mean plasma frequency," *Plasma Phys. Control. Fusion.* **28**, 527-545 (1986).
- [71] D. W. Forslund and P. D. Goldstone, "High energy plasma physics with CO₂ lasers," *Los Alamos Sci.* **12**, 2-27 (1985).
- [72] H. P. Schlenvoigt, K. Haupt, A. Debus, F. Budde, O. Jackel, S. Pfothenhauer, J. G. Gallacher, E. Brunetti, R. P. Shanks, S. M. Wiggins, D. A. Jaroszynski, E. Rohwer, and H. Schwoerer, "Synchrotron Radiation From Laser-Accelerated Monoenergetic Electrons," *IEEE Trans. Plasma Sci.* **36**(4), 1773-1781 (2008).

References

- [73] J. Miragliotta, J. Spicer, B. Brawley and S. Varma, "Enhancement of electromagnetic pulse emission from ultrashort laser pulse irradiated solid targets," *Proc SPIE*. **8381**, 83811N 1-7 (2012).
- [74] J.A. Aspiotis, N. Barbieri, R. Bernath, C.G. Brown, M. Richardson, and B.Y. Cooper, "Detection and analysis of RF emission generated by laser-matter interactions," *Proc. of SPIE* **6219**, 621908 (2006).
- [75] T. Matsuoka, S. Kneip, C. McGuffey, C. Palmer, J. Schreiber, C. Huntington, Y. Horovitz, F. Dollar, V. Chvykov, G. Kalintchenko, A. G. R. Thomas, V. Yanovsky, K. Ta Phuoc, S. P. D. Mangles, Z. Najmudin, A. Maksimchuk, and K. Krushelnick, "Synchrotron x-ray radiation from laser wakefield accelerated electron beams in a plasma channel," *J. Phys: Conf. Ser.* **244**, 042026 (2010).
- [76] A. Rousse, K. Ta Phuoc, R. Shah, A. Pukhov, E. Lefebvre, V. Malka, S. Kiselev, F. Burgy, J. P. Rousseau, D. Umstadter, and D. Hulin, "Production of a keV X-Ray Beam from Synchrotron Radiation in Relativistic Laser-Plasma Interaction," *Phys. Rev. Lett.* **93**(13), 135005 (2004).
- [77] H.-P. Schlenvoigt, K. Haupt, A. Debus, F. Budde, O. Ja'ckel, S. Pfoth, H. Schwoerer, E. Rohwer, J.G. Gallacher, E. Brunetti, R.P. Shanks, S. M. Wiggins and D. A. Jaroszynski, "A compact synchrotron radiation source driven by a laser-plasma wakefield accelerator," *Nat. Phys.* **4**, 130-133 (2008).
- [78] D.C. Eder, A. Throop, C.G. Brown, Jr., J. Kimbrough, M.L. Stowell, D. A. White, P. Song, N. Back, A. MacPhee, H. Chen, W. DeHope, Y. Ping, B. Maddox, J. Lister, G. Pratt, T. Ma, Y. Tsui, M. Perkins, D. O'Brien, and P. Patel, "Mitigation of electromagnetic pulse (EMP) effects from short-pulse lasers and fusion neutrons," Lawrence Livermore National Laboratory (LLNL), Livermore, CA (2009).
- [79] M. J. Mead, D. Neely, J. Gauoin, R. Heathcote, and P. Patel, "Electromagnetic pulse generation within a petawatt laser target chamber," *Rev. Sci. Instrum.* **75**, 4225 (2004).
- [80] L. Li, B. Li, S. Ishiguro, and M. Song, "Electromagnetic radiation at the electron plasma wave frequency by an intense laser pulse interacting with low-density plasmas," *J. Plasma Phys.* **72**(6), 1303-1307 (2006).
- [81] Z. M. Sheng, H. C. Wu, W. M. Wang, M. Chen, X. G. Dong, J. Zheng, and J. Zhang, "Simulation of high power THz emission from laser interaction with tenuous plasma and gas targets," *Commun. Comput. Phys.* **4**(5), 1258-1278 (2008).
- [82] W.-M. Wang, Z.-M. Sheng, H.-C. Wu, M. Chen, C. Li, J. Zhang, and K. Mima, "Strong terahertz pulse generation by chirped laser pulses in tenuous gases," *Opt. Express* **16**(21), 16999-17006 (2008).
- [83] K. Y. Kim, J. H. Glowia, A. J. Taylor, and G. Rodriguez, "Terahertz emission from ultrafast ionizing air in symmetry-broken laser fields," *Opt. Express* **15**(8), 4577-4584 (2007).

References

- [84] J. Dai, J. Liu, and X. C. Zhang, "Terahertz Wave Air Photonics: Terahertz wave generation and detection with laser-induced gas plasma," *IEEE J. Sel. Topics Quantum Electron.* **17**(1), 183-190 (2011).
- [85] J. A. Miragliotta, B. Brawley, C. Sailor, J. B. Spicer, and J. W. M. Spicer, "Detection of microwave emission from solid targets ablated with an ultrashort pulsed laser," *Proc. of SPIE* **8037**, 80370N 1-8 (2011).
- [86] C. D'Amico, A. Houard, M. Franco, B. Prade, and A. Mysyrowicz, "Coherent and incoherent radial THz radiation emission from femtosecond filaments in air," *Opt. Express* **15**(23), 15274-15279 (2007).
- [87] O. G. Kosareva, V. P. Kandidov, A. Brodeur, C. Y. Chien, and S. L. Chin, "Conical emission from laser-plasma interactions in the filamentation of powerful ultrashort laser pulses in air," *Opt. Lett.* **22**(17) 1332-1334(1997).
- [88] I. Babushkin, W. Kuehn, C. Köhler, S. Skupin, L. Berge, K. Reimann, M. Woerner, J. Herrmann, and T. Elsaesser, "Ultrafast spatio-temporal dynamics of terahertz generation by ionizing two-color femtosecond pulses in gases," *Phys. Rev. Lett.* **105**, 053903 (2010).
- [89] P. Sprangle, J. R. Penano, B. Hafizi, and C. A. Kapetanakis, "Ultrashort laser pulses and electromagnetic pulse generation in air and on dielectric surfaces," *Phys. Rev. E* **69**, 066415 (2004).
- [90] J. Papeer, C. Mitchell, J. Penano, Y. Ehrlich, P. Sprangle and A. Zigler, "Microwave diagnostics of femtosecond laser-generated plasma filaments," *Appl. Phys. Lett.* **99**, 141503 1-3 (2011).
- [91] Y. Brelet, A. Houard, G. Point, B. Prade, L. Arantchouk, J. Carbonnel, Y. B. Andre, M. Pellet and A. Mysrowicz, "Radiofrequency plasma antenna generated by femtosecond laser filaments in air," *Appl. Phys. Lett.* **101**, 264106 1-3 (2012).
- [92] B. Forestier, A. Houard, M. Durand, Y.B. Andre, B. Prade, J. Y. Dauvignac, F. Perret, C. Pichot, M. Pellet and A. Mysyrowicz, "Radiofrequency conical emission from femtosecond filaments in air," *Appl. Phys. Lett.* **96**, 141111 1-3 (2010).
- [93] J. Philip, C. D'Amico, G. Che'riaux, A. Couairon, B. Prade, and A. Mysyrowicz, "Amplification of Femtosecond Laser Filaments in Ti:Sapphire," *Phys. Rev. Lett.* **95**, 163901 (2005).
- [94] Y. Liu, A. Houard, B. Prade, A. Mysyrowicz, and A. Diaw, "Amplification of transition-Cherenkov terahertz radiation of femtosecond filament in air," *Appl. Phys. Lett.* **93**, 051108 (2008).
- [95] A. Houard, C. D'Amico, M. Franco, B. Prade, A. Mysyrowicz, A. Couairon, and V. Tikhonchuk "Cerenkov THz Emission from Femtosecond Filamentation in Air," *Quantum Electronics and Laser Science Conference*, (2007).
- [96] E.T.J. Nibbering, P.F. Curley, G. Grillon, B.S. Prade, M.A. Franco, F. Salin, and A. Mysyrowicz, "Conical emission from self-guided femtosecond pulses in air," *Opt. Express* **21**(1), 61-64 (1996).

References

- [97] A. Houard, Y. Liu, B. Prade, V. T. Tikhonchuk, and A. Mysyrowicz, "Strong Enhancement of Terahertz Radiation from Laser Filaments in Air by a Static Electric Field," *Phys. Rev. Lett.* **100**, 255006 (2008).
- [98] Y. Liu, A. Houard, B. Prade, S. Akturk, and A. Mysyrowicz, "Terahertz Radiation Source in Air Based on Bifilamentation of Femtosecond Laser Pulses," *Phys. Rev. Lett.* **99**, 135002 (2007).
- [99] H. Nakajima, Y. Shimada, T. Somekawa, M. Fujita and K. A. Tanaka, "Nondestructive sensor using microwaves from laser plasma by subnanosecond laser pulses," *IEEE Geosci. Remote Sens. Lett.* **6**, 718-722 (2009).
- [100] H. Nakajima, M. Yamaura, Y. Shimada, M. Fujita and K. A. Tanaka, "Ground penetrating radar using a microwave radiated from laser-induced plasma," *J. Phys. Conf. Ser.* **112**, 042086 1-4 (2008).
- [101] Service and installation manual, "Spitlight 1200 Nd:YAG laser system," (2006).
- [102] Service and installation manual, "EKSPLA PL2250 series lasers," (2012).
- [103] T. G. Thomas and S. Chandra Sekhar, "Communication theory," *Tata McGraw - Hill* (2002).
- [104] Basic mode guide, "Agilent Technologies PSA Series," (2008).
- [105] Antenna mount guide, "ETS-Lindgren antennas," (2012).
- [106] <http://www.indiatelecomonline.com/telecom-spectrum-allocation-in-india/>
- [107] K. K. Sharma, "Optics: Principles and Applications" *Acad. press* (2006).
- [108] S. H. Voldman, "ESD: RF Technology and Circuits," *Wiley* (2006).
- [109] S. G. Rabinovich "Measurement Errors and Uncertainties: Theory and Practice," *Springer* (2005).
- [110] K. B. Klaassen, "Electronic Measurement and Instrumentation," *Cambridge University press* (2002).
- [111] D. Leenaerts, J. van der Tang and C. S. Vaucher, "Circuit Design for RF Transceivers," *Kluwer-academic* (2001).
- [112] L. Vinoth Kumar, Ch. Leela, E. Manikanta, Surya P. Tewari and P. Prem Kiran, "Detection and analysis of low-frequency electromagnetic emissions from ns laser induced breakdown of air," *Proc. of SPIE* **8434**, 84340V 1-6 (2012).
- [113] J. Mauricio Paulin Fuentes, C. Sánchez-Aké, F. O. Bredice, and M. Villagrán-Muniz, "Dipolar distribution generated by laser-induced plasma (LIP) in air in earliest instants," *J. Phys. D. Appl. Phys.* **46**(49), 495202 (2013).
- [114] E. Hecht and A. R. Ganesan, "Optics," *Pearson* (2002).
- [115] A. V. Kabashin. and P. I. Nikitin, "Electric fields of a laser spark produced by radiation with various parameters," *Quantum Electron.* **27**(6), 536-541 (1997).

References

- [116] F. F. Chen, "Introduction to plasma physics and controlled fusion vol 1: plasma physics" *Plenum press* (1984).
- [117] L. Vinoth Kumar, E. Manikanta, C. Leela, and P. Prem Kiran, "Effect of laser intensity on radio frequency emissions from laser induced breakdown of atmospheric air", *J. Appl. Phys.* **119**, 214904 (2016).
- [118] G. P. Konnen, "Polarized Light in Nature" *Cambridge University press* (2012).
- [119] P. Brimbicombe, "Air Composition and Chemistry," *Cambridge University press* (1986).
- [120] P. Prem Kiran, Ch. Leela, Suman Bagchi, and S. P. Tewari, "Direction dependent asymmetric expansion of laser induced shockwaves in air", *Proc.SPIE 7721 772124-1 – 772124-7* (2010).
- [121] A. Z. Akcasu and L. H. Wald, "Bremsstrahlung of slow electrons in neutral gases," *Phys. fluids* **10**(6), 1327–1335 (1967).
- [122] S Soubacq, P Pignolet, E Schall and J Batina, "Investigation of a gas breakdown process in a laser-plasma experiment." *J. Phys. D: Appl. Phys.* **37**, 2686–2702 (2004).
- [123] L. Vinoth Kumar, E. Manikanta, C. Leela, and P. Prem Kiran, "Spectral selective radio frequency emissions from laser induced breakdown of target materials," *Appl. Phys. Lett.* **105**(6), 064102 (2014).
- [124] M. Muller, F. Kühn, P. Grobmann, P. Vrba, and K. Mann, "Emission properties of ns and ps laser-induced soft x-ray sources using pulsed gas jets," *Opt. Express* **21**(10), 223–230 (2013).
- [125] D. M. Goebel and I. Katz, "Fundamentals of Electric Propulsion: Ion and Hall Thrusters," *John Wiley and Sons* (2008).
- [126] T. X. Phuoc, "Laser spark ignition : experimental determination of laser-induced breakdown thresholds of combustion gases," *Opt. Commun.* **175**, 419–423 (2000).
- [127] J. A. Bittencourt "Fundamentals of Plasma Physics," *Springer* (2004).
- [128] G. Bekefi "Radiation processes in plasmas," *Wiley* (1966).
- [129] P. F. Browne, "Mechanism of gas breakdown by laser," *Proc. Phys. Soc.* **86**, 1323 (1965).
- [130] R. G. Pinnick, P. Chylek, M. Jarzembski, E. Creegan, V. Srivastava, G. Fernandez, J. D. Pendleton, and A. Biswas, "Aerosol-induced laser breakdown thresholds: wavelength dependence.," *Appl. Opt.* **27**(5), 987–996 (1988).
- [131] D. W. Forslund, J. M. Kindel and K. Lee, "Theory of Hot-Electron Spectra at High Laser Intensity," *Phys. Rev. Lett.* **39**, 284 (1977).
- [132] D. Batani, H. Stabile, A. Ravasio, G. Lucchini, F. Strati, T. Desai, J. Ullschmied, E. Krousky, J. Skala, L. Juha, B. Kralikova, M. Pfeifer, Ch. Kadlec, T. Mocek, A. Prag, H. Nishimura and Y. Ochi, "Ablation pressure scaling at short laser wavelength," *Phys. Rev. E* **68**, 067403 (2003).

References

- [133] J. D. Jackson, "Classical Electrodynamics" Wiley (1998).
- [134] C. Kittel, "Introduction to Solid State Physics," Wiley (2007).
- [135] N. B. Delone, "Basics of Interaction of Laser Radiation with Matter" *Frontiers* (1993).
- [136] P. D. Gupta, P. A. Naik and H. C. Pant, "Dependence of x-ray intensity scaling on target atomic number in laser produced plasmas," *J. Appl. Phys.* **56**, 1371 (1984).
- [137] P. Mulser and D. Bauer, "High power laser-matter interaction," Springer (2010).
- [138] D. Giulietti and L. A. Gizzi, "X-Ray Emission from Laser Produced Plasmas" *LaRivista del Nuovo Cimento* **21**, 1 (1998).
- [139] S. S. Mao, X. Mao, R. Greif, and R. E. Russo, "Observations of plasma formation during picosecond laser ablation of metals," *SPIE* **3935**, pp. 113–119 (2000).
- [140] Daniel Sola and Jose I. Pena, "Study of the Wavelength Dependence in Laser Ablation of Advanced Ceramics and Glass-Ceramic Materials in the Nanosecond Range," *Materials* **6**, 5302-5313 (2013).
- [141] E. Fogarassy, D. Geohagan and M. Stuke, "Laser ablation," Proceeding of the symposium F: Third International conference on laser ablation (COLA'95), *Appl. Surf. Science* **96-98**, 1-924 (1996).
- [142] J. Gonzalo, C. N. Afonso, and I. Madariaga, "Expansion dynamics of the plasma produced by laser ablation of BaTiO₃ in a gas environment," *J. Appl. Phys.* **81** (2), (1997).
- [143] N. S. Allen, "Photochemistry and photophysics of polymer materials" John Wiley (2010).
- [144] I. Radivojevic, "Spectrochemical Analysis of Solid Samples by Laser-induced Plasma Spectroscopy," Ph.D. thesis, Technischen Universitat, Munchen, 2004.
- [145] D. A. Ucko, "Basics for chemistry," Academic press (1982).
- [146] J. C. Miller and R. F. Haglund, "Laser ablation and desorption" Academic press (1998).
- [147] U. Mizutani, "Basics of Interaction of Laser Radiation with Matter," Cambridge University press (2001).
- [148] A. Thos, "X-Ray Emission and Particle Acceleration from a Liquid Jet Target Using a 1-kHz Ultrafast Laser System," Ph.D. thesis, Freien Universitat, Berlin, 2003.
- [149] A. Bogaerts and Z. Chen, "Effect of laser parameters on laser ablation and laser-induced plasma formation: A numerical modeling investigation," *Spectrochim. Acta Part B At. Spectrosc.* **60**(9-10), 1280–1307 (2005).
- [150] A. J. Effenberger, J. R. Scott, and I. Falls, "Effect of Atmospheric Conditions on LIBS Spectra," *Sensors*. **10**, 4907–4925 (2010).

References

- [151] A. De Giacomo, M. Dell’Aglia, R. Gaudio, S. Amoroso, and O. De Pascale, “Effects of the background environment on formation, evolution and emission spectra of laser-induced plasmas,” *Spectrochim. Acta Part B At. Spectrosc.* **78**, 1–19, Elsevier B.V. (2012).
- [152] C. Tse, M. J. Zohdy, J. Y. Ye, M. O’Donnell, W. Lesniak, and L. Balogh, “Enhanced optical breakdown in KB cells labeled with folate-targeted silver-dendrimer composite nanodevices,” *Nanomedicine* **7**(1), 97–106, Elsevier Inc. (2011).
- [153] J. Y. Ye, L. Balogh, and T. B. Norris, “Enhancement of laser-induced optical breakdown using metal/dendrimer nanocomposites,” *Appl. Phys. Lett.* **80**(10), 1713 (2002).
- [154] H. W. Jang, T. Sands, and J.-L. Lee, “Effects of KrF excimer laser irradiation on metal contacts to n-type and p-type GaN,” *J. Appl. Phys.* **94**(5), 3529 (2003).
- [155] A. M. El Sherbini, A. M. Aboufotouh, F. F. Rashid, S. H. Allam, A. El Dakrouri, and T. M. El Sherbini, “Observed Enhancement in LIBS Signals from Nano vs . Bulk ZnO Targets: Comparative Study of Plasma Parameters,” *World J. nano Sci. Eng.* **2**, 181–188 (2012).
- [156] A. De Giacomo, R. Gaudio, C. Koral, and O. De Pascale, “Nanoparticle-Enhanced Laser-Induced Breakdown Spectroscopy of Metallic Samples” *Anal. Chem.* **85**, 10180–10187 (2013).
- [157] S. Bagchi, P. Prem Kiran, K. Yang, A. M. Rao, M . K. Bhuyan, M. Krishnamurthy and G. Ravindra Kumar, “Bright, low debris, ultrashort hard x-ray table top source using carbon nanotubes,” *Phys. Plasmas* **18**, 014502 (2011).
- [158] S. Bagchi, P. Prem Kiran, M. K. Bhuyan, S. Bose, P. Ayyub, M. Krishnamurthy and G. Ravindra Kumar, “Hot ion generation from nanostructured surfaces under intense femtosecond laser irradiation,” *Appl. Phys. Lett.* **90** 141502 1-3 (2007).
- [159] S. Bagchi, P. Prem Kiran, M. K. Bhuyan, S. Bose, P. Ayyub, M. Krishnamurthy and G. Ravindra Kumar, “Fast ion beams from intense, femtosecond laser irradiated nanostructured surfaces,” *Appl.Phys.B* **88** 167-173 (2007).
- [160] S. Bagchi, P. Prem Kiran, M. K. Bhuyan, S. Bose, P. Ayyub, M. Krishnamurthy and G. Ravindra Kumar, “Hotter electrons and ions from nano-structured surfaces,” *Laser Part. beams* **26**, 259–264 (2008).
- [161] D. A. Cremers and L. J. Radziemski, “Handbook of Laser-Induced Breakdown Spectroscopy,” second edition, *Wiley* (2013).
- [162] Ch. Leela, V. R. Kumar, S. P. Tewari and P. Prem Kiran, “Laser-induced shock waves from structured surfaces,” *Proc SPIE.* **8433**, 57 (2012).
- [163] S. Bagchi, P. Prem Kiran, W. M. Yang, Z. M. Sheng, M. K. Bhuyan, M. Krishnamurthy and G. Ravindra Kumar, “Surface-plasmon-enhanced MeV ions from femtosecond laser irradiated, periodically modulated surfaces,” *Phys. Plasmas* **19**, 030703 (2012).

References

- [164] A. Eksi and M. K. Kulekci, "Hardness and densification behaviour of copper and bronze powders," *METALURGIJA* **43**(1), 129–134 (2004).
- [165] E. Klar "American society of metals handbook : Powder metal technologies and applications" Volume **7**," *ASM International* (1984).
- [166] Z. Zhang, F. Wang, L. Wang, and S. Li, "Ultrafine-grained copper prepared by spark plasma sintering process," *Mater. Sci. Eng. A* **476**, 201–205 (2008).
- [167] S. Chaurasia, D. S. Munda, P. Ayyub, N. Kulkarni, N. K. Gupta, and L. J. Dhareshwar, "Laser plasma interaction in copper nano-particle targets," *Laser Part. beams* **26**, 473–478 (2008).
- [168] W. Hergert, "The Mie Theory; basics and applications," *Springer* (2012).
- [169] H. C. Van de Hulst, "Light Scattering by Small Particles," *Dover* (1981).
- [170] A. Serpenguzel, S. Arnold, G. Griffel and J. A. Lock, "Enhanced coupling to microsphere resonances with optical fibers," *J. Opt. Soc. Am. B*, **14** (1997).
- [171] A. Chen, Y. Jiang, T. Wang, J. Shao and M. Jin "Comparison of plasma temperature and electron density on nanosecond laser ablation of Cu and nano-Cu," *Phys. Plasmas* **22**(033301), 1–5 (2015).
- [172] K.-H. Leitz, B. Redlingshöfer, Y. Reg, A. Otto, and M. Schmidt, "Metal Ablation with Short and Ultrashort Laser Pulses," *Phys. Procedia* **12**, 230–238 (2011).
- [173] E. O. Olakanmi, R. F. Cochrane and K. W. Dalgarno, "A review on selective laser sintering/melting (SLS/SLM) of aluminium alloy powders: Processing, microstructure, and properties," *Prog. Mater Sci.* **74**, 401–477 (2015).
- [174] J. P. Agrawal, "High energy materials" *Wiley* (2010).
- [175] P. Ravi and S. P. Tewari, "Solvent Free Microwave Assisted Isomerization of N-Nitropyrazoles," *Propellants, Explosives, Pyrotechnics*. **38** (1), 147 (2013).
- [176] P. M. Pellegrino, E. L. Holthoff and M. E. Farrel "Laser-based optical detection of explosives" *CRC press* (2015).
- [177] A.K. Myakalwar, S. Sreedhar, I. Barman, N.C. Dingari, S.V. Rao, P.P. Kiran, S.P. Tewari, and G. M. Kumar, "Laser-induced breakdown spectroscopy-based investigation and classification of pharmaceutical tablets using multivariate chemometric analysis," *Talanta* **87**, 53-59 (2011).
- [178] A. Couairon, and A. Mysyrowicz, "Femtosecond filamentation in transparent media," *Phys.Reports* **441**, 47-189 (2007).

List of publications

List of publications relevant to thesis in refereed journals

- **L. Vinoth Kumar**, E. Manikanta, C. Leela, and P. Prem Kiran, “Effect of laser intensity on radio frequency emissions from laser induced breakdown of atmospheric air”, *J. Appl. Phys.* **119**, 214904 (2016).
- **L. Vinoth Kumar**, E. Manikanta, Ch. Leela, and P. Prem Kiran, “Spectral selective radio frequency emissions from laser induced breakdown of target materials”, *Appl. Phys. Lett.* **105**, 064102 (2014).
- **Kumar, L.V.**; Manikanta, E.; Leela, C.; Kiran, P.P., “RF emissions from laser breakdown of target materials”, IEEE proceedings on International conference of Microwave and Photonics (ICMAP), 1-4 (2013).
- **L. Vinoth Kumar**, Ch. Leela, E. Manikanta, Surya P. Tewari, P. Prem Kiran, “Detection and analysis of low frequency electromagnetic emissions from laser produced plasma, *Proc. SPIE* **8434**, Nonlinear Optics and Applications VI, 84340V 1-6 (2012).

Other publications

- E. Manikanta, **L. Vinoth Kumar**, Ch. Leela, and P. Prem Kiran, “Effect of pulse duration on the acoustic frequency emissions during laser induced breakdown of atmospheric air,” *Appl. Opt.* **55**(3), (2016).
- E. Manikanta, **L. Vinoth Kumar**, P. Venkateshwarlu, and P. Prem Kiran, “Acoustic shockwave emissions from ns and ps pulsed laser induced breakdown of air,” *Tech. Lett.* **10**, 16-19 (2014).
- B. P. Saha, **Vinoth Kumar**, S.V.Joshi, A. Balakrishnan, C. L. Martin, “Investigation of Compaction Behaviour of Alumina Nano Powder”, *Powder Technol*, **224**, 90-95 (2012).
- Alok Kumar Rai, K.N. Rao, **L. Vinoth Kumar** and K.D. Mandal, “Synthesis and Characterization of Ultra fine Barium Calcium Titanate, Barium Strontium Titanate and $Ba_{1-2x}Ca_xSr_xTiO_3$ ($x = 0.05, 0.1$),” *J.Alloys Compd.* **475**, 316-320 (2009).

Manuscripts under preparation

- **L. Vinoth Kumar**, E. Manikanta, and P. Prem Kiran, “Spectral selective radio frequency emissions from laser induced breakdown of conductors, insulators and dielectrics”.
- **L. Vinoth Kumar**, E. Manikanta and P. Prem Kiran, “Effect of target surface on the radio frequency emissions from the laser induced breakdown of copper micro compacts”.

- **L. Vinoth Kumar**, E. Manikanta, and P. Prem Kiran, “Investigation of radio frequency emissions from laser induced breakdown of High energy materials”.

Awards

- **Best paper** presented on “RF emissions from laser breakdown of target materials” in an IEEE sponsored International conference on Microwave and Photonics (ICMAP-2013).
- **Best poster** presented on “Low frequency radiation emissions from pulsed laser-matter interactions” in conference on Application of Lasers in Manufacturing 2015. (CALM-2015).